CODED APERTURE DESIGN IN COMPRESSIVE SPECTRAL IMAGING

by

Laura Galvis-Carreno

A dissertation submitted to the Faculty of the University of Delaware in partial fulfillment of the requirements for the degree of Doctor of Philosophy in Electrical and Computer Engineering

Spring 2018

CODED APERTURE DESIGN IN

COMPRESSIVE SPECTRAL IMAGING

by

Laura Galvis-Carreno

Approved: ______________________________

Kenneth E. Barner, Ph.D.
Chair of the Department of Electrical and Computer Engineering

Approved: ______________________________

Babatunde Ogunnaike, Ph.D.
Dean of the College of Engineering

Approved: ______________________________

Ann L. Ardis, Ph.D.
Senior Vice Provost for Graduate and Professional Education

I certify that I have read this dissertation and that in my opinion it meets the academic and professional standard required by the University as a dissertation for the degree of Doctor of Philosophy.

Signed: ____________________________________

Gonzalo R. Arce, Ph.D.
Professor in charge of dissertation

I certify that I have read this dissertation and that in my opinion it meets the academic and professional standard required by the University as a dissertation for the degree of Doctor of Philosophy.

Signed: ____________________________________

Kenneth E. Barner, Ph.D.
Member of dissertation committee

I certify that I have read this dissertation and that in my opinion it meets the academic and professional standard required by the University as a dissertation for the degree of Doctor of Philosophy.

Signed: ____________________________________

Javier Garcia-Frias, Ph.D.
Member of dissertation committee

I certify that I have read this dissertation and that in my opinion it meets the academic and professional standard required by the University as a dissertation for the degree of Doctor of Philosophy.

Signed: ____________________________________

Henry Arguello-Fuentes, Ph.D.
Member of dissertation committee

ACKNOWLEDGEMENTS

I would like to express my appreciation and sincere gratitude to my advisor, Professor Gonzalo R. Arce for his academic support and the opportunity of being part of his research group. I would like to thank my co-advisor Professor Henry Arguello for all his guidance and good advise, that will be always highly appreciated. I also want to thank Dr. Kenneth Barner and Dr. Javier Garcia-Frias, for accepting the invitation to be the members of my dissertation committee. I would like to thank Colciencias Colombia for the scholarship to pursue my Ph.D. at University of Delaware.

I also want to thank my fellow colleagues: Hoover Rueda, Claudia Correa, Angela Cuadros, Juan Becerra and Chen Fu. We were part of each others research paths and I will always remember those times together. Of course, to all my research group, the seminars, discussions, and lab time were valuable with their company.

I would specially thank my beloved husband, "Cari" for being part of my life, and for being my super-supportive partner in every possible way. Finally, I would like to give the greatest gratitude to my family. Their support has been unconditional all these years; they have cherished with me every great moment and supported me whenever I needed it. To my parents, all I am is because of them. To my sister, my best friend all my life, thanks for all her support and encouragement throughout this wonderful experience.

TABLE OF CONTENTS

LIST OF TABLES . . . . **viii**
LIST OF FIGURES . . . . **ix**
ABSTRACT . . . . **xvi**

Chapter

1 INTRODUCTION **1**

1.1 Motivation 3
1.2 Dissertation Organization 4
1.3 Research Contributions 5

2 CODED APERTURE DESIGN IN MISMATCHED COMPRESSIVE SPECTRAL IMAGING **7**

2.1 Introduction 8
2.2 CASSI Model With Pixels Grouping 10
2.3 CASSI with pixel mismatch 13

2.3.1 Mismatching by Super-resolution 14
2.3.2 Mismatching by Synthetic Coded Apertures 15
2.3.3 Reconstruction Algorithm 19

2.4 Experimental results 20

2.4.1 SR-CASSI Reconstructions 22
2.4.2 Synthetic-CASSI Reconstructions 23

2.5 Conclusions 25

3 CODED APERTURE DESIGN IN COMPRESSIVE SPECTRAL IMAGING BASED ON SIDE INFORMATION **29**

3.1 Introduction 29

3.2 CASSI model for spectral imaging 32
3.3 Spectral Imaging with Side Information 33

3.3.1 Coded aperture design based on side information 34

3.3.1.1 Edge estimation based on the RGB image 36
3.3.1.2 Coded aperture calculation 39

3.3.2 Reconstruction process 40

3.4 Simulations and Results 44

3.4.1 Simulations 44
3.4.2 Experimental Results 48
3.4.3 Reconstruction Enhancement 49

3.5 Conclusions 50

4 SHIFTING COLORED CODED APERTURE DESIGN FOR SPECTRAL IMAGING 53

4.1 Introduction 53
4.2 CASSI System for Spectral Imaging 56
4.3 Colored Coded Aperture Optimization 58

4.3.1 Variability constraint in Colored Coded Aperture Optimization 60
4.3.2 Uniformity constraint in Colored Coded Aperture Optimization 61

4.4 Gradient Descent Approach to find Optimized Colored Coded Aperture 66
4.5 Shifting Colored Coded Aperture 67

4.5.1 LH-Colored Coded Aperture Design 67
4.5.2 Shifting Color Coded Aperture Design 68

4.6 Simulations and Experimental Results 70

4.6.1 Simulations 70
4.6.2 Experimental Results 75

4.7 Conclusions 85

BIBLIOGRAPHY 86

Appendix

A COPYRIGHT NOTICE 93
B DISCLAIMER 94

LIST OF TABLES

2.1 Comparison of the traditional CASSI and CASSI with pixel mismatch specifications. The number of resolvable bands is determined by Δ_d. 22

LIST OF FIGURES

1.1 Coded aperture snapshot spectral imager (CASSI) architecture. The main components are the coded aperture, the dispersive element, and the detector. 2

2.1 The CASSI architecture is illustrated. The data cube is coded, spectrally dispersed and integrated on the FPA. 10

2.2 Spatio-spectral data flow in the CASSI architecture. The source is coded by the coded aperture and dispersed by a prism. A source voxel is zoomed to identify the regions R_0, R_1 and R_2. 13

2.3 Physical sensing phenomena in CASSI, L spectral bands of the data cube $\mathbf{F}$ are coded spatially by a coded aperture $\mathbf{T}$ and dispersed by the prism. The detector captures the intensity g by integrating the coded light. The pixel pitch mismatch is depicted and zoomed, the FPA detector receives the coded and dispersed light but it is missing a pixel-to-pixel correspondence. The high resolution of the detector is therefore sub-utilized. 14

2.4 (Left) Grouping of pixels at the coded aperture in traditional-CASSI. (Right) Matching of the coded aperture and detector resolutions - SR-CASSI. 16

2.5 (Left) Translation from a coded aperture into its synthetic version. (Right) Matching of the coded aperture and detector resolutions through the use of a synthetic coded aperture. 18

2.6 Coded apertures and measurements for (Left) Traditional CASSI and (Right) CASSI with pixel mismatch. The projections attained with the CASSI with pixel mismatch model have a high resolution compared with those obtained with the traditional CASSI. 21

2.7 Experimental reconstructions of five spectral bands. (Top) Traditional CASSI, (Bottom) SR-CASSI. The improvement in the spatial quality achieved with the SR-CASSI can be easily noticed. . 23

2.8 RGB profile of the (Left) traditional and (Right) SR-CASSI reconstructions. The SR-CASSI achieves a smoothed reconstruction compared with the traditional result. 24

2.9 Spectral signatures of three different spatial points. Traditional CASSI and SR-CASSI signatures are compared with the original spectral responses. The spectral curves obtained with the SR-CASSI are closer to the originals. 24

2.10 A synthetic coded aperture with the resolution of the detector is created. This synthetic coded aperture is used in the reconstruction process. 25

2.11 RGB profile of the (Left) traditional and (Right) Synthetic-CASSI reconstructions. Synthetic-CASSI yields a smoothed image, retaining the details of the scene. 26

2.12 Experimental reconstructions of five spectral bands. (Up) Traditional CASSI, (Down) Synthetic-CASSI. It can be seen that Synthetic-CASSI results outperforms the results achieved by the traditional CASSI. 26

2.13 Spectral signatures of three different spatial points. Traditional CASSI and Synthetic-CASSI signatures are compared with the original spectral responses. The improved results can be noticed in the spectral signatures achieved by the Synthetic-CASSI. 27

2.14 Experimental reconstructions of five spectral bands. (Up) Traditional CASSI, (Down) Synthetic-CASSI. It can be seen that Synthetic-CASSI results outperforms the results achieved by the traditional CASSI. 28

3.1 **H** Transfer function sketch for a $4 \times 4 \times L$ data cube, and for 2 snapshots. 34

3.2 Schematic architecture of CASSI with RGB side information. A beam splitter is utilized to divide the incident light into two different directions. 35

3.3 (a) A spectral band is reconstructed through simulation of the CASSI system using a random coded aperture pattern. Zoomed sections of the original and reconstructed band are presented in green and red squares. (b) Edge estimation using the Canny method and correlation between the reconstruction error and the estimated edges for the spectral band reconstructed in (a). 37

3.4 Edge Calculation for the $\mathbf{F}_k$ spatio-spectral image for $k = 8$. The edge estimation $\mathbf{S}_C$ using the RGB image is compared with the real edges $\mathbf{S}_T$. Edges of each band are calculated and then summed for both the complete data cube and the RGB image. An error image is created to show that pixels in yellow (87%) are correctly estimated from the RGB image $\mathbf{F}_C$. 41

3.5 Fusion of the spatio-spectral image $\hat{\mathbf{f}}$ and RGB image $\mathbf{F}_C$ with the GFPCA framework. 43

3.6 (Left) Designed coded aperture with transmittance $T = 0.25$. (Right) Estimated edges overlapping the designed coded aperture to visualize edge component. 45

3.7 Reconstruction of four spectral bands using the CASSI with side information. Left column depicts the original bands, second column shows the reconstruction using a random coded aperture and the third column shows the reconstruction using the designed coded aperture in Fig. 3.6. 46

3.8 Mean spectral PSNR for the eight reconstructed bands and spectral signatures for two representative spatial points, indicated as P1 and P2. 47

3.9 (Top) Two real scenes used to show the performance of the approach. (Bottom) Designed coded apertures using the side information for the two targets. 49

3.10 Reconstruction of 3 bands for Target 1 (Top) Using random coded aperture. (Bottom) Using designed coded aperture. 50

3.11 Reconstruction of 3 bands for Target 2 (Top) Using random coded aperture. (Bottom) Using designed coded aperture. 51

3.12 Spectral reconstruction of a red (P1) and purple (P2) spatial points. The spectral profiles for CASSI with side information using random coded aperture and CASSI with side information using designed coded aperture are depicted to compare the spectral reconstruction. A zoomed version of the toy chest is shown to highlight the quality at the borders. 52

3.13 High resolution reconstruction of simulations scene and Target 2. The spatial resolution of the reconstructions is 256×256 and 512×512 respectively. The RGB image is fused with the low resolution reconstruction to increase the spatial resolution of the enhanced final version. An RGB profile is also shown for the two scenes. 52

4.1 Physical sensing phenomena in colored CASSI; L spectral bands of the data cube $\mathbf{F}$ are coded spatially and spectrally by a colored coded aperture, and dispersed by the prism. The detector captures the intensity $\mathbf{g}$ by integrating the coded and dispersed light. 58

4.2 Proposed $\mathbf{X}$ matrix arrangement of a colored coded aperture in binary representation with a dimension of $16 \times 16 \times 3$, and for 2 snapshots. A random pattern is used for the sketch. 59

4.3 Illustration of the uniformity constraint aimed to reduce the total number of times a voxel is sensed through the shots. Red and blue squares in figure show voxels sensed twice for the 2 shots. 62

4.4 Sketch of the spectral uniformity constraint. Red areas show pixels reaching the same spatial pixels in the detector.Yellow pixels represent detector pixels integrating information of all the bands. Blue pixels are under-utilized detector pixels. 63

4.5 Sketch of the spectral and shot uniformity constraint. Red and blue squares show pixels sensed through all the bands and through all the shots. 64

4.6 Column uniformity constraint illustration: $\mathbf{XW}$. Several clusters as the two presented in the figure within red squares should be avoided. 65

4.7 Row uniformity constraint illustration: $\mathbf{ZX}$. Clusters as the two presented in the figure within red areas should be avoided. 65

4.8 Set of filters for $L = 3$ spectral bands $\lambda_1, \lambda_2, \lambda_3$. In the left the set of filters is presented with its respective color pixel representation. In the right the spectral response of four of the six filters is shown. . . 69

4.9 Equivalent representation of a colored coded aperture and its binary arrangement matrix $\mathbf{X}$. The colored coded aperture dimensions are 4×4 spatial pixels, $L = 3$ spectral bands, and $K = 2$ shots. A high pass and a low pass filters representations are specified. 69

4.10 The colored coded aperture resulting from binary arrangement $\mathbf{X}$ in Fig. 4.9 is used to show the concatenation shifting strategy used to design the shifting color coded apertures. 71

4.11 Four of the eight original spectral bands of the data cube used in simulations. 71

4.12 Reconstruction of four spectral bands using the CASSI with color coded apertures and 2 measurements shots. For each spectral band, three reconstructions from measurements modulated by LH-colored coded apertures, with a random pattern (Random), an optimized coded aperture in literature, designed by a genetic algorithm (GA optimized), and the designed coded apertures (Designed) are shown. 72

4.13 Reconstruction of four spectral bands using the CASSI with color coded apertures and 4 measurements shots. For each spectral band, three reconstructions from measurements modulated by LH-colored coded apertures, with a random pattern (Random), an optimized coded aperture in literature, designed by a genetic algorithm (GA optimized), and the designed coded apertures (Designed) are shown. 74

4.14 Mean PSNR achieved with $K = 2$ measurements shots for different vertical shifting value S from 1 to 32 pixels. 74

4.15 Mean PSNR achieved with $K = 4$ measurements shots for different vertical shifting value S from 1 to 32 pixels. 75

4.16 Two real scenes used to show the performance of designed shifting color coded apertures. 76

4.17 Reconstruction of four bands for Target 1 using LH random, genetic algorithm optimized and designed shifting colored coded apertures, for 2 shots. 77

4.18 Reconstruction of four bands for Target 1 using LH random, genetic algorithm optimized and designed shifting colored coded apertures, for 4 shots. 78

4.19 Reconstruction of four bands for Target 2 using LH random, genetic algorithm optimized and designed shifting colored coded apertures, for 2 shots. 79

4.20 Reconstruction of four bands for Target 2 using LH random, genetic algorithm optimized and designed shifting colored coded apertures, for 4 shots. 80

4.21 RGB profiles of reconstructed target 1 using $K = 2$ measurements shots. (Left) Random. (Center) GA Optimized. (Right) Designed. . 81

4.22 RGB profiles of reconstructed target 1 using $K = 4$ measurements shots. (Left) Random. (Center) GA Optimized. (Right) Designed color coded apertures. 81

4.23 RGB profiles of reconstructed target 2 using $K = 2$ measurements shots. (Left) Random. (Center) GA Optimized. (Right) Designed color coded apertures. 82

4.24 RGB profiles of reconstructed target 2 using $K = 4$ measurements shots. (Left) Random. (Center) GA Optimized. (Right) Designed color coded apertures. 82

4.25 Spectral signatures for P1 (red) in target 1 when (Left) $K = 2$, and (Right) $K = 4$ shots are used. 82

4.26 Spectral signatures for P2 (yellow) in target 1 when (Left) $K = 2$, and (Right) $K = 4$ shots are used. 83

4.27 Spectral signatures for P3 (blue) in target 1 when (Left) $K = 2$, and (Right) $K = 4$ shots are used. 83

4.28 Spectral signatures for P1 (green) in target 2 when (Left) $K = 2$, and (Right) $K = 4$ shots are used. 84

4.29 Spectral signatures for P2 (red) in target 2 when (Left) $K = 2$, and (Right) $K = 4$ shots are used. 84

4.30 Spectral signatures for P3 (red-orange) in target 2 when (Left) $K = 2$, and (Right) $K = 4$ shots are used. 85

ABSTRACT

Compressive Spectral Imaging (CSI) systems sense 3D spatio-spectral data cubes through just few two dimensional (2D) projections by using a coded aperture, a dispersive element, and an FPA. The coded apertures in these systems, whose main function is the modulation of the data cube, are often implemented through photomasks attached to piezoelectric devices. The optimization of such coded aperture patterns is an actual area of research. Two remarkable improvements on this configuration have been recently proposed. First, the replacement of the photomask by digital micromirror devices (DMD) for block-unblock coding in order to facilitate the capture of multiple projections/snapshots or the capture of multiple shots at video rates without the displacement of the optical elements on the system. Secondly, the replacement of block-unblock coded apertures by patterned optical filter arrays, referred as colored coded apertures, which not only allow spatial modulation but spectral modulation as well. Despite the improvements, the design of the coded aperture patterns is still constrained by hardware considerations. This dissertation aims to overcome these hardware considerations by developing different coded aperture design strategies.

When using the DMD for coding the data cube, the DMD resolution and the possibility to use multiple shots have to be considered. Usually, the pitch size of the DMD mirrors is different than the pitch size of the pixels in the detector. The mismatch of the DMD mirrors and the detector pixels is such that pixel-to-pixel correspondence is not achieved. The first proposed strategy is a mismatching coded aperture design to exploit the maximum resolution of the coding element and the detector. Additionally, the capture of multiple snapshots could be highly exploited to extract prior-information of the scenes, here a second strategy is proposed, the use of side information in CSI

not only to improve the reconstructions but to design scenes-adaptive coded aperture patterns.

On the other hand, when using colored coded apertures, its real implementation in terms of cost and complexity, directly depends on the number of filters to be used as well as the number of shots. A shifting color coded aperture optimization featuring these observations is proposed as the third strategy with the aim to improve the quality reconstruction and to generate an achievable optical implementation.

The mathematical models of the different strategies of computational imaging to overcome the limitations of actual CSI systems will be presented along with testbed implementations. Simulations as well as experimental results will prove the accuracy and performance of the three proposed coding strategies.

Chapter 1

INTRODUCTION

Spectral images can be described as images with spatial information across a large number of wavelengths. Despite the many applications of spectral information such as quality control in food and industrial agriculture [1, 2], medical imaging [3, 4, 5, 6], remote sensing [7, 8, 9], art conservation [10, 11, 12, 13], gas identification [14, 15], security applications [14, 15], between others [16], the implementation of spectral sensing systems and the subsequent acquisition and processing of data pose significant challenges.

Spectral imagers measures the intensity of light at different wavelengths for each spatial location in a scene. The resulting three-dimensional (3D) dataset is known as spatio-spectral data cube. Different spectral imagers have been developed to capture one dimensional and two dimensional subsets of the data cube. To obtain the complete data cube, a scanning of the remaining dimensions is required. Push-broom spectral imaging sensors, for instance, measure the spectrum at each spatial point in the scene through a slit spectrometer. In these sensors, there is a spatial motion of the slit or the object in order to acquire the whole data cube [17]. A limitation of these sensing techniques is that the number of zones to scan grows linearly in proportion to the desired spatial and spectral resolution. These instruments are adequate to capture static scenes, but their use in capturing non-static scenes is challenging. Furthermore, the amount of data captured, stored, or transmitted is directly related to the amount of sensed data, thus leading to the manipulation of large datasets.

In contrast, compressive spectral imaging (CSI) senses 2D coded projections of the underlying scene such that the number of measurements is far less than that used in scanning-type instruments [18]. Coded aperture compressive spectral imagers

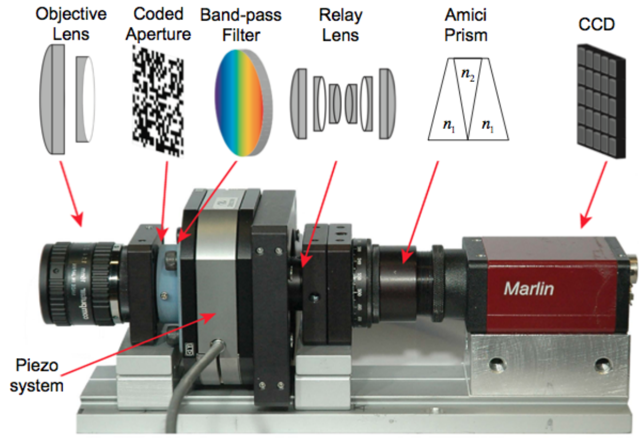

Figure 1.1: Coded aperture snapshot spectral imager (CASSI) architecture. The main components are the coded aperture, the dispersive element, and the detector.

capture two-dimensional projections by multiplexing the spatio-spectral information of a scene by means of a modulation and dispersion process. These imagers systems often rely on focal plane arrays (FPAs), spatial light modulators (SLMs), digital micromirror devices (DMDs), and dispersive elements. The coded aperture snapshot spectral imager (CASSI) is an example of a CSI architecture whose main components are a coded aperture, usually implemented by use of photomask, and a dispersive element such as a prism [19]. Figure 1.1 illustrates the CASSI architecture. It captures multiplexed (2D) projections of the spatio-spectral datacube using a snapshot. The data cube is denoted as $\mathbf{F}_{ijk}$ where i and j index the spatial coordinates, and k determines the k^{th} spectral plane. The multiplexed projections in CASSI are given by $\mathbf{g}_{mn} = \sum_{k=0}^{L-1} \mathbf{T}_{m(nk)} \mathbf{F}_{m(nk)k} + \omega_{mn}$, where $\mathbf{T}$ represents the coded aperture and ω the noise of the system [19].

The spectral signal $\mathbf{F} \in \mathbb{R}^{N \times N \times L}$, where $N \times N$ is its spatial resolution, and L is the number of resolvable bands, or its vector representation $\mathbf{f} \in \mathbb{R}^{N \cdot N \cdot L}$ is S-sparse on some basis $\mathbf{\Psi}$, such that $\mathbf{f} = \mathbf{\Psi}\boldsymbol{\theta}$ can be approximated by a linear combination of S vectors from $\mathbf{\Psi}$ with $S \ll (N \cdot N \cdot L)$. Alternatively, the CASSI projections can be expressed as $\mathbf{g} = \mathbf{H}\mathbf{\Psi}\boldsymbol{\theta} = \mathbf{A}\boldsymbol{\theta}$ where the $\mathbf{H}$ is a matrix whose structure is determined by the coded aperture entries and the dispersive element effect, and the matrix $\mathbf{A} = \mathbf{H}\boldsymbol{\Psi}$ is the sensing matrix. An estimation of the spatio-spectral data cube can be attained by solving the regularization problem

$$\tilde{\mathbf{f}} = \boldsymbol{\Psi}\{\text{argmin}_{\boldsymbol{\theta}}||\mathbf{g} - \mathbf{H}\boldsymbol{\Psi}\boldsymbol{\theta}||_2 + \tau||\boldsymbol{\theta}||_1\}, \tag{1.1}$$

where $\boldsymbol{\theta}$ is an S-sparse representation of $\mathbf{f}$, and τ is a regularization constant [20]. Different algorithms have been proposed to solve the optimization problem in Eq. 3.11, including the two-step iterative shrinkage/thresholding (TwIST) [21], the gradient projection for sparse reconstruction (GPSR) [22], Gaussian mixture models (GMM) [23], and the compressive imaging reconstruction algorithm based on the approximate message passing (AMP) framework [24].

1.1 Motivation

The increasing interest of compressive sensing theory in spectral imaging has generated the development of many compressive spectral imaging systems. These systems measure spatio-spectral information in such a way that the data cube is sensed (modulated and dispersed), and compressed at the same time. In fact, this data cube is acquired in the form of two-dimensional projections or measurements at the detector. Despite the differences in each implementation, these methods share the attempt to perform a direct 2D measurement, where each point from the scene is mapped to a single point in the optical sensor. The main components of these architectures are focal plane arrays, spatial light modulators, digital micromirror devices, and dispersive elements. The coded apertures, whose main function is the modulation of the data cube, are often implemented through photomasks attached to piezoelectric devices. The optimization of such coded aperture patterns is an actual area of research.

Two remarkable improvements in the coding devices for compressive spectral imaging have been recently proposed. The replacement of the photomask by digital micromirror devices, and the replacement of block-unblock coded apertures by patterned optical filter arrays or colored coded apertures, which allow the spatial and spectral modulation at the same time. This dissertation focuses in different strategies of coded aperture design in compressive spectral imaging, with the main purpose to overcome the forthcoming hardware constraints of the coding improvements, as well as to take advantage of the opportunities that they offer. The proposed coded aperture design strategies are developed and modeled, simulated, and experimentally implemented resulting in improved projections, and furthermore enhanced reconstructions of spectral images.

1.2 Dissertation Organization

The organization of this dissertation is as follows:

Chapter 2 covers a first hardware consideration usually faced by compressive spectral imagers, the pixel mismatch between coded aperture elements and detector pixels. A model for the CASSI with pixel mismatch is presented having as a motivation the full use of the coding and detector elements in the system. The model exploits the resolution of these devices and accounts two different cases of mismatching. First, a super-resolution model is presented to exploit the coded aperture resolution. This method, follows the same rationale than super-resolution approaches, where the idea is to translate high-resolution scenes into low-resolution detectors. Secondly, the creation of a synthetic coded aperture is proposed in order to reconstruct the spectral data cubes, at the detector resolution. Extensive simulations, as well as a testbed implementation illustrate the spatial and spectral improvement achieved with the proposed model in comparison with traditional approaches.

Chapter 3 presents a second hardware consideration in compressive spectral imaging, the fully DMD utilization. It is proposed a method to use side information from an RGB sensor to design the coded aperture patterns of a CSI. These adaptive coded apertures take advantage of the DMD capability to implement coded apertures with elaborately designed structure. The use of side information and specifically the estimation of the borders of the scene allows the coded aperture design, promoting a high quality reconstruction, specially of the high frequency components in the scene.

Moreover, the side information is also exploited for the reconstruction algorithm to improve the quality of the reconstructions, and even more, it is also used to achieve super-resolution by the use of a fusion algorithm taking advantage of the high resolution of the RGB image. Then, the side information is exploited twice, for both sensing and reconstruction processes. Simulations are used to illustrate the benefits of this approach. In addition, testbed reconstructions are also presented to verify the proposed coded aperture method based on the side information in a coded aperture compressive spectral imaging system.

In chapter 4, a color coded aperture optimization is presented. The optimization is constrained by a third hardware consideration, the achievable optical implementation in terms of costs and complexity. The optimization promotes the variability in the columns and rows of the coded aperture, the uniformity aimed at reducing the spatial, spectral and shot correlation of the samples in the acquisition process, and the filters limitation in terms of fabrication cost. A shifting color coded aperture, such that only one mask is required for several shots in a real implementation with a limited number of filters is proposed. The design can be implemented as a moving colored lithographic mask using a micro-piezo electric device, achieving a low space-time multishot compressive measurement acquisition. Several simulations and real reconstructions show the improvement achieved with the proposed optimization in comparison with random and optimized coded apertures from literature.

1.3 Research Contributions

The research work in this dissertation have been published in the following journals and conferences:

1. **L.V. Galvis**, E. Mojica, H. Arguello, and G.R. Arce. "Shifting colored coded aperture design for spectral Imaging", Journal in preparation to be submitted (2018).

2. **L.V. Galvis**, E. Mojica, H. Arguello, and G.R. Arce. "Colored coded aperture optimization: Experimental validation", Conference in preparation to be submitted (2018).

3. **L.V Galvis**, H. Arguello, D. Lau, and G. R. Arce. "Side information in coded aperture compressive spectral imaging", in Proc. SPIE 10117, Emerging Digital Micromirror Device Based Systems and Applications IX, 101170H, February 20, 2017.

4. **L.V Galvis**, D. Lau, X. Ma, H. Arguello, and G. R. Arce. "Coded aperture design in compressive spectral imaging based on side information", in Applied Optics, vol. 56, no. 22, pp. 6332-6340, 2017.

5. **L.V Galvis**, H .Arguello, and G. R. Arce. "Coded aperture design in mismatched compressive spectral imaging". Applied Optics, USA. Vol. 54, No. 33, pp. 9875-9882, 2015.

6. **L.V Galvis**, H. Arguello, and G. R. Arce. "Synthetic coded apertures in compressive spectral imaging: Experimental validation", in IEEE Global Conference on Signal and Information Processing (GlobalSIP), Orlando, FL, December 2015.

7. **L.V Galvis**, H. Arguello, and G. R. Arce. "Synthetic coded apertures in compressive spectral imaging", in IEEE ICASSP, Florence, Italy, May 2014.

Chapter 2

CODED APERTURE DESIGN IN MISMATCHED COMPRESSIVE SPECTRAL IMAGING

Compressive spectral imaging (CSI) senses a scene by using 2D coded projections such that the number of measurements is far less than that used in spectral scanning-type instruments. An architecture that efficiently implements CSI is the coded aperture snapshot spectral (CASSI) imager. A physical limitation of the CASSI is the system resolution, which is determined by the lower resolution element used in the the detector and the coded aperture. Although the final resolution of the system is usually given by the detector, in the CASSI for instance, the use of a low resolution coded aperture implemented using a digital micromirror device (DMD), which induces the grouping of pixels in super-pixels in the detector, is decisive to the final resolution. The mismatch occurs by the differences in the pitch size of the DMD mirrors and focal plane array (FPA) pixels. A traditional solution to this mismatch consists on grouping several pixels in square features which sub-utilizes the DMD and the detector resolution and, therefore reduces the spatial and spectral resolution of the reconstructed spectral images. This chapter presents a model for CASSI which admits the mismatch and permits to exploit the maximum resolution of the coding element and the FPA sensor. A super-resolution algorithm and a synthetic coded aperture are developed in order to solve the mismatch. The mathematical models are verified using a real implementation of CASSI. The results of the experiments show a significant gain in spatial and spectral imaging quality over the traditional grouping pixel technique.

2.1 Introduction

Spectral imaging systems acquire large amounts of data, by sequentially scanning either the spatial or spectral coordinates. The resulting signals are merged to construct a spectral data cube or three-dimensional (3D) data set, known as spatio-spectral data cube. Push-broom spectral imaging sensors, for instance, measure the spectrum at each spatial point in the scene through a slit spectrometer. In these sensors, there is a spatial motion of the slit or the object in order to acquire the whole data cube [25]. A limitation of these sensing techniques is that the number of zones to scan grows linearly in proportion to the desired spatial and spectral resolution. In contrast, compressive spectral imaging (CSI) systems sense the 3D data cube through just few two dimensional (2D) measurements of the coded and spectrally dispersed source field. These systems have gained popularity since they require fewer measurements than those attained with traditional hyperspectral imaging sensors [26, 19, 27].

A CSI architecture that efficiently attains coded measurements is the Coded Aperture Snapshot Spectral Imager (CASSI). It captures 2D coded aperture projections of the spatio-spectral data cube by using a coded aperture and a dispersive element. An inverse problem is solved to reconstruct the spectral images by using a linear program or a greedy pursuit in a basis where the under sampled signals admit sparse representations.

The coded apertures in CASSI are often implemented through photomasks attached to piezoelectric devices [28]. An improvement on this configuration has been proposed in order to facilitate the capture of multiple projections or snapshots, each admitting a different coded aperture pattern [29, 30, 28]. The replacement of the photomask by digital micromirror devices (DMD) allows the multicoding or the capture of multiple shots at video rates without the displacement of the optical elements on the system. Further, the DMD transmission efficiency is comparable to that offered by the photomask. Despite the selection of the coding element, the resolution has to be considered. Usually, the resolution or number of pixels of the DMD, is different than the exhibited by the detector. The mismatch of the DMD mirrors and the detector pixels is such that pixel-to-pixel correspondence is not achieved. This issue also occurs in detectors at γ- and x-ray wavelengths [31]. The traditional approach to match the resolution of the CASSI elements consists on grouping several pixels in square features. The maximum resolution of the system is then given by the element with lower resolution, sub-utilizing the resolution of the other element [32].

More formally, let $N_1 \times N_1$ be the resolution of the coded aperture and $N_2 \times N_2$ the resolution of the FPA. Two possible cases of mismatching can take place, which are analyzed by defining the relation between the resolutions of the detector and coded aperture as $N_1/p_1 = N_2/p_2$, where p_1 and p_2 are integers. The first case occurs when $P = \frac{p_1}{p_2} > 1$, which means that $N_1 > N_2$, and the second case occurs when $P' = \frac{p_2}{p_1} > 1$, meaning that $N_1 < N_2$. To alleviate this mismatch, several pixels can be grouped such that the resulting spatial resolution of the CASSI system is determined by $\min\{N_1, N_2\}$, which sub-utilizes the DMD or FPA resolutions. This work develops two methods to fully utilize the maximum resolution of the coded aperture and the detector. The first case $P > 1$, follows the same rationale than super-resolution approaches, where the idea is to translate high-resolution scenes into low-resolution detectors. A super-resolution technique is applied in this case to exploit the high resolution of the coded aperture in the CASSI system. In the second case $P' > 1$, the design of a synthetic coded aperture that allows to fully utilize the detector resolution is proposed.

The main contribution of this work is the development of a mathematical model for the CASSI with pixel pitch mismatch between the coded aperture and the detector. Two cases of mismatch are analyzed and modeled allowing the reconstruction of a high-resolution spatio-spectral data cube. The mathematical models developed are verified by using a real implementation of CASSI. Finally, the real reconstructions demonstrate the improvement obtained by using this approach instead of the traditional grouping of pixels.

2.2 CASSI Model With Pixels Grouping

The CASSI architecture is composed by a coded aperture, a dispersive element and a FPA as illustrated in Fig. 2.1. It captures multiplexed (2D) projections of a spatio-spectral data cube using a snapshot. The spatio-spectral power source density is defined as $f_0(x, y, \lambda)$, where (x, y) index the spatial dimensions and λ indexes the wavelength. The source is first coded by a coded aperture $T(x, y)$ where the black pixels block the impinging light and the white pixels permit light to pass through, resulting in the coded field $f_1(x, y, \lambda)$. The resulting coded field is then spectrally dispersed by a dispersive element. The impulse response of this component is $h(x' - S(\lambda) - x, y' - y)$, where $S(\lambda) = \alpha(\lambda)(\lambda - \lambda_c)$ accounts for the dispersion induced by the prism along the x-axis and λ_c is the central wavelength, which is not dispersed by the prism.

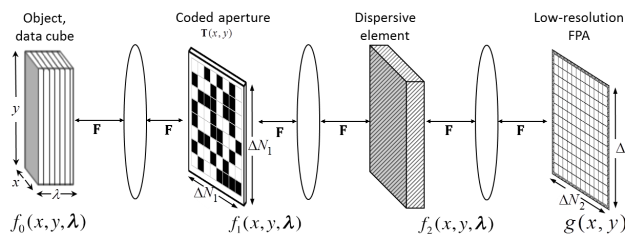

Figure 2.1: The CASSI architecture is illustrated. The data cube is coded, spectrally dispersed and integrated on the FPA.

Before the integration on the detector, the output can be expressed as

$$f_2(x, y, \lambda) = \iint T(x', y') f_0(x', y', \lambda) h(x' - S(\lambda) - x, y' - y) dx' dy'. \tag{2.1}$$

The compressive measurement at the focal plane array results from the integration of the coded and dispersed data field $f_2(x, y, \lambda)$ over the detector's spectral range sensitivity (Λ). The compressive measurement is represented as $g(x, y) = \int_\Lambda f_2(x, y, \lambda) d\lambda$.

When several FPA measurements are captured each one using a different coded aperture $T^\ell(x, y)$, the energy in front of the 2D FPA can be expressed as

$$g^\ell(x, y) = \int_\Lambda T^\ell(x - S(\lambda), y) f_0(x - S(\lambda), y, \lambda) d\lambda, \tag{2.2}$$

for $\ell = 0, 1, \ldots, K-1$ where K is the number of snapshots. The discretized compressive measurement at the respective pixel of the detector is given by

$$g_{mn}^{\ell} = \iint p(m, n; x, y) g^{\ell}(x, y) dx dy, \tag{2.3}$$

where $p(m, n; x, y) = \text{rect}\left(\frac{x}{\Delta_d} - m, \frac{y}{\Delta_d} - n\right)$ accounts for the detector pixelation in the detector, $\Delta_d = D_2/N_2$ is the pitch of the detector pixels and D_2 is the size of the detector. Replacing Eq. 2.2 in Eq. 2.3 leads to

$$g_{mn}^{\ell} = \iiint \text{rect}\left(\frac{x}{\Delta_d} - m, \frac{y}{\Delta_d} - n\right) T^{\ell}(x - S(\lambda), y) f_0(x - S(\lambda), y, \lambda) dx dy d\lambda. \tag{2.4}$$

The transmittance function of the coded aperture is given by

$$T^{\ell}(x, y) = \sum_{m', n'} t_{m'n'}^{\ell} \text{rect}\left(\frac{x}{\Delta_c} - m', \frac{y}{\Delta_c} - n'\right), \tag{2.5}$$

where $\Delta_c = D_1/N_1$ is the pitch of the coded aperture, D_1 is the size of the coded aperture, and $t_{m'n'}^{\ell}$ is the discretized version of the coded aperture $T^{\ell}(x, y)$.

Traditionally, the optical system can be designed such that $D_1 = D_2 = D$. This can be established through the prescription of the lens in the system to obtain an adequate magnification [19]. When $N_1 \neq N_2$, such that there is a pixel pitch mismatch $\Delta_c = D_1/N_1 \neq \Delta_d = D_2/N_2$, it is usual to artificially match the DMD and FPA resolutions. A common strategy consists on grouping several pixels in square features. This grouping reduces the resolution of the system which is given by $N = \min\{N_1, N_2\}$. This strategy implicates a significant reduction of the spatial and spectral resolution of the measurements and therefore of the reconstructions [33, 34].

When the pixels are grouped into square features such that $N = N_1/p_1 = N_2/p_2$, the integration of the continuous field $g(x, y)$ in a single $(m, n)^{th}$ detector pixel in Eq. 2.4 can be expressed as,

$$g_{mn}^{\ell} = \sum_{m',n'} t_{m'n'}^{\ell} \iiint \text{rect}\left(\frac{x - S(\lambda)}{\Delta} - m', \frac{y}{\Delta} - n'\right)$$
$$\text{rect}\left(\frac{x}{\Delta} - m, \frac{y}{\Delta} - n\right) f_0(x - S(\lambda), y, \lambda) dx dy d\lambda, \quad (2.6)$$

where $\Delta = D/N$. Eq. 2.6 is the forward model of CASSI, which has been recently extended to account for the non-linearity of the dispersive element [29]. In this new model, the energy from a single voxel is mapped onto three detector pixels, such that each source voxel can be split into three regions R_0, R_1 and R_2. Figure 2.2 illustrates a zoomed version of the regions of the source voxel affecting one pixel on the detector. The corresponding energy of each region that impinges in the $(m,n)^{th}$ detector pixel is represented by the weights w_{mnku}, where m, n index the spatial coordinates, k the spectral dimension and u accounts for the region R_0, R_1 and R_2 of the source voxel. More specifically, $w_{mnku} = (\iiint_{R_u} dx dy d\lambda)(\iiint_{R_1 \cup R_2 \cup R_3} dx dy d\lambda)^{-1}$. The following discrete notation is used to reformulate the FPA measurement. The source $f_0(x, y, \lambda)$ can be written as F_{mnk}, where m and n index the spatial coordinates and k determines the k^{th} spectral band. The discretized coded aperture is $t_{m'n'}^{\ell}$ as indicated in Eq. 2.5. Using this notation, the FPA measurement in Eq. 2.6 can be written as

$$g_{mn}^{\ell} = \sum_{k=0}^{L-1} \sum_{u=0}^{2} w_{mnku} t_{m(n-k-u)}^{\ell} F_{m(n-k-u)k}, \quad (2.7)$$

where $m, n = 0, 1, \ldots, N-1$, $k = 0, 1, \ldots, L-1$, $u = 0, 1, 2$ and $\ell = 0, 1, \ldots, K-1$. The number of resolvable bands L is determined by the detector resolution Δ. The spatial resolution N is determined for both, the FPA and coded aperture resolutions.

The analysis of the physical sensing phenomena in the CASSI system when $N_1 \neq N_2$ allows to develop different strategies to overcome the mismatch. Figure 2.3 illustrates an example of a mismatch, where more than one row of detector pixels receives the coded and dispersed light; in this particular case, it occurs given the high resolution of the detector.

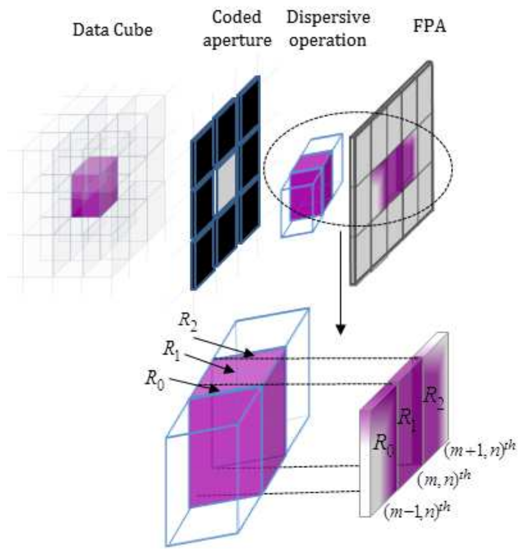

Figure 2.2: Spatio-spectral data flow in the CASSI architecture. The source is coded by the coded aperture and dispersed by a prism. A source voxel is zoomed to identify the regions R_0, R_1 and R_2.

2.3 CASSI with pixel mismatch

The CASSI with pixel mismatch is developed with the aim to solve the mismatching problem when $N_1 > N_2$ and $N_1 < N_2$. More formally, let $N_1 \times N_1$ be the resolution of the coded aperture and $N_2 \times N_2$ the resolution of the FPA. Two possible cases of mismatching can take place, which are analyzed by defining the relation between the resolutions of the detector and coded aperture as $N_1/p_1 = N_2/p_2$, where p_1 and p_2 are integers. The first case occurs when $P = \frac{p_1}{p_2} > 1$, which means that $N_1 > N_2$, and the second case occurs when $P' = \frac{p_2}{p_1} > 1$, meaning that $N_1 < N_2$. To alleviate this mismatch, several pixels can be grouped such that the resulting spatial resolution of the CASSI system is determined by $\min\{N_1, N_2\}$, which sub-utilizes the DMD or FPA resolutions. This work develops two methods to fully utilize the maximum resolution of the coded aperture and the detector. The first case $P > 1$, follows the same rationale than super-resolution approaches, where the idea is to translate high-resolution scenes into low-resolution detectors. A super-resolution technique is applied in this case to exploit the high resolution of the coded aperture in the CASSI system. In the second

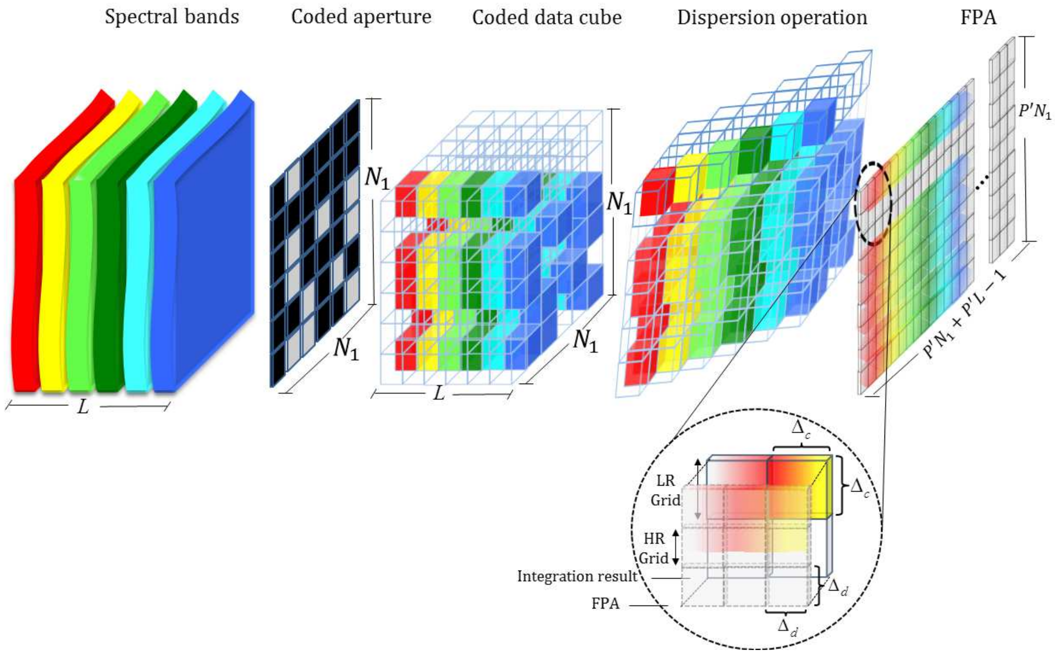

Figure 2.3: Physical sensing phenomena in CASSI, L spectral bands of the data cube $\mathbf{F}$ are coded spatially by a coded aperture $\mathbf{T}$ and dispersed by the prism. The detector captures the intensity g by integrating the coded light. The pixel pitch mismatch is depicted and zoomed, the FPA detector receives the coded and dispersed light but it is missing a pixel-to-pixel correspondence. The high resolution of the detector is therefore sub-utilized.

case $P' > 1$, the design of a synthetic coded aperture that allows to fully utilize the detector resolution is proposed.

2.3.1 Mismatching by Super-resolution

This case of mismatching occurs when the coded aperture resolution is higher than the FPA resolution. The approach to overcome this mismatching is to apply super-resolution to the model in Eq. 2.7. This is possible if the detector element pitch is greater than the Nyquist sample-limited resolution given by the wavelength of the light imaged [35, 36]. The energy impinging one detector pixel is divided in the number of coded aperture pixels that match that detector pixel. This sub-pixel division is included in the model in Eq. 2.7. The number of sub-pixels in a detector pixel P or the super-resolution factor respectively in the x and y dimensions depends on the number of coded aperture pixels matching one detector pixel following $N = N_1 = PN_2$. A decimation of the $(m,n)^{th}$ detector pixel is defined as,

$$g^{\ell}_{mn} = \sum_{q=0}^{P-1}\sum_{r=0}^{P-1} \hat{g}^{\ell}_{iP-q,jP-r}, \tag{2.8}$$

where $\hat{g}^{\ell}_{ij}$ is the measurement at the sub-pixel level and $i, j = 0, 1, \ldots, N_2(P-1)$. In addition, the dispersion effect must be modeled at the sub-pixel level in the horizontal dimension in both, the coded aperture and the source. Equation 2.7 is then rewritten including the sub-pixel decimation and the dispersion effect as,

$$\mathbf{G}^{\ell}_{mn} = \sum_{q=0}^{P-1}\sum_{r=0}^{P-1}\ \sum_{k=0}^{L-1}\sum_{u=0}^{2} \mathbf{w}_{(mP-q)(nP-r)ku}\mathbf{T}^{\ell}_{((mP-q-k)-k-u)(nP-r)}(F_k)_{((mP-q-k)-k-u)(nP-r)}, \tag{2.9}$$

where $\mathbf{F} \in \mathbb{R}^{N^2L}$, $\mathbf{T}^{\ell} \in \mathbb{R}^{N^2}$, and $\mathbf{G} \in \mathbb{R}^{N/P(N/P+L/P-1)}$. Notice the lower resolution of the detector compared with the coded aperture.

The forward model in Eq. 2.9 allows to use the full coded aperture resolution instead of the resolution exhibited by the detector, and as a result it is possible to obtain a high spatial resolution reconstruction. Figure 2.4 (Left) shows a traditional approach example, where 2×2 pixels are grouped at the coded aperture to match the resolutions. The SR-CASSI on Fig. 2.4 (Right) instead, take advantage of the full resolution of the coded aperture and proposes a solution with $P = 2$ to emulate a detector with the resolution of the coded aperture.

2.3.2 Mismatching by Synthetic Coded Apertures

The opposite case occurs when the FPA resolution is higher than that of the coded aperture. Since a pixel in the coded aperture is mapped into several pixels on the detector, the proportion of the coded aperture pixel as they are projected onto the

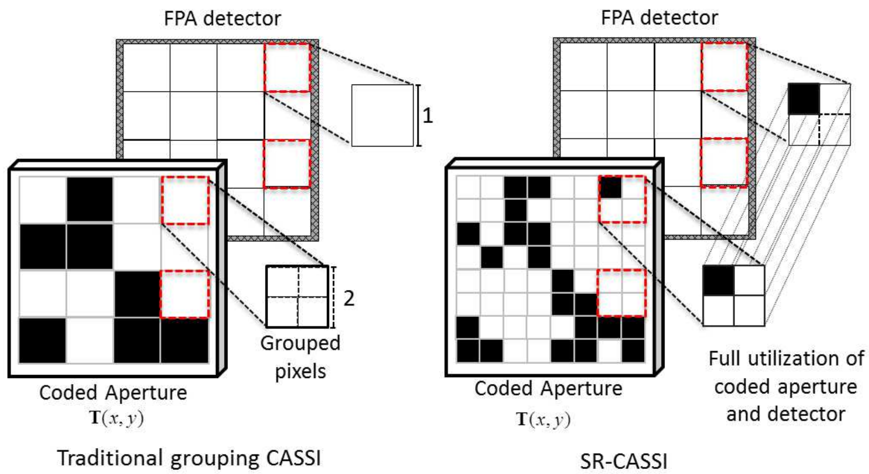

Figure 2.4: (Left) Grouping of pixels at the coded aperture in traditional-CASSI. (Right) Matching of the coded aperture and detector resolutions - SR-CASSI.

detector pixels, defines a synthetic gray-scale, higher resolution coded aperture. Thus, the projections attained by the system could be realized by a coded aperture matching the detector pixel size, with the exception that the coded aperture values needed to realize the projection are in this case, gray-scale, which model the proportion that is mapped from the coded aperture pixel into each of the detector pixels. It should be noted, that a higher resolution gray-scale coded is not used in the projection. It is only a model used to describe the physical phenomena of the pixel mismatch, and is then used into the reconstruction of the data cube. The FPA resolution replaces Δ in Eq. 2.6 using $N = P'N_1 = N_2$. The resulting g^{ℓ}_{mn} measurement includes the intensity of the corresponding P'^2 detector pixels. Traditionally, the measurement fails to exploit the sub-pixel information, the Synthetic-CASSI seeks to reach the level of resolution of the sub-pixels. More specifically, Eq. 2.6 should be reformulated as

$$g^{(1)\ell}_{mn} + g^{(2)\ell}_{mn} + \dots + g^{(P'^2)\ell}_{mn} = \sum_{m',n'} t^{\ell}_{m'n'} \iiint \operatorname{rect}\left(\frac{x - S(\lambda)}{P'\Delta_c} - m', \frac{y}{P'\Delta_c} - n'\right)$$
$$\operatorname{rect}\left(\frac{x}{P'\Delta_c} - m, \frac{y}{P'\Delta_c} - n\right) f_0(x - S(\lambda), y, \lambda) dx dy d\lambda. \quad (2.10)$$

A synthetic coded aperture with higher resolution is defined, in order to take into account the intensity on each $g_{mn}^{(th)\ell}$ of the left side on Eq. 2.10. Hence, the translation of the coded aperture $t_{m'n'}^{\ell}$ into one with higher resolution directly related with N_2 accounts for the mismatching effect produced by the resolution differences on the coded aperture and detector. This matching is done through the creation of a synthetic coded aperture. The synthetic coded aperture defined as $\hat{t}_{m'n'}$ is tuned in, and the FPA measurement at the N resolution is expressed as

$$g_{mn}^{(i)\ell}=\sum_{m'n'}\hat{t}_{m'n'}^{\ell}\iiint \mathrm{rect}\left(\frac{x-S(\lambda)}{\Delta}-m',\frac{y}{\Delta}-n'\right)\mathrm{rect}\left(\frac{x}{\Delta}-m,\frac{y}{\Delta}-n\right)f_0(x-S(\lambda),y,\lambda)dxdyd\lambda, \tag{2.11}$$

where $\Delta = D/N_2$ and i index each of the pixels at the detector. The synthetic coded aperture $\hat{t}_{m'n'}$ in Eq. 2.11 can be succinctly expressed as

$$\begin{aligned}\hat{t}_{m'n'} = \quad & \alpha\left(\beta\, t_{m',n'} + (1-\beta)\, t_{m',n'+1}\right) + \\ & (1-\alpha)\left(\beta\, t_{m'+1,n'} + (1-\beta)\, t_{m'+1,n'+1}\right).\end{aligned} \tag{2.12}$$

The synthetic coded aperture is defined in terms of α and β, accounting for the horizontal and vertical fraction of a pixel at the coded aperture that is reflected in the synthetic pixel of $\hat{t}_{m'n'}$, and the evaluation of the neighbours of the pixel (i,j) in the original discrete version of the coded aperture $t_{m'n'}$. These neighbours are denoted as $t_{m',n'}, t_{m',n'+1}, t_{m'+1,n'}, t_{m'+1,n'+1}$. The α and β fractions can be expressed as,

$$\alpha = \begin{cases} B, & B > 0 \\ 1, & B = 0 \end{cases}, \qquad \beta = \begin{cases} C, & C > 0 \\ 1, & C = 0 \end{cases}, \tag{2.13}$$

where B and C are defined in terms of the ratio between the coded aperture and the FPA pixel pitch $P' = \frac{p_2}{p_1}$ as

$$B = \left\lfloor \frac{(n+1)}{P'} \right\rfloor P' - n, \tag{2.14}$$

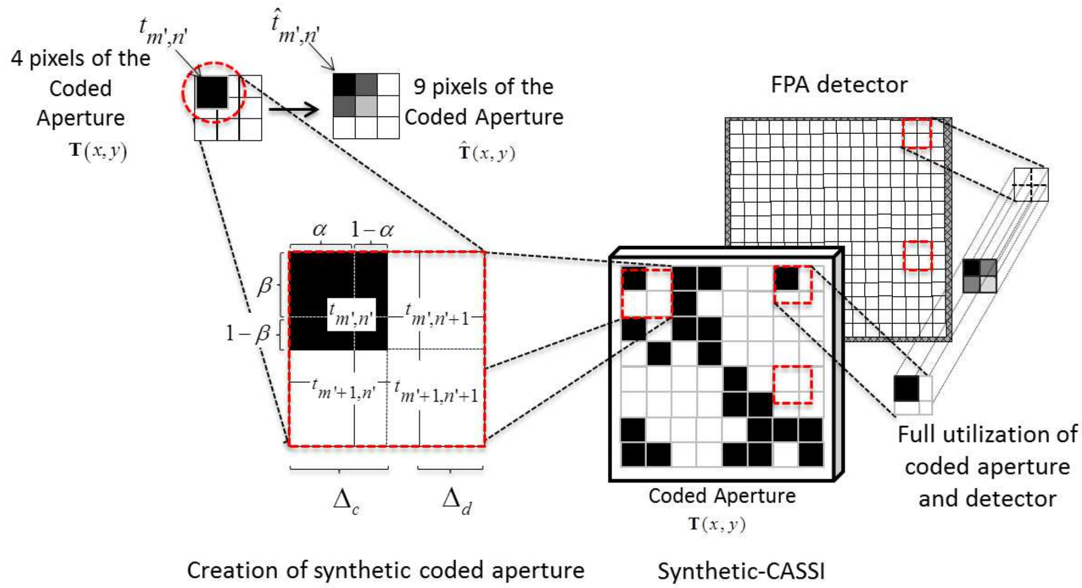

Figure 2.5: (Left) Translation from a coded aperture into its synthetic version. (Right) Matching of the coded aperture and detector resolutions through the use of a synthetic coded aperture.

$$C = \left\lfloor \frac{(m+1-k-u)}{P'} \right\rfloor P' - (m-k-u). \tag{2.15}$$

Figure 2.5 (Left) shows the translation from a small set of pixels of a coded aperture into its respective synthetic coded aperture. Figure 2.5 (Right) shows the matching of the resolutions through the creation of a synthetic coded aperture to fully utilize the detector resolution. It is noticeable the higher resolution of the synthetic coded aperture and detector in the Synthetic-CASSI.

The discretized Synthetic-CASSI model is then expressed as

$$\mathbf{G}^{\ell}_{mn} = \sum_{k=0}^{(L-1)P'} \sum_{u=0}^{2} w_{mnku} \hat{\mathbf{T}}^{\ell}_{m(n-k-u)} (\mathbf{F}_k)_{m(n-k-u)}, \tag{2.16}$$

where the spatial and spectral resolutions of this measurements are dictated by P' such that $m,n = 0,1,\ldots,(N-1)P'$ and $k = 0,1,\ldots,(L-1)P'$.

2.3.3 Reconstruction Algorithm

The hyperspectral signal $\mathbf{F} \in \mathbb{R}^{N \times N \times L}$, or its vector representation $\mathbf{f} \in \mathbb{R}^{N \cdot N \cdot L}$ is S-sparse on some basis $\boldsymbol{\Psi}$, such that $\mathbf{f} = \boldsymbol{\Psi\theta}$ can be approximated by a linear combination of S vectors from $\boldsymbol{\Psi}$ with $S \ll (N \cdot N \cdot L)$. Alternatively, the CASSI projections in Eq. 2.9 and Eq. 2.16 can be expressed as $\mathbf{g} = \mathbf{H}\boldsymbol{\Psi\theta} = \mathbf{A}\boldsymbol{\theta}$ where the $\mathbf{H}$ is a matrix whose structure is determined by the coded aperture entries and the dispersive element effect, and the matrix $\mathbf{A} = \mathbf{H}\boldsymbol{\Psi}$ is the sensing matrix. This algorithm solves the optimization problem

$$\tilde{\mathbf{f}} = \boldsymbol{\Psi}\{\text{argmin}_{\boldsymbol{\theta}}||\mathbf{g} - \mathbf{H}\boldsymbol{\Psi\theta}||_2 + \tau||\boldsymbol{\theta}||_1\}, \tag{2.17}$$

where $\boldsymbol{\theta}$ is an S-sparse representation of $\mathbf{f}$, and τ is a regularization constant [20]. The basis representation $\boldsymbol{\Psi}$ is set as the kronecker product of two basis $\boldsymbol{\Psi} = \boldsymbol{\Psi}_1 \bigotimes \boldsymbol{\Psi}_2$, where $\boldsymbol{\Psi}_1$ is a 2D-Wavelet Symmlet 8 basis and $\boldsymbol{\Psi}_2$ is the 1D-Discrete Cosine Transform.

The compressive sensing GPSR algorithm is used to obtain the reconstructions of the data cube [22]. The methods proposed, in essence, increase the resolution of the reconstructed data cubes, and consequently the inverse problem deals with large sets of pixels to be reconstructed. As such, the computational complexity of the reconstruction increases in proportion to the added spatial and spectral resolution. The computational complexity is determined by the particular reconstruction algorithm. In this case, the GPSR complexity is $\mathcal{O}(KN^4L)$ per iteration, where K is the number of snapshots, N^2 is the spatial resolution, and L is the number of spectral bands. Hence, the complexity in the two approaches described is determined also by the $P > 1$ and $P' > 1$ factors. The computational complexity is then $\mathcal{O}(KN^4P^4L)$ for the mismatching by super-resolution and $\mathcal{O}(KN^4P'^4L)$ in the case of the mismatching by synthetic coded apertures.

2.4 Experimental results

The CASSI system was experimentally realized to demonstrate the CASSI with pixel mismatch performance. The coded apertures were implemented in a Texas Instruments D1100 DMD (DLP), a custom double Amici prism (Shangai Optics) was used as a dispersive element and a FPA detector (Stingray F-033B) captured the measurements. The non-linear dispersion curve of the prism was determined experimentally by using a monochromator. The DMD used to implement the coded apertures has a resolution of 1024×768 and a mirror pitch size of $\Delta_c = 13.68\mu m$. The FPA detector used in this experimental setup has a resolution of 656×492 pixels and a pitch size of $\Delta_d = 9.9\mu m$.

Three set of compressive measurements were acquired by using the CASSI optical setup. The sets correspond to the traditional CASSI, the SR-CASSI and the Synthetic-CASSI measurements respectively. In the traditional CASSI, the pixels are grouped into square features to match the resolutions on the coded aperture and the detector using the relation $N = N_1/p_1 = N_2/p_2$, where $p_1 = 2$, $p_2 = 3$, $N_1 = 318$ and $N_2 = 477$. In this traditional case, the reconstructed images have a low spatial resolution of 159×159 pixels due to the grouping process. Also, this grouping approach limits the number of spectral bands to 8. For the three cases a sensing ratio of 50% was used and the GPSR algorithm was used to recover the spatio-spectral data cube [22]. Table 2.1 shows the specifications of the three set of measurements.

A visual comparison of the coded apertures and measurements is presented in Figure 2.6 top and Bottom respectively. 318×318 DMD mirrors were used to implement the coded apertures for the three sets. The traditional approach however, requires the grouping of pixels, which reduces the actual resolution of the coded aperture designed (Top-Left), compared with the high resolution of the coded apertures implemented in the CASSI with pixel mismatch (Top-Right). On the other hand, the traditional CASSI measurements in Fig. 2.6 (Bottom-Left) have low resolution; the measurements resolution for the first case of mismatching (SR-CASSI) is the same as in the traditional case, but the codification using a high-resolution coded aperture produces a more

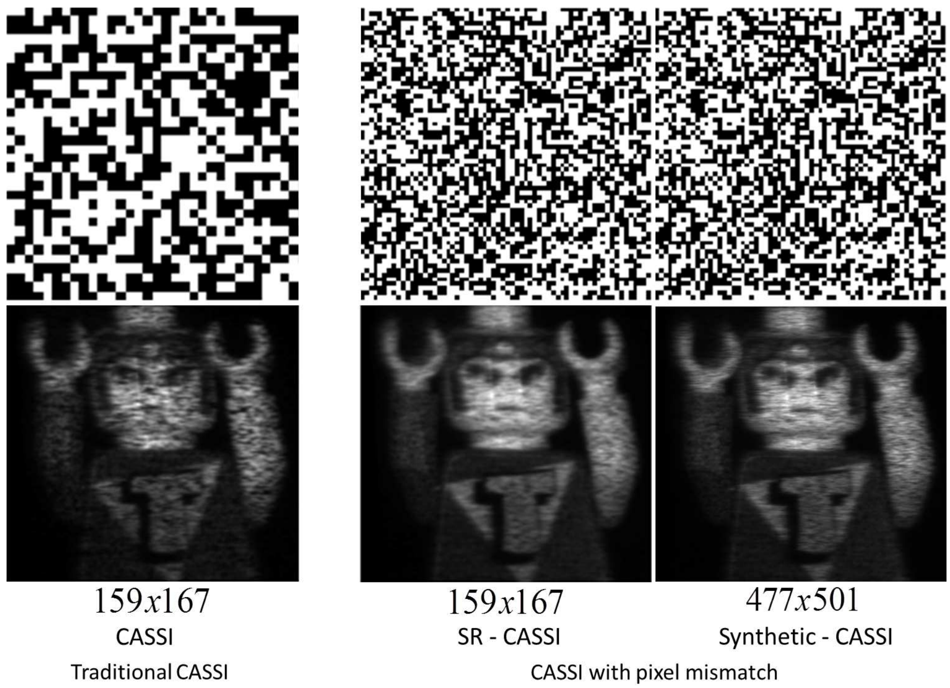

Figure 2.6: Coded apertures and measurements for (Left) Traditional CASSI and (Right) CASSI with pixel mismatch. The projections attained with the CASSI with pixel mismatch model have a high resolution compared with those obtained with the traditional CASSI.

Table 2.1: Comparison of the traditional CASSI and CASSI with pixel mismatch specifications. The number of resolvable bands is determined by Δ_d.

Cases (# of pixels)	Mirrors and pixels pitch sizes (μm)		Resolution (Pixels)		
	Δ_c	Δ_d	Coded Aperture	Spatial Recons.	Spectral Recons.
Traditional CASSI $159 = 318/2 = 477/3$	$\Delta_c = 27.36$*	$\Delta_d = 29.7$**	159×159	159×159	8
SR-CASSI $318 = 318 = (2)159$	$\Delta_c = 13.68$	$\Delta_d = 29.7$**	318×318	318×318	8
Synthetic-CASSI $477 = (3/2)318 = 477$	$\Delta_c = 13.68$	$\Delta_d = 9.9$	318×318	477×477	24

* 2×2 grouping of pixels.
** 3×3 grouping of pixels.

detailed 2D projection. The Synthetic-CASSI measurements have a high-resolution as well as a codification with a high-resolution coded aperture.

2.4.1 SR-CASSI Reconstructions

The measurements for the SR-CASSI were acquired implementing a coded aperture with a resolution $N_1 = 318$ pixels. To emulate a low-resolution detector, its pixels were grouped into 3×3 square features representing one low-detector pixel for a $N_2 = 159$ such that $P = 2$. After the application of the SR-CASSI model in Eq. 2.9 and applying the GPSR algorithm that solves the optimization problem in Eq. 2.17, the measurements and the reconstructions have the coded aperture resolution, this is 318×318 pixels. Therefore, the coded aperture resolution is fully utilized. In this case, the number of resolvable bands is 8.

The traditional CASSI reconstructions were interpolated to the resolution of the SR-CASSI approach $318 \times 318 \times 8$ to compare the results. Figure 2.7 illustrates five spectral bands for the traditional CASSI and the SR-CASSI respectively. It can be observed that the SR-CASSI results outperforms the results attained with the traditional approach.

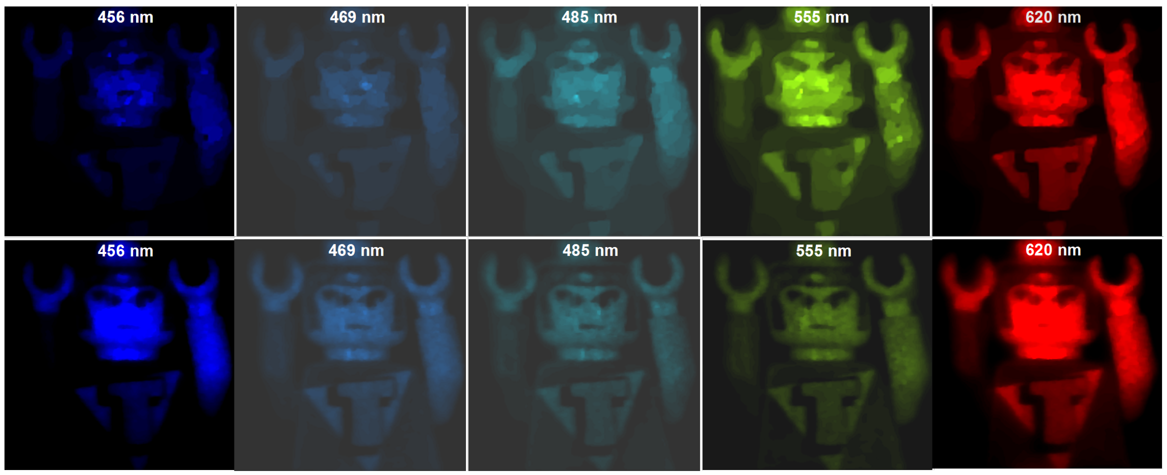

Figure 2.7: Experimental reconstructions of five spectral bands. (Top) Traditional CASSI, (Bottom) SR-CASSI. The improvement in the spatial quality achieved with the SR-CASSI can be easily noticed.

Figure 2.8 shows a RGB profile of the traditional and SR-CASSI. The details in the SR-CASSI reconstruction can be easily noticed. The spectral signatures for three points randomly chosen are shown in Fig. 2.9. The points are indicated in the original RGB image as P1, P2 and P3. The original signature, obtained using a commercially available spectrometer (Ocean Optics USB2000+) is compared with the traditional CASSI and the SR-CASSI signatures. The curves obtained by using the SR-CASSI are closer to the original.

2.4.2 Synthetic-CASSI Reconstructions

In the third set of measurements, the Synthetic-CASSI is tested using a resolution $N_1 = 318$ pixels to implement the coded aperture and as a result, the FPA measurement has a resolution $N_2 = 477$ pixels such that $P' = 3/2$. Applying the Synthetic-CASSI model in Eq. 2.16, a synthetic coded aperture with the same used resolution of the detector is created to reconstruct the spatio-spectral data cube. Fig 2.10 shows a coded aperture and its equivalent synthetic coded aperture such as the used to reconstruct the data-cube. Then, the final spatial resolution of the reconstructed images is 477×477 pixels. As a result, the detector resolution is fully utilized. In this

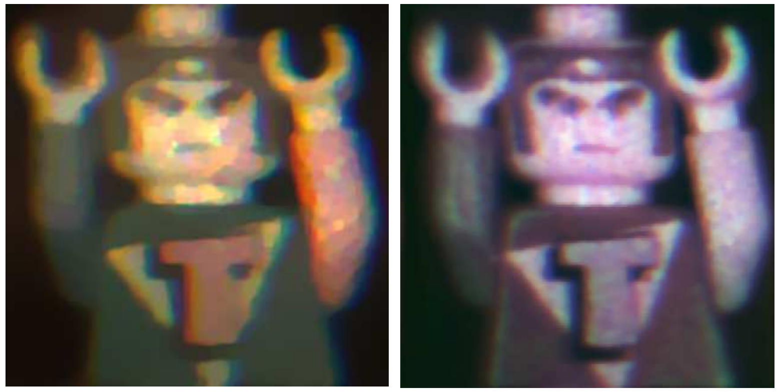

Figure 2.8: RGB profile of the (Left) traditional and (Right) SR-CASSI reconstructions. The SR-CASSI achieves a smoothed reconstruction compared with the traditional result.

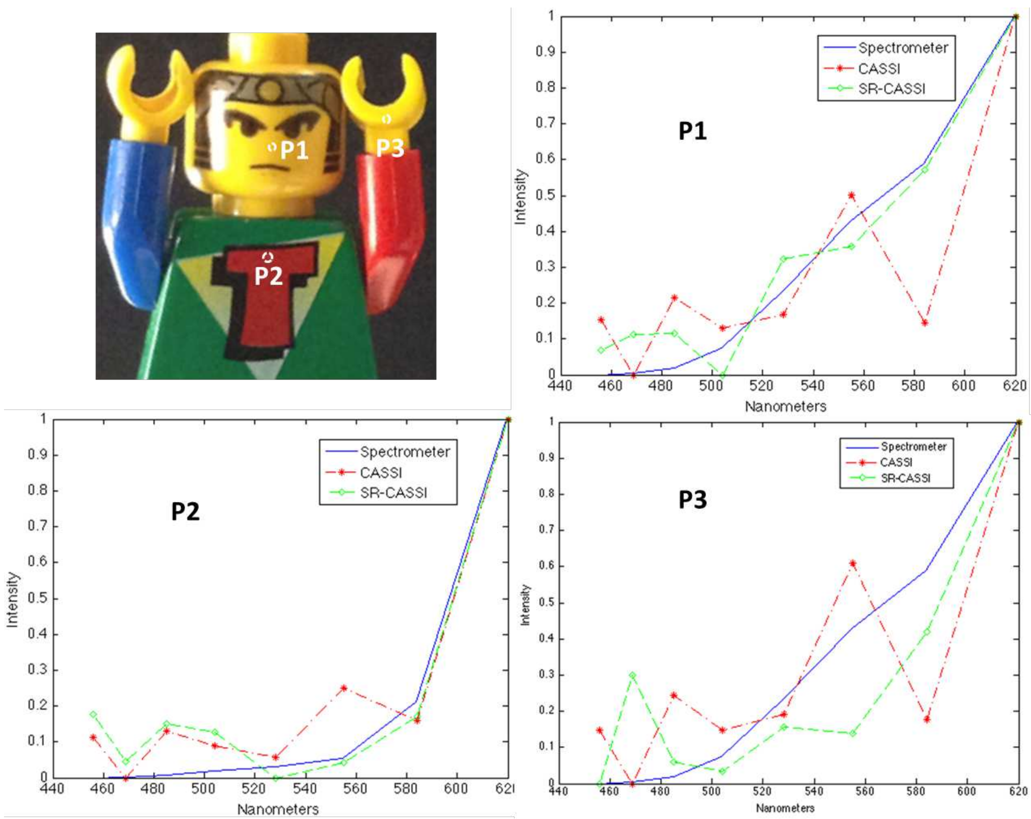

Figure 2.9: Spectral signatures of three different spatial points. Traditional CASSI and SR-CASSI signatures are compared with the original spectral responses. The spectral curves obtained with the SR-CASSI are closer to the originals.

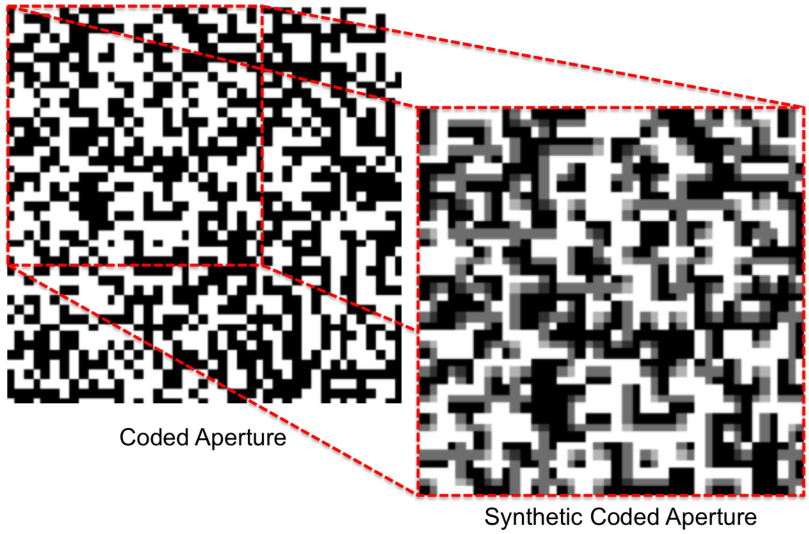

Figure 2.10: A synthetic coded aperture with the resolution of the detector is created. This synthetic coded aperture is used in the reconstruction process.

case, the high-resolution of the FPA permits to achieve 24 spectral bands.

In order to compare the results, the traditional CASSI reconstructions were interpolated to the resolution of the Synthetic-CASSI approach $477 \times 477 \times 24$. The RGB profiles of the traditional and Synthetic-CASSI are depicted in Fig. 2.11. The improvement in the spatial quality can be easily noticed. Figure 2.14 shows five spectral bands for the traditional CASSI, and the Synthetic-CASSI respectively. The improvement in the spatial quality can be observed.

The spectral signatures of three randomly selected points are compared with the signatures obtained using a spectrometer in Fig. 2.13. The points are indicated as P1, P2 and P3. Again, it can be seen how the curves using the Synthetic-CASSI are closer to the originals, which demonstrate the improvement of the model.

2.5 Conclusions

A mathematical model for the CASSI with pixel mismatch has been developed. The model exploits the resolution of the DMD and FPA which therefore determines

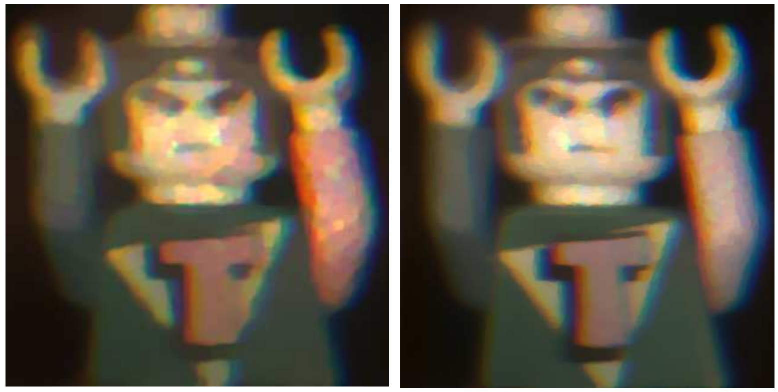

Figure 2.11: RGB profile of the (Left) traditional and (Right) Synthetic-CASSI reconstructions. Synthetic-CASSI yields a smoothed image, retaining the details of the scene.

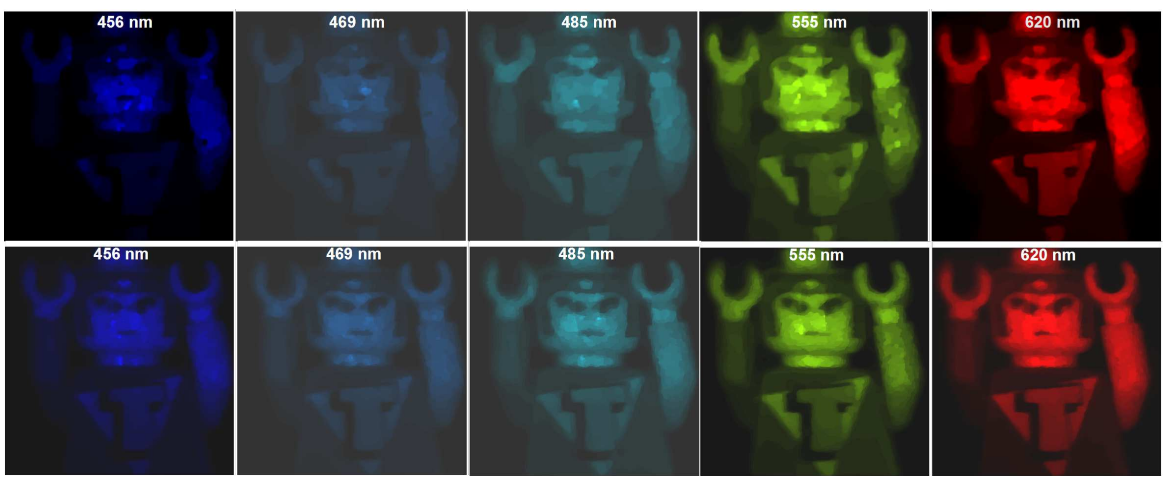

Figure 2.12: Experimental reconstructions of five spectral bands. (Up) Traditional CASSI, (Down) Synthetic-CASSI. It can be seen that Synthetic-CASSI results outperforms the results achieved by the traditional CASSI.

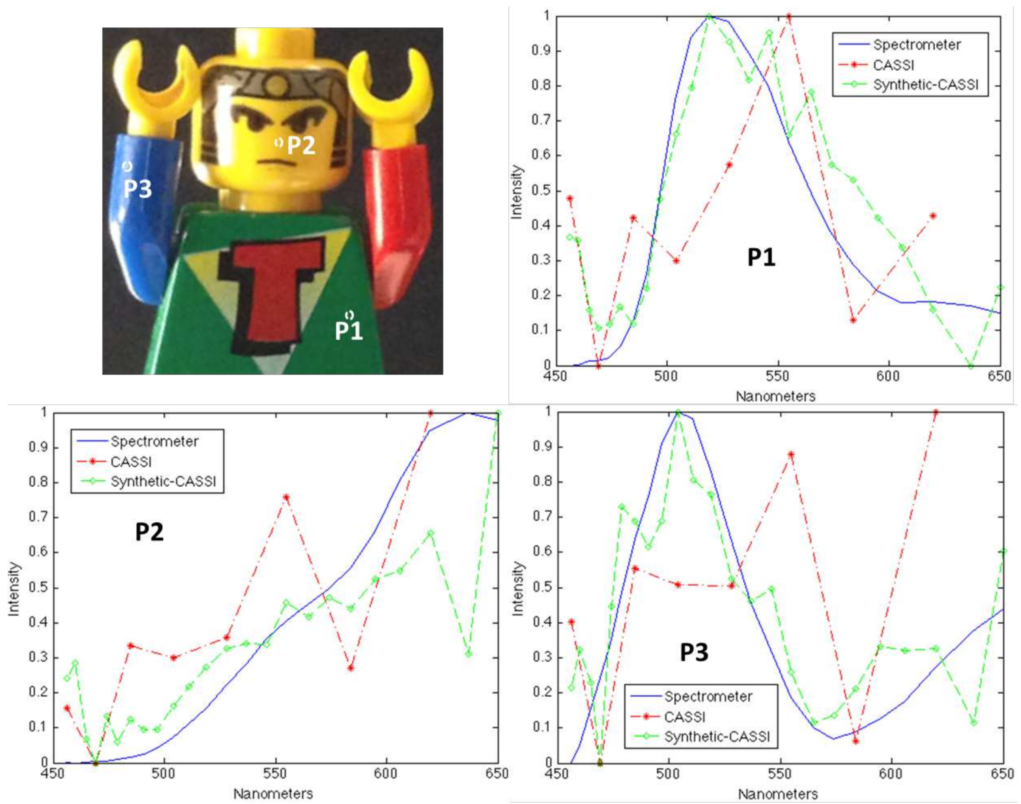

Figure 2.13: Spectral signatures of three different spatial points. Traditional CASSI and Synthetic-CASSI signatures are compared with the original spectral responses. The improved results can be noticed in the spectral signatures achieved by the Synthetic-CASSI.

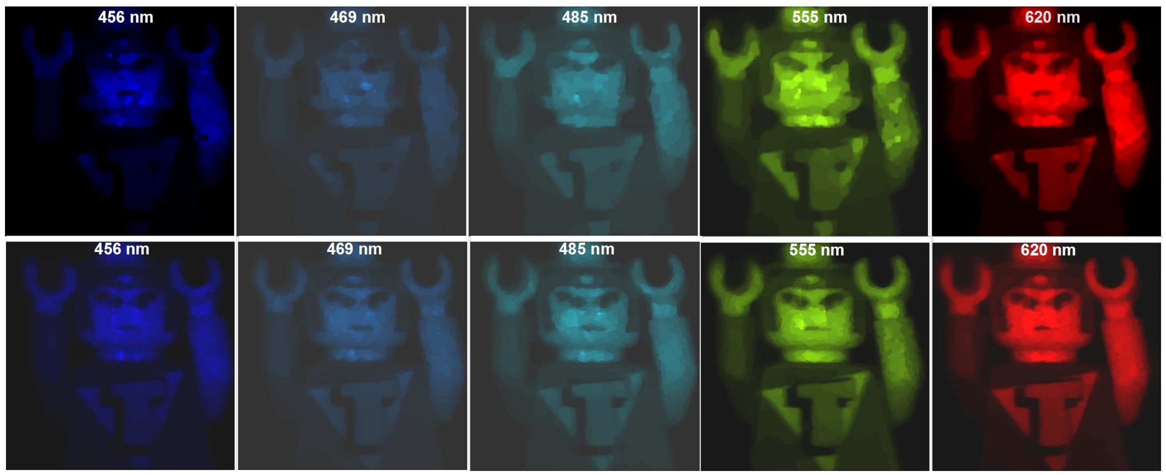

Figure 2.14: Experimental reconstructions of five spectral bands. (Up) Traditional CASSI, (Down) Synthetic-CASSI. It can be seen that Synthetic-CASSI results outperforms the results achieved by the traditional CASSI.

the resolution of the reconstructions. The model accounts two different cases of mismatching. In the first case, a super-resolution model is proposed to exploit the coded aperture resolution. In the second case, the creation of a synthetic coded aperture is proposed in order to reconstruct the spectral images, at the detector resolution. Real reconstructions show the spatial and spectral improvement achieved with the proposed model in comparison with traditional approaches of grouping pixels.

Chapter 3

CODED APERTURE DESIGN IN COMPRESSIVE SPECTRAL IMAGING BASED ON SIDE INFORMATION

Coded aperture compressive spectral imagers (CSI) sense a three-dimensional data cube by using two-dimensional projections of the coded and spectrally dispersed input image. Recently, it has been shown that combining spectral images acquired from a CSI sensor and a complementary sensor leads to substantial improvement in the quality of the fused image. To maximally exploit the benefits of the complementary information, the spatial structure of the coded apertures must be optimized inasmuch as these structures determine the sensing matrix properties and accordingly the quality of the reconstructed images. It is proposed a method to use side information from an RGB sensor to design the coded aperture patterns of a CSI imager, such that more detailed spatial images and wavelength profiles can be reconstructed. The side information is used as input of an edge detection algorithm to approximate a version of the edges of the spectral images. The coded apertures are designed to follow the spatial structure determined by the estimated spectral edges such that the high frequencies are promoted, leading to more detailed reconstructed spectral images. Simulations and experimental results indicate that when compared with random coded aperture structures, the designed coded apertures based on side information obtain up to 3dB improvement in the quality of the reconstructed images.

3.1 Introduction

Coded aperture compressive spectral imagers sense a three-dimensional data set, known as spatio-spectral data cube, by capturing two-dimensional projections of the spatio-spectral information modulated and multiplexed by a coded aperture and a dispersive element [19, 27]. These imager systems often rely on Focal Plane Arrays (FPA), Spatial Light Modulators (SLM), Digital Micromirror Devices (DMD), and dispersive elements. The use of DMDs to implement the coded apertures facilitates the capture of multiple projections, each admitting a different coded aperture pattern. Furthermore, the DMD allows to collect the sufficient number of measurements for spectrally rich scenes or very detailed spatial scenes, as well as it implement the coded apertures with elaborately designed structure to maximize the information content on the compressive measurements. The snapshots are measured by an FPA, the pixel pitch of which determines the spatial and spectral resolutions of the reconstructed images [26]. An optimization formulation resulting from the ill-conditioned linear system of equations at the detector is then used to reconstruct the data cube, using representation basis where the undersampled signals admit sparse representations. Several numerical algorithms are available to solve the resulting inverse compressive sensing problem, seeking to minimize the error with respect to the compressed measurements by means of the ℓ_2-norm, and penalizing the objective function by the ℓ_1-norm forcing the solution to be sparse.

The use of a-prior information has been extensively studied to improve the reconstruction of those undersampled signals [37, 38, 39, 40, 41]. For instance, the work in [42] takes advantage of the information about the support of the signal at the decoder for its reconstruction. In work [43], a side information (SI)-aided compressed sensing reconstruction was considered. It used a noisy version of the underlying signal, to reconstruct the original signal through a SI-aided approximate message passing (SI-AMP) algorithm. In [44], it is provided a theoretical analysis of the sufficient number of measurements for reliable recovery with high probability in the presence of prior information for both ℓ_1/ℓ_1 and mixed ℓ_1/ℓ_2 reconstruction strategies; however, the use of prior information as an additional measurement has only been recently considered. It is known as side information and is used to aid the reconstruction of signals.

In tomography, previous scans of a subject can be used as side information enabling accurate reconstruction of dynamic CT images [45]. The works in [46] and

[47] reconstructed images using a side information snapshot. Both of the methods used ℓ_1-norm based minimization for image recovery, by adding an additional term that accounts for the distance between the recovered image and the side information snapshot. Some of the works in [48, 49, 50, 51, 52] developed hybrid cameras to acquire simultaneously side RGB information in addition to multispectral imaging with low spatial resolution. In [51] for instance, the sampling patterns are generated according to the scene content in such a way that the captured hyperspectral video provides nonredundant spectrum information over frames. In terms of adaptability, in [53], it is developed a low-resolution tracking method utilizing low-resolution images captured by a traditional (i.e., non-compressive) camera as side information, which was then applied to background subtraction for video sequences.

A new approach is presented that optimally designs the set of coded apertures patterns to use in the acquisition of the compressive spectral imaging projections. In essence, the side RGB image provides a-priori information to design the coded aperture in order to sense the scene, in a structured format, such that high spatial frequency components of the spectral image are better reconstructed. The proposed method achieves superior reconstruction performance over the traditional results using random coded aperture patterns. More specifically, the edges in the scene are used to calculate new coded aperture patterns in order to better reconstruct those spatial frequencies. In addition, the side RGB information is used to improve the reconstruction quality by its use during the reconstruction process. Even more, the RGB information is used to achieve super-resolution by the use of a fusion algorithm taking advantage of the high resolution of the RGB image. So, the side RGB information is exploited twice, for both sensing and reconstruction processes. Simulations are used to illustrate the benefits of this approach. In addition, testbed reconstructions are also presented to verify the proposed coded aperture method based on the side information in a coded aperture compressive spectral imaging system.

The reminder of this chapter is organized as follows. Section 3.2 introduces the mathematical model of a known coded aperture compressive spectral imager to be used for the acquisition of compressive projections. Section 3.3 develops the spectral imaging with the side information approach. The coded aperture design method and the reconstruction process based on side information are also described in Section 3.3. Simulations as well as experimental results are presented in Section 3.4, and Section 3.5 summarizes the work.

3.2 CASSI model for spectral imaging

The coded aperture snapshot spectral imager (CASSI) captures multiplexed 2D projections of the spatio-spectral scene using a snapshot. The optical CASSI architecture consists of a coded aperture, a dispersive element, and a FPA. Figure 4.1 depicts the structure of CASSI system. The compressive spectral imager is located along the main arm. An additional arm is included in order to acquire an RGB image of the scene simultaneously; a beam splitter is used to divide the incident light into the two optical paths, the CASSI and the RGB arms. The input, a spatio-spectral data cube, is defined as $(\mathbf{F}_k)_{mn}$, where (m, n) indicates the spatial coordinates and k determines the k^{th} spectral band of an $N \times N \times L$ data cube with $m, n = 0, 1, \ldots, N-1$ and $k = 0, 1, \ldots, L-1$. The spatio-spectral images are modulated by a discretized coded aperture $\mathbf{T}^{\ell}_{mn}$, where $\ell = 0, 1, ...K-1$ indexes the number of snapshots to be captured. Notice that each snapshot uses a different coded aperture $\mathbf{T}^{\ell}$. Using this notation, the ℓ^{th} FPA measurement, referred to as $\mathbf{G}^{\ell}_{mn}$ can be written as

$$\mathbf{G}^{\ell}_{mn} = \sum_{k=0}^{L-1} \mathbf{T}^{\ell}_{m(n-k)} \left(\mathbf{F}_k\right)_{m(n-k)} . \tag{3.1}$$

The dispersion effect is modeled at the pixel level in the horizontal dimension in both the coded aperture and the source. Alternatively, the spectral signal can be expressed as $\mathbf{F} \in \mathbb{R}^{N\times N\times L}$, or its vector representation $\mathbf{f} \in \mathbb{R}^{N\cdot N\cdot L}$, which is S-sparse on a basis $\mathbf{\Psi}$, such that $\mathbf{f} = \mathbf{\Psi}\boldsymbol{\theta}$ can be approximated by a linear combination of S basis functions chosen from $\mathbf{\Psi}$ with $S \ll (N \cdot N \cdot L)$. Following this notation, the CASSI projections in Eq. 3.1 can be rewritten in the standard form of an under-determined system of linear equations

$$\mathbf{g}^{\ell} = \mathbf{A}^{\ell}\boldsymbol{\theta} = \mathbf{H}^{\ell}\boldsymbol{\Psi}\boldsymbol{\theta} + \boldsymbol{\omega}, \tag{3.2}$$

where the matrix $\mathbf{A}^{\ell} = \mathbf{H}^{\ell}\boldsymbol{\Psi}$ is the CASSI sensing matrix, $\boldsymbol{\theta}$ is a S-sparse representation of the data cube in a 3-dimensional basis $\boldsymbol{\Psi}$, and $\boldsymbol{\omega}$ represents the noise in the system. $\mathbf{H}^{\ell}$ is the system transfer function defined as $\mathbf{H}^{\ell} = \mathbf{P}\mathbf{T}^{\ell}$, its structure is determined by the coded aperture entries $\mathbf{T}^{\ell}$ and the dispersive function of the prism $\mathbf{P}$, which remains constant for all the snapshots. Hence, the size of $\mathbf{H}^{\ell}$ is $U \times Q$, where $U = N(N+L-1)$ is the number of FPA pixels and $Q = N^2L$ is the total number of data cube voxels. The set of K snapshots in Eq. 3.2 can be assembled into a single vector by concatenating the $\mathbf{y}^{\ell}$ vectors, in order to create an overall measurement vector with dimension $KU \times 1$, which is denoted as $\mathbf{g} = \left[(\mathbf{g}^0)^T, \ldots, (\mathbf{g}^{K-1})^T\right]^T$, such that $\mathbf{g} = \mathbf{H}\mathbf{f}$, where $\mathbf{H} = \left[(\mathbf{H}^0)^T, \ldots, (\mathbf{H}^{K-1})^T\right]^T$ is a $KU \times Q$ matrix. Figure 3.1 shows a sketch of the $\mathbf{H}$ matrix for an $N \times N = 4 \times 4$ spectral data cube with L bands, and $K = 2$ snapshots. The diagonals correspond to the coded aperture pattern applied to each waveband, white entries correspond to unblock elements, while black entries are blocking elements. In the sketch, 2 snapshots are vertically stacked, and the dispersion function is modeled by the shifting of the diagonal N pixels as the wavelength increases from left to right.

3.3 Spectral Imaging with Side Information

In spectral imaging, an RGB image of the same target can be captured in two distinct ways. One is to use different cameras in the same path of the spectral image and another is to split the light in two phats by using a beam splitter. The two different implementation methods are suited for different applications. For instance, in satellite or airborne imaging, the use of the same path with different cameras is suitable given that the scene is very far from the cameras and the disparity can be ignored. In contrast, if the scene is near to the camera, the disparity should be taken into account

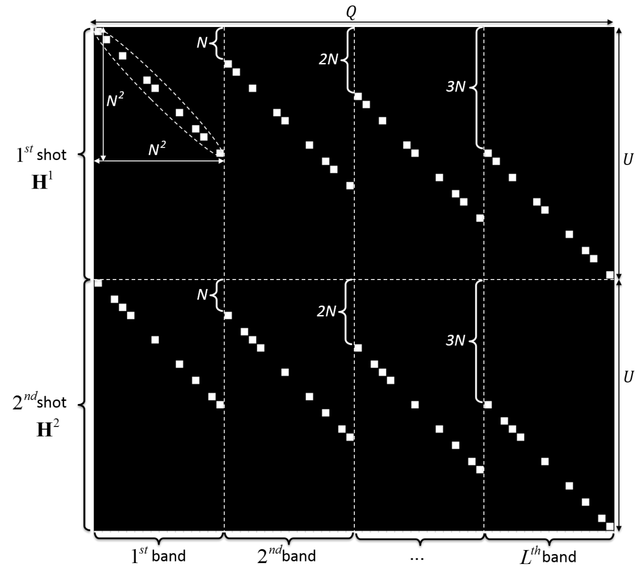

Figure 3.1: H Transfer function sketch for a $4 \times 4 \times L$ data cube, and for 2 snapshots.

and a second arm using a beam splitter will be preferable [54]. An example of the latter schematic architecture is presented in Fig. 3.2. This architecture combines a hyperspectral system and a traditional RGB imaging system by a beam splitter, which divides the incident light into two paths. After the registration of the images, the RGB image could be used as side information to aid the reconstruction of the spectral images. We propose to use the RGB information to design edge-based structured coded apertures to improve the quality of the reconstructions. The RGB information is used to adaptively configure the DMD coded aperture patterns according to different content in the scene. This is, the coded apertures implemented by the DMD can carefully sense the borders of the object, and preserve the high-frequency details in the reconstructed images.

3.3.1 Coded aperture design based on side information

Hadamard matrices, S matrices and Bernoulli random matrices are often used as coded apertures patterns for CASSI. The use of these coded apertures was motivated since they are well conditioned when used in least square estimation [55]. However,

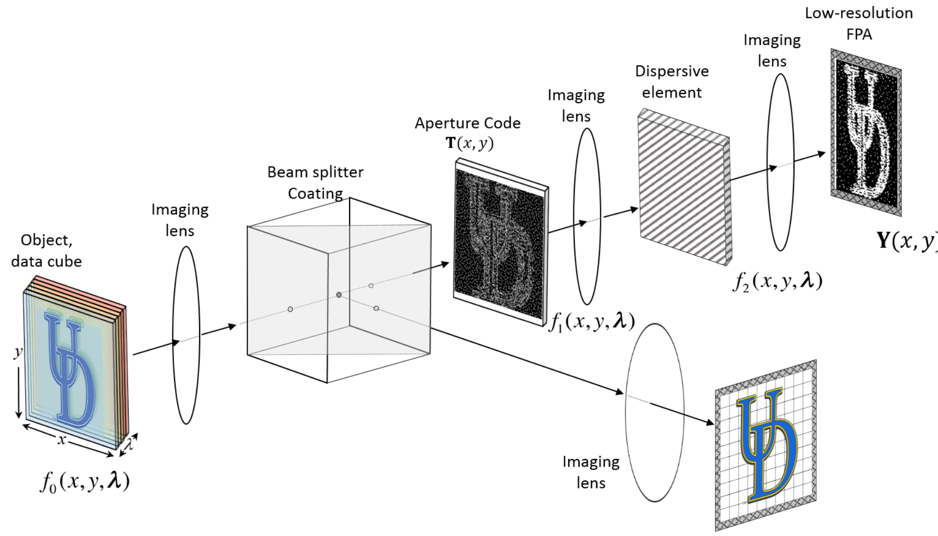

Figure 3.2: Schematic architecture of CASSI with RGB side information. A beam splitter is utilized to divide the incident light into two different directions.

these code designs do not exploit the a-priori information of the scene, even when it is available, and the properly designed coded aperture ensembles could improve the quality of the reconstruction.

In this work, the following observations are taken into account for the design of the coded aperture patterns. First, consider a traditional random coded aperture, whose entries are realizations of a Bernoulli random variable. The element values of this coded aperture are usually non-uniform distributed. This is, some areas contain more dense zero-valued pixels than other areas. In these areas, poor reconstruction of the spatial scene is expected. What is more important, if the coded aperture area with dense zero-valued pixels coincides with the high frequency components of the scene, such as the edges, then the detailed structures in the reconstructed image will be distorted or even lost. As an example, Fig. 3.3 shows the spatial reconstruction of an spectral band through simulation of the CASSI system using a random coded aperture pattern and focusing on an specific area where the scene presents high frequency components. The coded apertures using these random patterns try to sense in an unstructured way regardless the specific shapes of the underlying objects; however, the scenes of objects or images are not usually uniform. Instead, they contain intensity variations, intensity discontinuities in some directions and uniform/non-uniform patches.

The spatial quality of the reconstructed spectral image is affected mainly in the sections containing numerous details. More specifically, the edges of the objects in the scene are poorly reconstructed using traditional coded apertures, such as random and hadamard coded apertures. One reconstructed band is presented in Fig. 3.3 (a). For the simulation, the data cube is sensed by the CASSI system using a random coded aperture with a transmittance of 50%. The toy chest highlights the poor reconstruction of the edges. The corresponding original section is presented in a green square in order to visually compare the quality. In order to evaluate the reconstruction performance at the edges of the object in the scene, the edges are first estimated from an RGB image of the data cube through the widely known Canny edge detector method [56], which will be described afterwards. The estimated edges can be seen in Fig. 3.3 (b). In order to evaluate the error localized at the edges, for the 484 nm spectral band, the absolute value of the reconstruction error is calculated and overlapped with the edges estimated before. The yellow pixels in Fig. 3.3 (b) correspond to errors localized on the edges. The ratio of error on edges over the overall energy of the original image is 19.84% for the 484 nm spectral band.

3.3.1.1 Edge estimation based on the RGB image

The previous observations motivate us to design coded apertures based on the side information to enhance the reconstruction quality of the spectral data cube. More formally, the k^{th} spectral bands of the spatio-spectral image $(\mathbf{F}_k)_{mn}$, can be compactly rewritten as $\mathbf{F}_k = (\mathbf{F}_k)_{mn}$. In order to take advantage of the a-priori information, an RGB image $\mathbf{F}_C$ is used to design edge-based coded aperture patterns. Each RGB image channel can be written as,

$$\mathbf{F}_R = \sum_{k=0}^{L-1} \mathbf{w}_k^R \mathbf{F}_k, \quad \mathbf{F}_G = \sum_{k=0}^{L-1} \mathbf{w}_k^G \mathbf{F}_k, \quad \mathbf{F}_B = \sum_{k=0}^{L-1} \mathbf{w}_k^B \mathbf{F}_k, \tag{3.3}$$

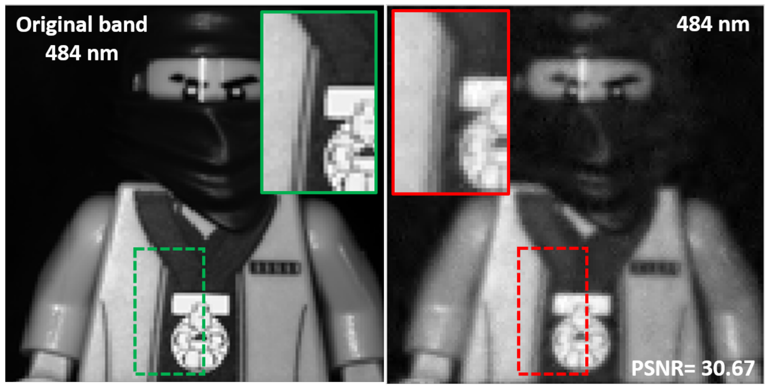

(a)

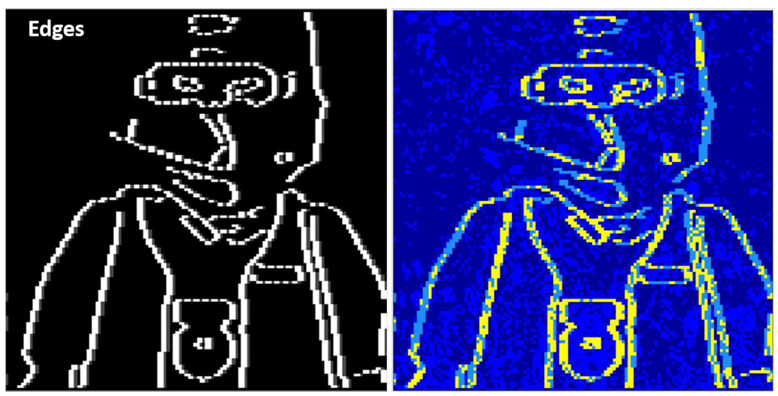

(b)

Figure 3.3: (a) A spectral band is reconstructed through simulation of the CASSI system using a random coded aperture pattern. Zoomed sections of the original and reconstructed band are presented in green and red squares. (b) Edge estimation using the Canny method and correlation between the reconstruction error and the estimated edges for the spectral band reconstructed in (a).

where $\mathbf{w}_k^R, \mathbf{w}_k^G, \mathbf{w}_k^B > 0$, are the spectral responses of the CCD sensor for the R,G,B channels, respectively. The RGB image is composed by the three channels, such that $\mathbf{F}_C = \mathbf{F}_R + \mathbf{F}_G + \mathbf{F}_B$.

Given $\mathbf{F}_C$, an edge detection process is carefully applied to establish the key spatial frequencies on the image to improve its reconstruction. The edge detection process is then performed using the Canny edge detector method [56], based on optimizing the trade-off between the following two performance criteria: good edge detection, which means low probabilities to loose the real edges or generate artificial edges in the flat area, and good edge localization, which means the positions of edge points marked by the edge detector should be as close to real edges as possible.

A noise reduction is first implemented by convolving the RGB image $\mathbf{F}_C$ with a Gaussian mask $\mathbf{G}(\sigma) \in \mathbb{R}^{r\times r}$, where σ is the spread of the Gaussian filter and controls the degree of smoothing, and the ideal value for r is the smallest odd integer greater than 6σ [57]. The smoothed RGB image is calculated as $\hat{\mathbf{F}}_C = \mathbf{G}(\sigma) * \mathbf{F}_C$. Where $*$ represents the convolution operation. The size of the resulting image is fixed to be the same as the original image size.

The partial derivatives $\partial\hat{\mathbf{F}}_C/\partial x$ and $\partial\hat{\mathbf{F}}_C/\partial y$ at every pixel location in the RGB image are calculated to compute the intensity gradient of the image. These derivatives can be implemented by filtering the smoothed image $\hat{\mathbf{F}}_C$ with a gradient operator $\mathbf{S}$, such as the Prewitt or Sobel 2D masks of size 3×3, in order to obtain the intensity gradient image $\mathbf{S}_C$,

$$\begin{aligned}
\mathbf{S}_C &= \mathbf{S} * \hat{\mathbf{F}}_C = \mathbf{S} * \hat{\mathbf{F}}_R + \mathbf{S} * \hat{\mathbf{F}}_G + \mathbf{S} * \hat{\mathbf{F}}_B \\
\mathbf{S}_C &= \mathbf{S} * \sum_{k=0}^{L-1} \mathbf{w}_k^R \hat{\mathbf{F}}_k + \mathbf{S} * \sum_{k=0}^{L-1} \mathbf{w}_k^G \hat{\mathbf{F}}_k + \mathbf{S} * \sum_{k=0}^{L-1} \mathbf{w}_k^B \hat{\mathbf{F}}_k \\
\mathbf{S}_C &= \sum_{k=0}^{L-1} \mathbf{w}_k^R \left(\mathbf{S} * \hat{\mathbf{F}}_k\right) + \sum_{k=0}^{L-1} \mathbf{w}_k^G \left(\mathbf{S} * \hat{\mathbf{F}}_k\right) + \sum_{k=0}^{L-1} \mathbf{w}_k^B \left(\mathbf{S} * \hat{\mathbf{F}}_k\right),
\end{aligned} \tag{3.4}$$

where $\hat{\mathbf{F}}_R$, $\hat{\mathbf{F}}_G$, and $\hat{\mathbf{F}}_B$ are the smoothed versions of the RGB image channels in Eq. 3.3.

The intuition behind the use of the edges is that it is possible to approximate the edges of the spectral data cube from the RGB image, and that information could be used to design the coded apertures. In order to verify that insight, the edge detection process is also applied to the complete spectral data cube. First, the noise reduction for the complete spectral scene is calculated as $\hat{\mathbf{F}}_k = \mathbf{G}(\sigma) * \mathbf{F}_k$, and the intensity gradient image $\mathbf{S}_T$ for the complete data cube is given by,

$$\mathbf{S}_T = \mathbf{S} * \hat{\mathbf{F}}_k = \mathbf{S} * \sum_{k=0}^{L-1} \mathbf{w}_k \hat{\mathbf{F}}_k = \sum_{k=0}^{L-1} \mathbf{w}_k \left(\mathbf{S} * \hat{\mathbf{F}}_k \right). \tag{3.5}$$

From Eq. 3.4, it can be seen that $\mathbf{S}_C$ contains a weighted sum of the edges of the spectral bands. Thus, $\mathbf{S}_C \approx \mathbf{S}_T$. Then, the edges estimated from the RGB image could be seen as an approximation of the edges of the complete spectral scene.

3.3.1.2 Coded aperture calculation

The coded apertures are designed as the Hadamard product of two components. The first component is a blue noise pattern generated by using a blue noise mask. The second component is the edge component. The blue noise patterns are selected since they exhibit the high-frequency component that suppresses low-frequency components of white noise, producing patterns of pixels distributed as homogeneously as possible [58, 59, 60]. This feature helps to achieve a more uniform sensing than that obtained with random patterns as verified in several works [61, 62]. The coded aperture $\mathbf{T}$ is then calculated as,

$$\mathbf{T} = \mathbf{T}_{b1} \cdot \mathbf{T}_e + \mathbf{T}_{b2} \cdot (1 - \mathbf{T}_e), \tag{3.6}$$

where $\mathbf{T}_{b1}$ and $\mathbf{T}_{b2}$ are two blue noise patterns with different transmittance. The transmittance is defined as the percentage of light intensity passing through the coded aperture among the overall intensity. $\mathbf{T}_e$ is the edge component. $(1 - \mathbf{T}_e)$ guarantees that each pixel in the edge component is classified as part of the edges or the background, defined as the scene complement of the edges. The pre-calculated image $\mathbf{S}_C$

in Eq. 3.4 is used as the edge component, thus $\mathbf{T}_e = \mathbf{S}_C$. Then the coded aperture in Eq. 3.6 can be re-written as,

$$\mathbf{T} = \mathbf{T}_{b1} \cdot \mathbf{S}_C + \mathbf{T}_{b2} \cdot (1 - \mathbf{S}_C). \tag{3.7}$$

The transmittance of the blue noise patterns $\mathbf{T}_{b1}$ and $\mathbf{T}_{b2}$ must be different, otherwise, the coded aperture will be a blue noise pattern sensing the whole scene.

In order to improve the reconstruction of the edges, the coded aperture in Eq. 3.1 is replaced by coded in Eq. 3.7, the FPA measurement for one snapshot can be seen as,

$$\mathbf{G}_{mn} = \sum_{k=0}^{L-1} \Big((\mathbf{T}_{b1})_{m(n-k)} (\mathbf{S}_C)_{m(n-k)} + (\mathbf{T}_{b2})_{m(n-k)} (1 - \mathbf{S}_C)_{m(n-k)} \Big) (\mathbf{F}_k)_{m(n-k)} \,. \tag{3.8}$$

Expanding Eq. 3.8, the measurements can be seen as the sum of the sensed edges and the sensed background:

$$\mathbf{G}_{mn} = \underbrace{\sum_{k=0}^{L-1} (\mathbf{T}_{b1})_{m(n-k)} (\mathbf{S}_C)_{m(n-k)} (\mathbf{F}_k)_{m(n-k)}}_{a} + \underbrace{\sum_{k=0}^{L-1} (\mathbf{T}_{b2})_{m(n-k)} (1 - \mathbf{S}_C)_{m(n-k)} (\mathbf{F}_k)_{m(n-k)}}_{b} \,. \tag{3.9}$$

Figure 3.4 presents a comparison between the edge estimation $\mathbf{S}_C$ obtained from $\hat{\mathbf{F}}_C$ and the real edges $\mathbf{S}_T$. Figure 3.4 shows that 87% (yellow pixels) of the edges are correctly estimated from the RGB image. The coded aperture $\mathbf{T}$ then tries to emphasizes the edges of the spectral bands thus is more beneficial to preserve the high frequency details in the reconstructed spectral images.

3.3.2 Reconstruction process

The CASSI with side information approach results in two measurements shots: the RGB image $\mathbf{F}_C$ acquired by the RGB detector, and the CASSI measurements

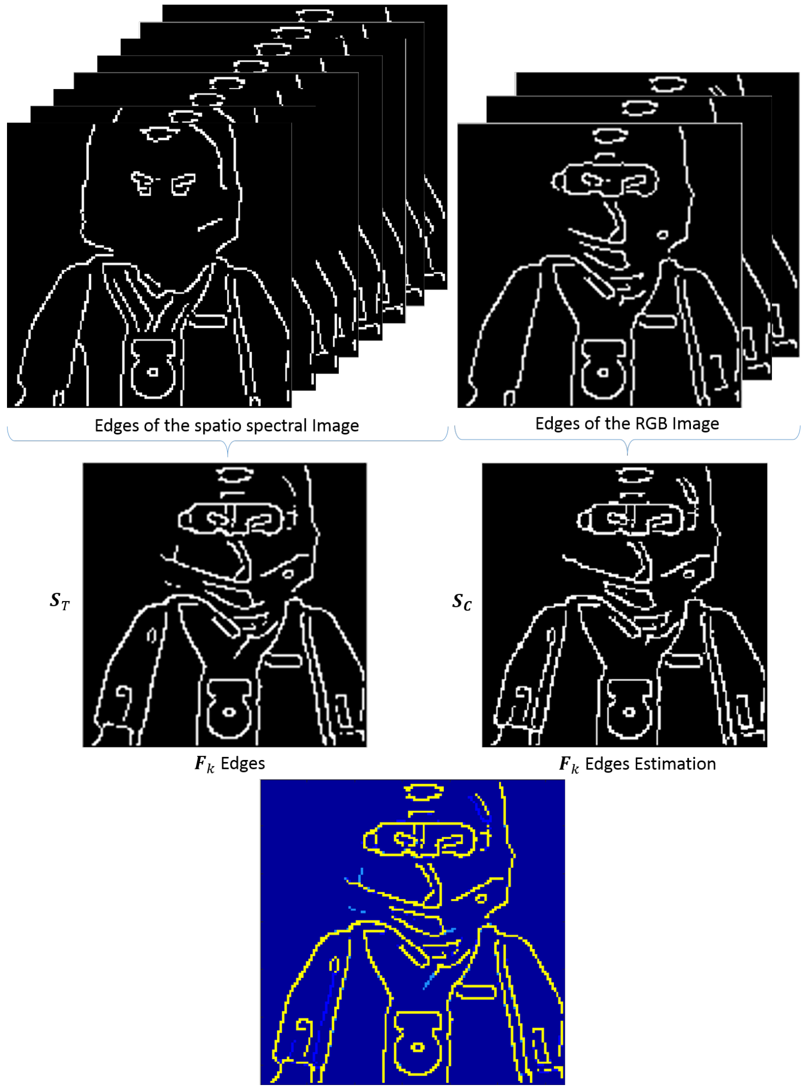

Figure 3.4: Edge Calculation for the $\mathbf{F}_k$ spatio-spectral image for $k = 8$. The edge estimation $\mathbf{S}_C$ using the RGB image is compared with the real edges $\mathbf{S}_T$. Edges of each band are calculated and then summed for both the complete data cube and the RGB image. An error image is created to show that pixels in yellow (87%) are correctly estimated from the RGB image $\mathbf{F}_C$.

captured using the designed coded aperture, corresponding to Eq. 3.9. In order to reconstruct the spatio-spectral data cube, the two measurements are stacked together such that the final measurements are given by $\tilde{\mathbf{g}} = \tilde{\mathbf{H}}\mathbf{f} + \tilde{\boldsymbol{\omega}}$, where

$$\tilde{\mathbf{g}} = \begin{bmatrix} \mathbf{g}' \\ \mathbf{g} \end{bmatrix}, \quad \tilde{\mathbf{H}} = \begin{bmatrix} \mathbf{H}' \\ \mathbf{H} \end{bmatrix}, \quad \tilde{\boldsymbol{\omega}} = \begin{bmatrix} \boldsymbol{\omega}' \\ \boldsymbol{\omega} \end{bmatrix}, \tag{3.10}$$

where $\mathbf{g}' = \mathbf{H}'\mathbf{f} + \boldsymbol{\omega}'$ corresponds to the linear representation of the RGB measurement, the matrix $\mathbf{H}'$ is the system forward response of the RGB camera, and $\mathbf{y}$ represents the CASSI shot. $\tilde{\boldsymbol{\omega}}$ accounts for the additive noise of the two detectors, generally modeled as white Gaussian noise.

An estimation of the spatio-spectral data cube can be attained by solving the regularization problem,

$$\hat{\mathbf{f}} = \boldsymbol{\Psi}\{\text{argmin}_{\theta}\|\tilde{\mathbf{g}} - \tilde{\mathbf{H}}\boldsymbol{\Psi}\boldsymbol{\theta}\|_2 + \tau\|\boldsymbol{\theta}\|_1\}, \tag{3.11}$$

where $\boldsymbol{\theta}$ represents an S-sparse representation of $\mathbf{f}$, and τ is a regularization constant. The basis representation $\boldsymbol{\Psi}$ is formulated as the Kronecker product of two bases $\boldsymbol{\Psi} = \boldsymbol{\Psi}_1 \bigotimes \boldsymbol{\Psi}_2$, where $\boldsymbol{\Psi}_1$ is a 2D wavelet Symmlet 8 basis and $\boldsymbol{\Psi}_2$ playing the role of spectral sparsifier is a the 1D discrete cosine transform. Different algorithms have been proposed to solve the optimization problem in Eq. 3.11, including the two-step iterative shrinkage/thresholding (TwIST) [21], the gradient projection for sparse reconstruction (GPSR) [22], Gaussian mixture models (GMM) [23], and the compressive imaging reconstruction algorithm based on the approximate message passing (AMP) framework [24]. The GPSR algorithm was used, although any of the other algorithms could be used as well.

With the aim to enhance the reconstructed spatio-spectral data cube $\hat{\mathbf{f}}$, a data fusion algorithm is applied after reconstruction taking advantage of the acquired RGB

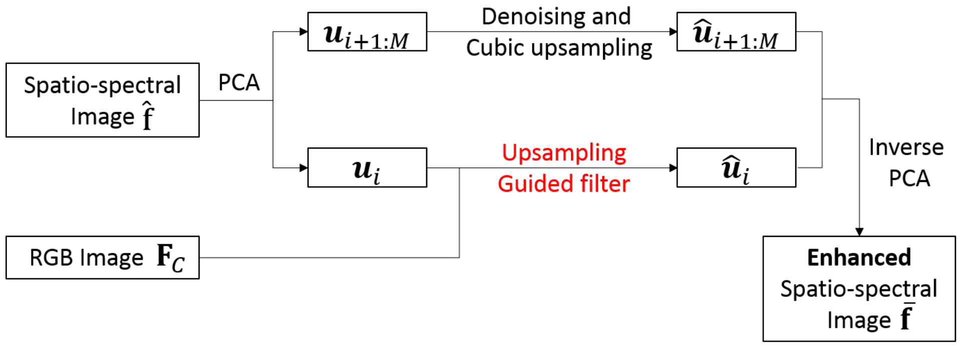

Figure 3.5: Fusion of the spatio-spectral image $\hat{\mathbf{f}}$ and RGB image $\mathbf{F}_C$ with the GF-PCA framework.

image $\mathbf{F}_C$. More specifically to the fact that high resolution RGB detectors are cheaper than FPAs, it is lower-cost to acquire high resolution side information images than spectral measurements. Hence, the guided filter principal component analysis (GFPCA) algorithm is used. The goal of the data fusion algorithm is to enhance the resolution of the reconstructed spectral data cube as well as its spatial quality. The general idea of the GFPCA is to calculate the principal components of $\hat{\mathbf{f}}$ using PCA. Then, apply a guided filter [63] over the first i principal components of the data cube, given that those contain the most useful information. For the other components, a denoising process and a cubic upsampling is performed first. Then both resulting principal components are stacked again, and an inverse PCA is applied to obtain the enhanced spatio-spectral image $\bar{\mathbf{f}}$. Figure 3.5 shows the GFPCA framework that uses the $\mathbf{F}_C$ image to guide the filtering process aiming at obtaining super-resolution.

Within this framework, the guided filtering applied to the $\mathbf{u}_i$ principal components to calculate $\hat{\mathbf{u}}_i$, can be represented as an affine transformation of the guidance image $\mathbf{F}_C$ in a local and sliding window w_j as,

$$\hat{\mathbf{u}}_i = a_j \mathbf{F}_C + b_j, \quad \forall i \in w_j, \tag{3.12}$$

where a_j and b_j are some linear coefficients assumed to be constant in the window w_j. Eq. 3.12 ensures that the output $\hat{\mathbf{u}}_i$ has an edge only if the guided image $\mathbf{F}_C$ has an edge, since $\nabla(\hat{\mathbf{u}}_i) = a\nabla\mathbf{F}_C$. The cost function to determine the coefficients a_j and b_j is given by,

$$E(a_j, b_j) = \sum_{i\in w_j} \left[(a_j\mathbf{F}_C + b_j - \mathbf{u}_i)^2 + \epsilon a_j^2 \right], \tag{3.13}$$

where ϵ is a regularization parameter to determine the degree of blurring for the guided filter. The cost function in Eq. 3.13 leads the term $a_j\mathbf{F}_C + b_j$ to be as close to $\mathbf{u}_i$ as possible, such that it is ensured the preservation of the spectral information. The solution to the cost function in Eq. 3.13 is given by a linear regression that gives the a_j and b_j coefficients in terms of the mean and variance of the guiding image, the number of pixels $|w|$ and the mean of the principal components in the window w_j. This linear model is applied to all the local windows in the principal components. After the filtering process, all the principal components are stacked into $\hat{\mathbf{u}}$, and the inverse PCA transformation is applied to obtain the enhanced spatio-spectral image $\overline{\mathbf{f}}$.

3.4 Simulations and Results

3.4.1 Simulations

In order to verify the CASSI with side information approach, two sets of compressive measurements are simulated using the forward model in Eqs. 3.2 and 3.9, adding Gaussian noise with zero mean to the measurements $\mathbf{Y}$. The sets correspond to the CASSI with side information, but the first set is modulated by a random coded aperture and the second by the designed coded aperture. For the simulations, a test spectral data cube $\mathbf{F}$, acquired using a monochromator in the spectral range between 450 nm and 650 nm with 128×128 pixels of spatial resolution and $L = 8$ spectral bands is used. A CCD camera AVT Marlin F0033B, with 656×492 pixels and a pixel pitch size of 9.9 μm is used. The spatial resolution of the coded apertures $\mathbf{T}, \mathbf{T}_{b1}$ and $\mathbf{T}_{b2}$ is 128×128 pixels, and the transmittances of $\mathbf{T}$, $\mathbf{T}_{b1}$ and $\mathbf{T}_{b2}$ are 0.25, 0.22 and 0.26, respectively. The coded aperture designed using the CASSI with side information approach has a final transmittance of $\mathbf{T} = 0.25$ and it is presented in fig. 3.6 (left), the

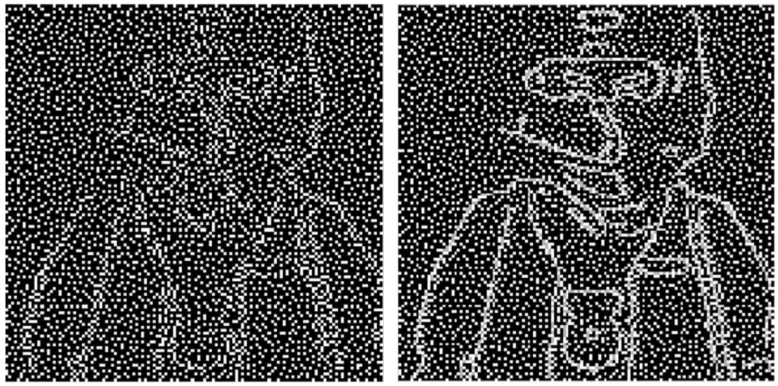

Figure 3.6: (Left) Designed coded aperture with transmittance $T = 0.25$. (Right) Estimated edges overlapping the designed coded aperture to visualize edge component.

estimated edges are overlapped with the coded aperture in fig. 3.6 (right) to facilitate the visualization of the edge component.

The compressive sensing gradient projection for sparse reconstruction (GPSR) algorithm is used to obtain the reconstructions of the data cube [22]. Figure 3.7 illustrates four spectral bands of the original data cube and the respective reconstructions. The left column presents the original bands. The second column shows the reconstruction of the set of measurements simulated using model in Eq. 3.2, and a random coded aperture. The third column shows the reconstruction of the set of measurements simulated using model in Eq. 3.9 with the designed coded aperture in Fig. 3.6. The compressive reconstruction algorithm for both sets of measurements takes into account the RGB information, and a SNR level of 8 dB of noise is also added in the measurements. The spatial quality is improved when the designed coded aperture is used, and it can be easily noticed. Observe that the spatial quality of the borders is specially enhanced.

Figure 3.8 shows the mean spectral PSNR for the reconstructed eight bands. The improvement reached by using the designed coded aperture is superior than the improvement achieved using a random coded aperture for all the bands. Moreover, the spectral signature for two spatial points, indicated as P1 and P2 in Fig. 3.8, are

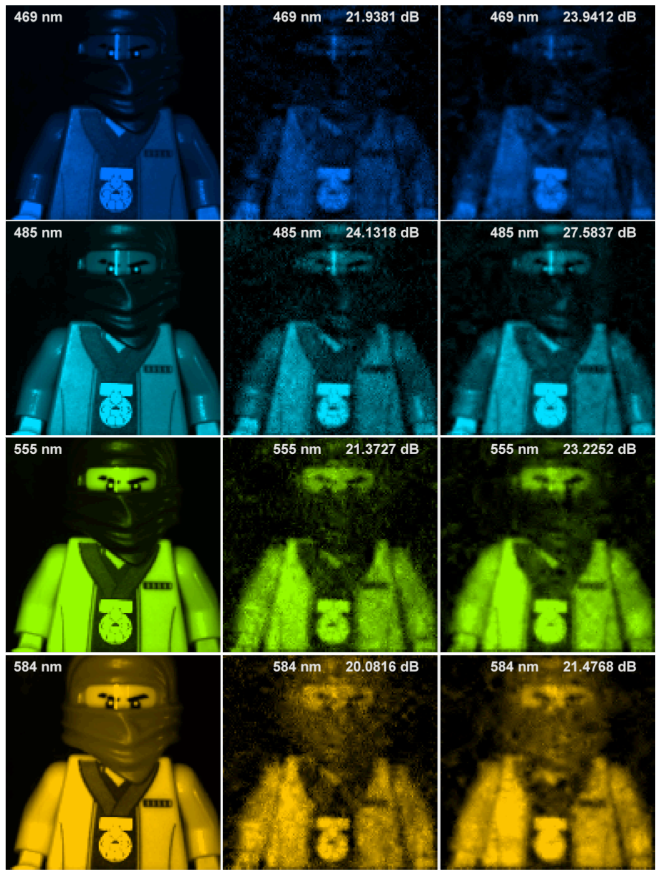

Figure 3.7: Reconstruction of four spectral bands using the CASSI with side information. Left column depicts the original bands, second column shows the reconstruction using a random coded aperture and the third column shows the reconstruction using the designed coded aperture in Fig. 3.6.

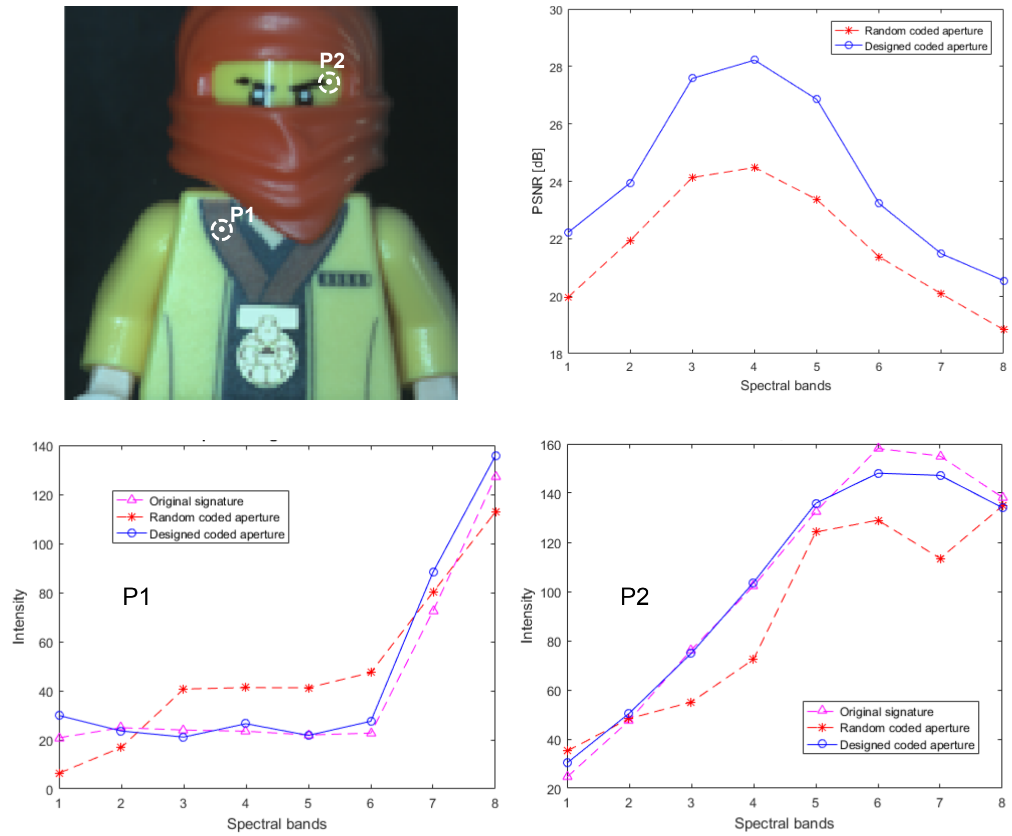

Figure 3.8: Mean spectral PSNR for the eight reconstructed bands and spectral signatures for two representative spatial points, indicated as P1 and P2.

evaluated and compared with the original profile. As can be noticed, the use of designed coded apertures provides more accurate reconstructed profiles than the use of random coded apertures.

3.4.2 Experimental Results

The CASSI system was experimentally realized to demonstrate the proposed design method of the coded aperture based on side information. The coded apertures were implemented in a Texas Instruments D1100 DMD (DLP), a custom double Amici prism (Shangai Optics) was used as a dispersive element, and an FPA detector (Stingray F-033B) captured the measurements. The nonlinear dispersion curve of the prism was determined experimentally by using a monochromator. The DMD used to implement the coded apertures has a resolution of 1024×768 and a mirror pitch size of 13.68 μm. The FPA detector used in this experimental setup has a resolution of 1280×960 pixels and a pitch size of 6.45 μm. A Pike F-145 RGB camera with a Sony ICX285 sensor was used to acquire the RGB side image. The camera has a resolution of 1388×1038 pixels and a pitch size of 6.45 μm. The resulting resolution of the RGB images is 512×512 pixels.

Two sets of compressive measurements were acquired by using the CASSI optical setup for two different targets. Figure 3.9 shows the real scenes used in the experiments. The first set of compressive measurements was modulated by a random coded aperture, and the second, by the proposed designed coded aperture. In order to design the coded apertures, a re-sized version of the RGB image with 128×128 pixels was used to estimate the borders of the scene according to Eq. 3.4. Then, two blue noise patterns with transmittances $\mathbf{T}_{b1}, \mathbf{T}_{b2} \in [0.40, 0.80]$ were used to calculate the designed coded aperture $\mathbf{T}$ with a final transmittance of 0.25. The designed coded apertures for the two scenes are presented in the bottom row of Fig. 3.9. The spatial resolution of the scenes, coded apertures, and respective reconstructions is 128×128 pixels. The number of resolvable bands was $k = 10$. The GPSR algorithm was used to recover the spatio-spectral data cube using the RGB side information as formulated in Eq. 3.10.

The spatial reconstructions for the scenes are shown in Fig. 3.10 and 3.11. Figure 3.10 illustrates three reconstructed bands of Target 1, for both random and designed coded apertures. The quality on the borders of the reconstructed bands using the designed coded apertures clearly outperforms the results attained with the random

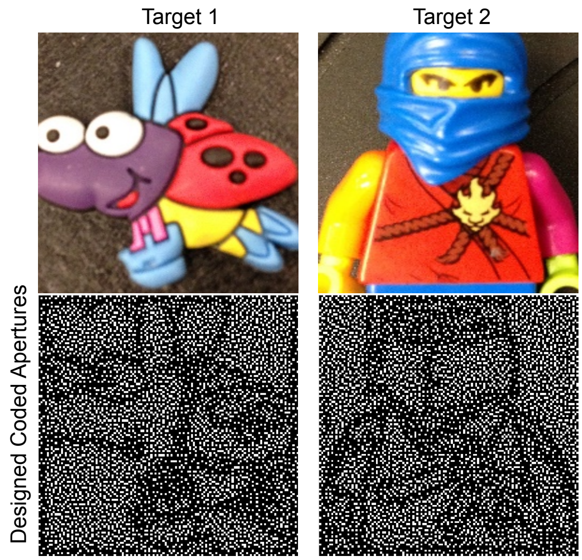

Figure 3.9: (Top) Two real scenes used to show the performance of the approach. (Bottom) Designed coded apertures using the side information for the two targets.

coded aperture. Figure 3.11 shows three reconstructed bands of Target 2. Notice the quality improvement achieved at the borders of the object in the scene.

Figure 3.12 shows the spectral signatures for two points randomly chosen from reconstruction of target 2. The points are indicated as P1 and P2. The original signature, obtained using a commercially available spectrometer (Ocean Optics USB2000+) is compared with the spectral reconstruction based on side information using the random and the designed coded apertures. The curves obtained by using the CASSI with side information and coded aperture design are closer to the original signatures. A zoomed version of the toy chest is also shown to highlight the quality at the borders.

3.4.3 Reconstruction Enhancement

The GFPCA data fusion algorithm was applied in order to enhance the reconstructed spatio-spectral data cube $\hat{\mathbf{f}}$. The full 512×512 RGB image is used as the guided image. The first four principal components were used to apply the guided filter, the local sliding window for the filtering is 25, and the regularization parameter

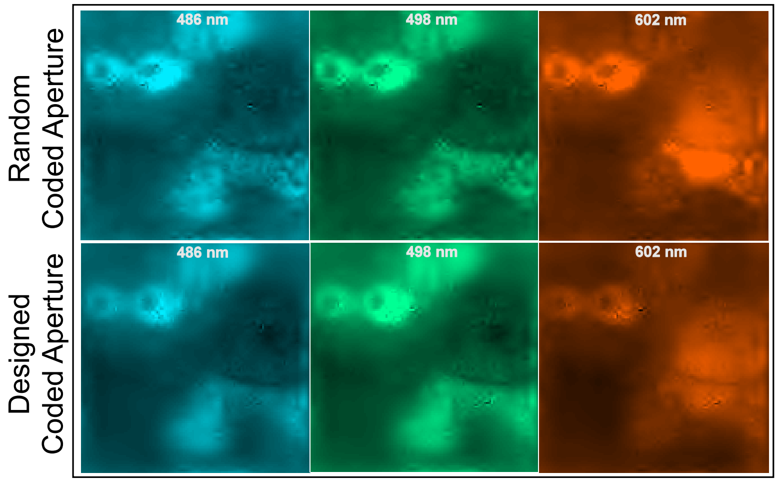

Figure 3.10: Reconstruction of 3 bands for Target 1 (Top) Using random coded aperture. (Bottom) Using designed coded aperture.

is $\epsilon = 10^{-5}$. Figure 3.13 presents the high resolution reconstruction of simulations scene and Target 2. The RGB mapping of the recovered spectral data cubes can be compared to the original scenes in Figs. 3.8 and 3.9 respectively. Four reconstructed and enhanced spectral bands are also presented to visualize the quality improvement. The final resolution of the enhanced versions is $256 \times 256 \times 8$ and $512 \times 512 \times 10$ respectively. The improvements of the resolution and image quality for the spectral bands and entire data cube can be easily noticed.

3.5 Conclusions

A coded aperture design method based on side information has been developed. The method and designs were experimentally demonstrated in a compressive spectral imaging architecture. The use of side information and specifically the estimation of the borders of the scene allows the coded aperture design and promotes a high quality reconstruction, specially the high frequency components in the scene. The quality achieved is given by the coded aperture design in the sensing process and the use of the side information during the reconstruction process. After reconstruction, a super-resolution algorithm takes advantage of the high spatial resolution of the RGB image.

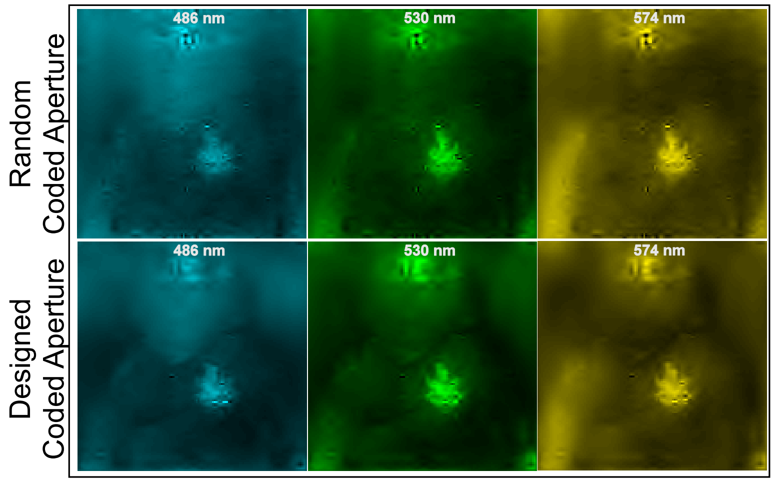

Figure 3.11: Reconstruction of 3 bands for Target 2 (Top) Using random coded aperture. (Bottom) Using designed coded aperture.

Simulations and experimental results demonstrate the performance of the proposed method as well as the super-resolution results.

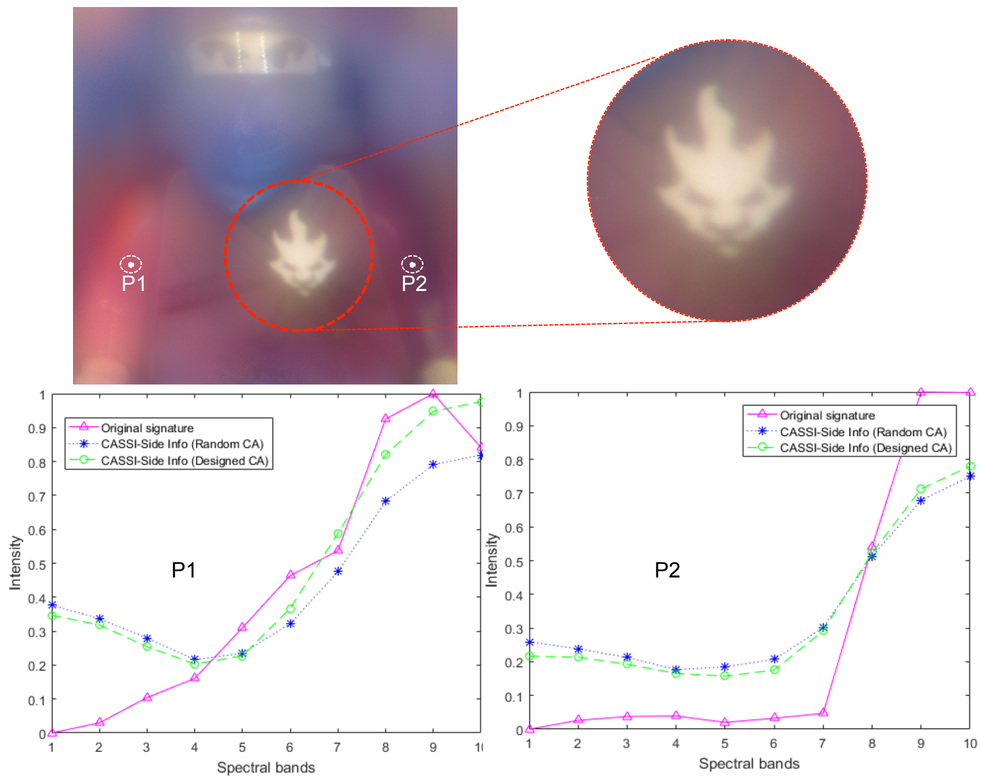

Figure 3.12: Spectral reconstruction of a red (P1) and purple (P2) spatial points. The spectral profiles for CASSI with side information using random coded aperture and CASSI with side information using designed coded aperture are depicted to compare the spectral reconstruction. A zoomed version of the toy chest is shown to highlight the quality at the borders.

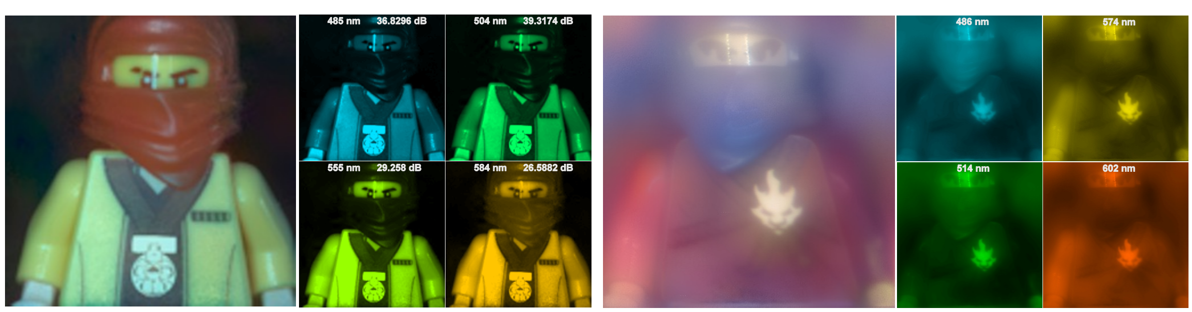

Figure 3.13: High resolution reconstruction of simulations scene and Target 2. The spatial resolution of the reconstructions is 256×256 and 512×512 respectively. The RGB image is fused with the low resolution reconstruction to increase the spatial resolution of the enhanced final version. An RGB profile is also shown for the two scenes.

Chapter 4

SHIFTING COLORED CODED APERTURE DESIGN FOR SPECTRAL IMAGING

4.1 Introduction

Spectral images can be described as images with spatial information across a large number of wavelengths. Despite the many applications of spectral information such as quality control in food and industrial agriculture [1, 2], medical imaging [3, 4, 5, 6], remote sensing [7, 8, 9], art conservation [10, 11, 12, 13], gas identification [14, 15], security applications [14, 15], between others [16], the implementation of spectral sensing systems and the subsequent acquisition and processing of data pose significant challenges. Most common spectral imaging (SI) systems generally exploit a full sampling scheme, which effectively sense a full spatio-spectral data cube at the expense of a time-consuming acquisition. As a result, a full sampling scheme can only be usefully applied to static scenes or scenes with slow movement [64]. Compressive sensing (CS) handles these challenges effectively, and it has been a powerful framework to acquire large amount of data with fewer measurements than those required by the well known Shannon-Nyquist sampling theorem [16].

The increasing interest of CS theory in spectral imaging has generated the development of many compressive spectral imaging (CSI) systems [65, 64] such as the multi-aperture filtered camera (MAFC), coded aperture snapshot spectral imager (CASSI), and snapshot hyperspectral imaging Fourier transform (SHIFT). CSI measures spatio-spectral information in such a way that the data cube is sensed and compressed at the same time. In fact, this spatio-spectral information is acquired in the form of two-dimensional (2D) projections at the detector [66]. Despite the differences in each implementation, these methods share the attempt to perform direct 2D measurements, where each point from the scene is mapped to a single point in the optical sensor [65]. The main components of these architectures are Focal Plane Arrays (FPA), Spatial Light Modulators (SLM), Digital Micromirror Devices (DMD), and dispersive elements [64].

The acquisition of 2D projections is realized by coded aperture compressive spectral imagers, which sense the data cube by means of the spatio-spectral information modulation by a coded aperture (CA) and multiplexing by a dispersive element [16]. The CA can be implemented by a photomask with a permeability to block or let pass the light in a single narrow or a wide spectral band or with the use of DMDs. In particular, the CASSI attracts the interest due to its capability to capture the 2D measurements using a single exposure or snapshot, turning the 3D incoming information into a 2D distribution [16]. However, the reconstruction of spectral scenes with very detailed spatial information requires more than a single-shot CASSI measurement since it does not provide enough information, as a response, the multi-frame CASSI takes multiple shots of the same scene with different CAs [62].

Traditionally, the coded apertures are proposed as matrices, whose entries are realizations of a Bernoulli random variable, Hadamard matrices, S-matrices and cyclic S matrices obtained by cyclic permutations of a codeword, and these distributions have shown to obtain good reconstructions, and have been widely used [19, 55, 67]. These results have been improved by replacing the traditional block-unblock CA by multi-patterned arrays of selectable optical flters or colored coded apertures (CCA) allowing to modulate the data cubes both spatially and spectrally [68]. Even more, some recent works have been reported in which the authors attempt to find an optimal structure for the coded aperture in an explicit or implicit way, with the aim to increase the reconstruction quality and/or in order to take fewer measurements, revealing the benefits of optimal sampling applied in conjunction with CS [69, 68, 70, 71, 72]. A major trend however, focuses on the mutual coherence, where the sensing matrix is desired to be as incoherent as possible with the sparsifying matrix. Singular value decomposition [69, 73], genetic algorithms [68], adaptive schemes [74, 75], shrinkage methods [69], among others approaches [76, 77] have been proposed.

More computational-based approaches to optimize the measurement matrix have been also proposed. For instance, in Ref. [78], a gradient-based method is used to design the measurement matrix by changing the location and distribution of the blocking elements, having into account the coherence of the sensing matrix. In Ref. [79], it is proposed an algorithm that iteratively constructs the sparsifying dictionary and the projection matrix. Another work is found in Ref. [80], where the optimal solution of the optimization function that minimizes the Frobenius norm of the difference between the Gram matrix and the identity matrix is calculated.

In this work, a colored coded aperture design is proposed through a minimization problem of the Frobenius norm to enhance the orthogonal criteria by rows and columns, allowing the possibility to vary the distribution while an uniform sensing through the shots is realized. The spatial distribution and the uniformity of sensed information in each spectral band is likewise reduced in their norms. It is noteworthy that the gradient descent algorithm proposed to solve the optimization problem, offers a non-binary matrix response, for this reason, it is included a thresholding operator to binarize the response that minimizes the problem. A compensating trade-off strategy between the uniformity by shots, wavelength uniformity, spatial distribution features and reconstruction improvement is established using the proposed approach to calculate the coded aperture distribution. In addition, a remarkable difference between the actual designs and the one proposed is that the proposed design can be implemented as a moving colored lithographic mask using a micro-piezo electric device, achieving a low space-time multishot compressive measurement acquisition. The proposed coded aperture design allows to recover spatio-spectral scenes with up to 3 dB of PSNR in comparison with random CA, and achieves similar results to low-high colored coded apertures designed in [68]. The problem lets to set up as input parameters in the design process, the transmittance and number of shots, as well as the set of filters to be used in the design.

The remainder of this chapter is organized as follows. Section 4.2 introduces the mathematical model of the CASSI system, which is used to model the acquisition of the compressive projections. Section 4.3 develops the colored coded aperture optimization. The colored coded aperture design as well as the shifting model are also described in Section 4.5. Simulations as well as experimental results are presented in section 4.6, and Section 4.7 summarizes the work.

4.2 CASSI System for Spectral Imaging

The coded aperture snapshot spectral imager (CASSI) captures multiplexed 2D projections of the spatiospectral scene. The optical CASSI architecture consists of a coded aperture, a dispersive element, and an FPA. The input, a spectral datacube $\mathbf{F}_{mnk}$ with m, n spatial coordinates, and k spectral bands determines a data cube resolution of $N \times N \times L$, with $m, n = 0, 1, \ldots, N-1$ and $k = 0, 1, \ldots, L-1$. The spatiospectral images are modulated by a discretized binary coded aperture $\mathbf{T}^{\ell}_{mn}$, where $\ell = 0, 1, \ldots, K-1$ indexes the number of snapshots to be captured. These coded apertures have been to date fabricated in materials such as chrome-on-quarts [19], where each coded element is either opaque or transparent to the whole wavelenghts of interest. Recent advances in micro-lithography and coating technology allows the fabrication of multi-patterned arrays of different optical filters, enabling its use on multispectral sensors, electro-mechanical devices, and gratings. The incorporation of this technology in spectral imaging, and specifically in the CASSI system in the form of colored coded apertures allows not only the spatial but the spectral modulation as well. When the binary coded aperture is replaced by a colored coded aperture, it can be seen as $\mathbf{T}^{\ell}_{mnk}$. Using this notation, the ℓ^{th} FPA measurement, referred to as $\mathbf{G}^{\ell}_{mn}$, can be written as

$$\mathbf{G}^{\ell}_{mn} = \sum_{k=0}^{L-1} \mathbf{T}^{\ell}_{m(n-k)k} \ \mathbf{F}_{m(n-k)k} + \boldsymbol{\omega}_{mn}, \tag{4.1}$$

where $\boldsymbol{\omega}_{mn}$ is the white noise of the sensing system. The dispersion induced by the prism is modeled in the horizontal dimension in both the coded aperture and the source. Alternatively, the spatiospectral data cube can be expressed as $\mathbf{F} \in \mathbb{R}^{N \times N \times L}$, or its vector representation $\mathbf{f} \in \mathbb{R}^{N^2 L}$, such that $\mathbf{f} = \boldsymbol{\Psi}\boldsymbol{\theta}$, where $\boldsymbol{\theta}$ is a S-sparse representation on the basis $\mathbf{\Psi}$, and can be approximated by a linear combination of S basis functions chosen from the basis, with $S \ll (N \cdot N \cdot L)$. Following this matrix notation, the CASSI projections in Eq. 4.1 can be rewritten in the standard form of an under-determined system of linear equations:

$$\mathbf{g}^{\ell} = \mathbf{A}^{\ell}\boldsymbol{\theta} = \mathbf{H}^{\ell}\mathbf{\Psi}\boldsymbol{\theta} + \boldsymbol{\omega}, \tag{4.2}$$

where the matrix $\mathbf{A}^{\ell} = \mathbf{H}^{\ell}\mathbf{\Psi}$ is the CASSI sensing matrix, $\mathbf{H}^{\ell}$ is the system transfer function that represents the effects of the coded aperture and the dispersive element, and $\boldsymbol{\omega}$ represent the noise in the system. The matrix $\mathbf{H}^{\ell}$ is defined as $\mathbf{H}^{\ell} = \mathbf{P}\mathbf{T}^{\ell}$, where $\mathbf{P}$ represents the dispersive function of the prism and remains constant for all the snapshots, and $\mathbf{T}^{\ell}$ is determined by the coded aperture. Hence, the CASSI measurement vector $\mathbf{g} = \left[(\mathbf{g}^{0})^{\intercal}, \ldots, (\mathbf{g}^{K-1})^{\intercal}\right]^{\intercal}$ is the concatenation of the set of K snapshots in Eq. 4.2 such that the vector dimension is given by $KU \times 1$, where $U = N(N+L-1)$ is the number of pixels in the detector. The matrix $\mathbf{H} = \left[(\mathbf{H}^{0})^{\intercal}, \ldots, (\mathbf{H}^{K-1})^{\intercal}\right]^{\intercal}$ is a $U \times Q$ matrix, where $Q = N^2L$ is the total number of data cube voxels. The compression ratio achieved with the projection is then calculated as the size of the vector of measurements $\mathbf{g}$ over the total number of data cube voxels KU/N^2L, where K matrices are stacked, one per each shot. Figure 4.1 depicts the physical sensing phenomenon in the colored CASSI. The data cube is modulated by a colored coded aperture, then dispersed, and integrated in the FPA. Each coded aperture pixel has a color, representing the cut-off wavelength, and is marked with a low or high pass filter. A low pass filter element permits the wavelengths under the cut-off to pass through, and a high pass filter element permits the wavelengths over the cut-off to be transmitted.

An estimate of the spatiospectral data cube from the KU measurement pixels can be attained by solving the regularization problem,

$$\hat{\mathbf{f}} = \mathbf{\Psi}\left\{\arg\min_{\boldsymbol{\theta}} \|\mathbf{g} - \mathbf{H}\mathbf{\Psi}\boldsymbol{\theta}\|_2 + \tau\|\boldsymbol{\theta}\|_1\right\}, \tag{4.3}$$

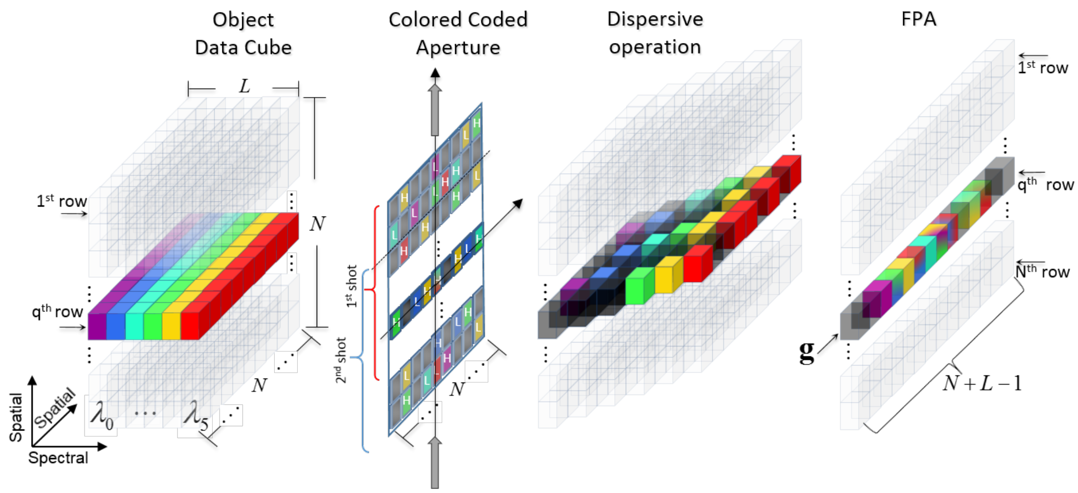

Figure 4.1: Physical sensing phenomena in colored CASSI; L spectral bands of the data cube $\mathbf{F}$ are coded spatially and spectrally by a colored coded aperture, and dispersed by the prism. The detector captures the intensity $\mathbf{g}$ by integrating the coded and dispersed light.

where τ is a regularization constant. The basis representation $\mathbf{\Psi}$ is formulated as the Kronecker product of two bases $\mathbf{\Psi} = \mathbf{\Psi}_1 \bigotimes \mathbf{\Psi}_2$, where $\mathbf{\Psi}_1$ is a 2D wavelet Symmlet 8 basis, and $\mathbf{\Psi}_2$, playing the role of spectral sparsifier, is the one-dimensional discrete cosine transform. Different algorithms have been proposed to solve the optimization problem in Eq. 4.3, including the two-step iterative shrinkage/thresholding (TwIST) [21], the gradient projection for sparse reconstruction (GPSR) [22], Gaussian mixture models (GMM) [23], and the compressive imaging reconstruction algorithm based on the AMP framework [24]. In this work, the GPSR algorithm was used, although any of the other algorithms could be used as well.

4.3 Colored Coded Aperture Optimization

A single shot may not be enough to reach reconstructed scenes with certain quality. In a CASSI multi-shot system, several captures are allowed for a given scene, changing the coded aperture used in each snapshot. A convenient matrix arrangement of the colored coded apertures in binary representation is proposed with the aim of reduce the complexity of the design. Let us define $\mathbf{X}^i \in \mathbb{R}^{N \times N \cdot L}$ as a matrix that

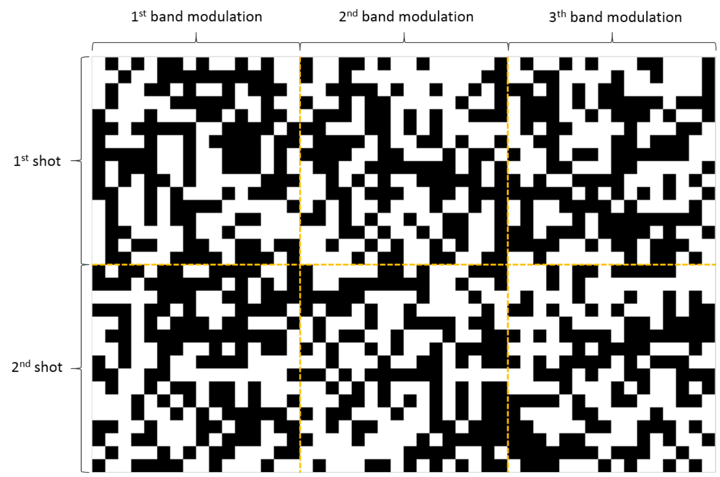

Figure 4.2: Proposed $\mathbf{X}$ matrix arrangement of a colored coded aperture in binary representation with a dimension of $16 \times 16 \times 3$, and for 2 snapshots. A random pattern is used for the sketch.

contains the colored CA pattern for the i^{th} snapshot. The multi-shot CASSI CCA is represented by simply concatenating the corresponding CCA binary matrix of the K shots as $\mathbf{X} = [(\mathbf{X}^1)^\intercal, \ldots, (\mathbf{X}^i)^\intercal, \ldots, (\mathbf{X}^K)^\intercal]^\intercal$ such that $\mathbf{X} \in \mathbb{R}^{KN \times NL}$. Figure 4.2 shows a sketch of the $\mathbf{X}$ matrix arrangement for a modulation coded aperture with 16×16 spatial pixels, 3 spectral bands, and $K = 2$ snapshots.

The main intuition behind the optimization of the colored coded aperture proposed in this work can be summarized as a variability and uniformity promotion. The variability is referred as the low correlation between the rows and columns of $\mathbf{X}$. On the other hand, the uniformity is referred as the even sensing process through the spatial dimensions and spectral bands, as well as through the number of snapshots to be acquired. Since the sampling process is directly affected by the CA, therefore by $\mathbf{X}$, then the matrix $\mathbf{X}$ allows us to define the design of the blockages by finding the solution to the following minimization problem:

$$\mathbf{X}^* = \arg\min_{\mathbf{X}} \left(J(\mathbf{X}) + Q(\mathbf{X}) \right), \tag{4.4}$$

where $\mathbf{X}^*$ is the optimized coded aperture matrix arrangement, and the terms

$J(\cdot)$ and $Q(\cdot)$ account for the *variability* and *uniformity* constraints over $\mathbf{X}$, respectively.

The variability term $J(\mathbf{X})$ and the uniformity term $Q(\mathbf{X})$ in (4.4) are presented in the following subsections. An iterative solution using a gradient descent algorithm to solve Eq. (4.4) is presented in section 4.4.

4.3.1 Variability constraint in Colored Coded Aperture Optimization

The variability constraint begin with the generation of patterns having orthonormal rows and columns. The Gram matrix of the $\mathbf{X}$ matrix is used in the design optimization problem as the constraint inducing the low correlation between the rows and columns of $\mathbf{X}$. The row-wise correlation is formulated in the problem as,

$$\arg\min_{\mathbf{X}} \|\mathbf{I}_1 - \mathbf{X}\mathbf{X}^{\intercal}\|_F^2, \tag{4.5}$$

where $\mathbf{I}_1$ is an identity matrix of size $KN \times KN$, and $\mathbf{X}$ is the optimization variable matrix. The solution of (4.5) yields to a coded aperture ensemble with improved row-wise coherence by maximizing the linear independence of its rows. However, this can result in a high number of column repetitions, so we turn to reduce also the column correlation of $\mathbf{X}$. Therefore, the column-wise correlation is minimized by solving the problem,

$$\arg\min_{\mathbf{X}} \|\mathbf{I}_2 - \mathbf{X}^{\intercal}\mathbf{X}\|_F^2, \tag{4.6}$$

where $\mathbf{I}_2$ is an identity matrix of size $LN \times LN$. Considering both, the row-wise coherence in (4.5) and column-wise coherence in (4.6), the variability cost function of (4.4) is defined as,

$$J(\mathbf{X}) = \phi_1\|\mathbf{I}_1 - \mathbf{X}\mathbf{X}^{\intercal}\|_F^2 + \phi_2\|\mathbf{I}_2 - \mathbf{X}^{\intercal}\mathbf{X}\|_F^2, \tag{4.7}$$

Where the step control variables are ϕ_1 and ϕ_2.

4.3.2 Uniformity constraint in Colored Coded Aperture Optimization

The uniformity constraint is aimed at reducing the spatial, spectral and shot correlation of the samples in the acquisition process. In particular, when multiple shots are acquired, the coded aperture elements, should allow to transmit ideally uniform and non-redundant information of the scene, meaning that the repetition of sensed voxels across shots should be avoided. The number of times a voxel is sensed across shots given a coded aperture arrangement $\mathbf{X}$, can be calculated as the product $\mathbf{RX}$, where $\mathbf{R} = [\mathbf{I}_1, \ldots, \mathbf{I}_k]^\intercal$, and $\mathbf{I}_i$ is an identity matrix of size $N \times N$. The number of repeated sensed voxels in the measurements when multiple shots are acquired can be minimized by solving

$$\arg\min_{\mathbf{X}} \|\mathbf{U} - \mathbf{RX}\|_F^2, \tag{4.8}$$

where $\mathbf{U}$ is a selectable matrix with constant values, which define the number of sensed voxels by each pixel at the FPA detector. Figure 4.3 shows the constraint in Eq. 4.8. Hence, the coded apertures are designed such that the number of times each spectral voxel is sensed remain constant. In the figure, the times each pixel is sensed for each of the bands is calculated. Red and blue squares show voxels of second and third bands, sensed twice in the 2 shots. Notice, that blue pixels are voxels not sensed at all.

Regarding the spectral uniformity constraint, the desired number of times a voxel is sensed should be also constant. As the dispersion affects the spatial position of the integrated voxels in the detector, this dispersion should be considered. Therefore, to guarantee the spectral uniformity, the number of times a voxel is sensed is calculated as $\mathbf{XD}$, where $\mathbf{D}$ is a matrix defined as $\mathbf{D} = [\mathbf{I}_N^\intercal \, \mathbf{0}_{N\times(L-1)}^\intercal, \ldots, \mathbf{0}_{N\times(L-i)}^\intercal \, \mathbf{I}_N^\intercal \, \mathbf{0}_{N\times(L-i)}^\intercal, \ldots,$ $\mathbf{0}_{N\times(L-1)}^\intercal \, \mathbf{I}_N^\intercal]^\intercal$, where $\mathbf{0}_{N\times L-1}$ is a 0−valued $N \times (L-1)$ matrix, and $\mathbf{I}_N$ is an identity $N \times N$ matrix. Then, the number of times a voxel is measured can be minimized by

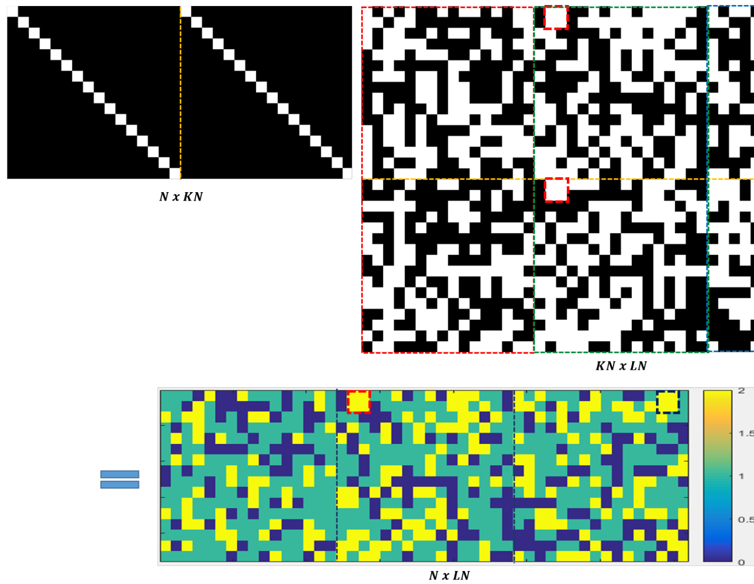

Figure 4.3: Illustration of the uniformity constraint aimed to reduce the total number of times a voxel is sensed through the shots. Red and blue squares in figure show voxels sensed twice for the 2 shots.

adding the constraint,

$$\underset{\mathbf{X}}{\arg\min} \|\mathbf{V} - \mathbf{XD}\|_F^2, \tag{4.9}$$

where $\mathbf{V}$ is a matrix with expected constant values, defining the utilization of the detector pixels. Figure 4.4 presents visually this constraint. Observe the red areas in $\mathbf{X}$, although these three pixel areas are in different spatial positions (shifted one pixel to the right), after the horizontal dispersion and integration of the second shot, they reach the same spatial pixels in the detector. The measurements at the detector, are represented as the resulting matrix $\mathbf{XD}$, where the two measurements shots are stacked one over the other. The yellow pixels in the detector, represent then, detector pixels integrating information of all the three bands, while blue pixels are under-utilized detector pixels. Notice that $\mathbf{XD}$ can be multiplied by $\mathbf{R}$, to calculate how many voxels are integrated in a detector pixel through all the shots. This is presented in Figure 4.5, and it is basically the union of the constraints in Eqs. 4.8 and 4.9. The red and

Figure 4.4: Sketch of the spectral uniformity constraint. Red areas show pixels reaching the same spatial pixels in the detector.Yellow pixels represent detector pixels integrating information of all the bands. Blue pixels are under-utilized detector pixels.

blue squares in the resulting matrix in figure 4.5, show two detector pixels sensing six voxels through 2 shots, or the sum of three spectral voxels per shot. That is a clear example of redundant sensing. These two constraints are considered separately as Eqs. 4.8 and 4.9, such that a different weight can be assigned to each of the constraints.

In order to guarantee the spatial uniformity, two additional constraints are included. The main idea of these constraints is to avoid the clusters of one-valued entries both in the columns and the rows of the coded aperture pattern. To constraint the spatial uniformity two Toeplitz matrices are defined such that they find the columns and row clusters to be reduced through an iterative algorithm. Let $\mathbf{W}$ and $\mathbf{Z}$ be positive definite Toeplitz matrices of size $LN \times LN$ and $KN \times KN$. The spatial column and row uniformity constraints are defined as,

$$\arg\min_{\mathbf{X}} \|\mathbf{B} - \mathbf{X}\mathbf{W}\|_F^2, \tag{4.10}$$

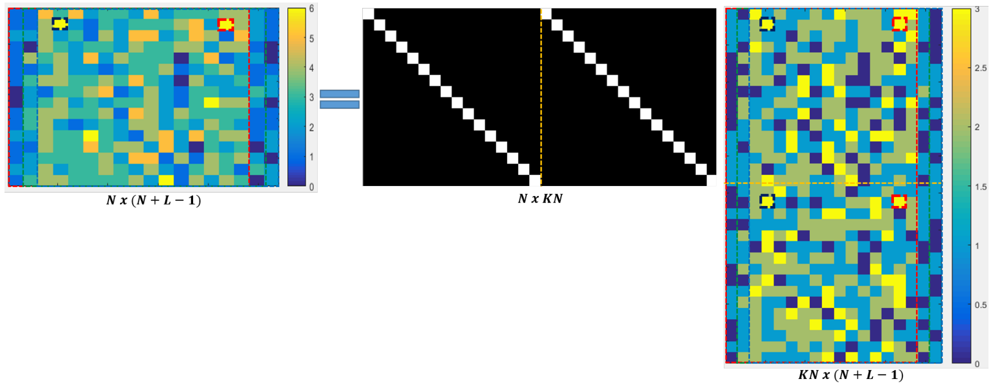

Figure 4.5: Sketch of the spectral and shot uniformity constraint. Red and blue squares show pixels sensed through all the bands and through all the shots.

$$\arg\min_{\mathbf{X}} \|\mathbf{C} - \mathbf{Z}\mathbf{X}\|_F^2, \tag{4.11}$$

where $\mathbf{B}$ and $\mathbf{C}$ are matrices defining the number of adjacent pixels or sensed neighbors of each pixel, $\mathbf{B}$ for vertical adjacency, and $\mathbf{C}$ for horizontal adjacency. This matrices are intended to have constant values, such that no clusters of sensed voxels are allowed. Figures 4.6 and 4.7 illustrate the common columns/rows clusters that can be found using two different Toeplitz matrices, the first matrix having d constant diagonals each one using a different weight, and the second having d constant 1-valued diagonals. The selection of the d number of diagonals and its respective values determine the neighbor ratio to analyze and the weight assigned to each of the surrounded pixel positions, this respectively for each column or row. The expected behavior of the matrix multiplication $\mathbf{XW}$ and $\mathbf{ZX}$ as in the previous constraints is to have a resultant matrix with constant values and therefore a more uniform sensing.

Considering the four uniformity constraints presented before, the uniformity cost function in Eq. 4.4 is expressed as,

$$\begin{aligned} Q(\mathbf{X}) = {} & \phi_3\|\mathbf{U}-\mathbf{R}\mathbf{X}\|_F^2 + \phi_4\|\mathbf{V}-\mathbf{X}\mathbf{D}\|_F^2 \\ & + \phi_5\|\mathbf{B}-\mathbf{X}\mathbf{W}\|_F^2 + \phi_6\|\mathbf{C}-\mathbf{Z}\mathbf{X}\|_F^2. \end{aligned} \tag{4.12}$$

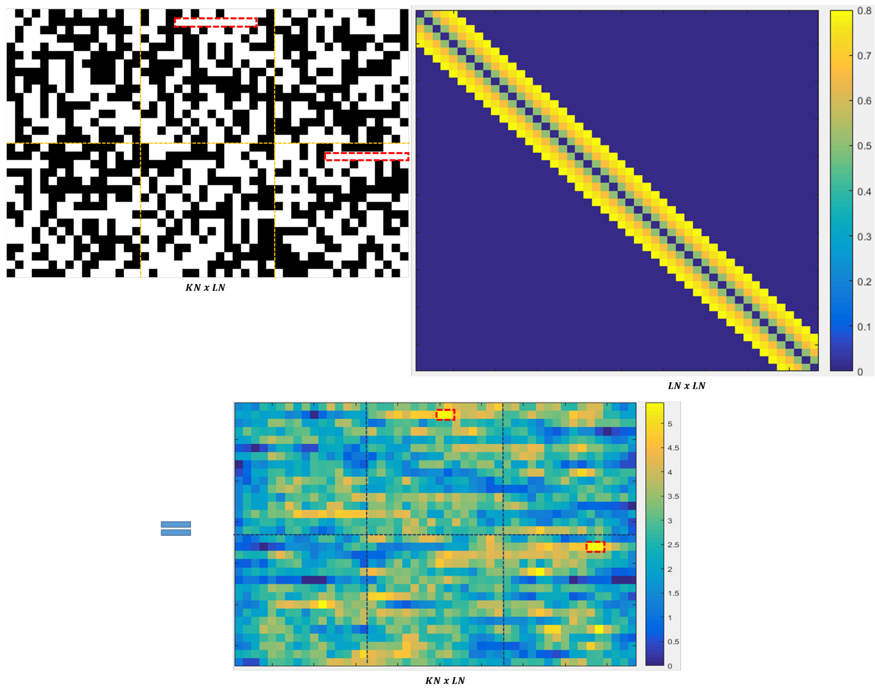

Figure 4.6: Column uniformity constraint illustration: **XW**. Several clusters as the two presented in the figure within red squares should be avoided.

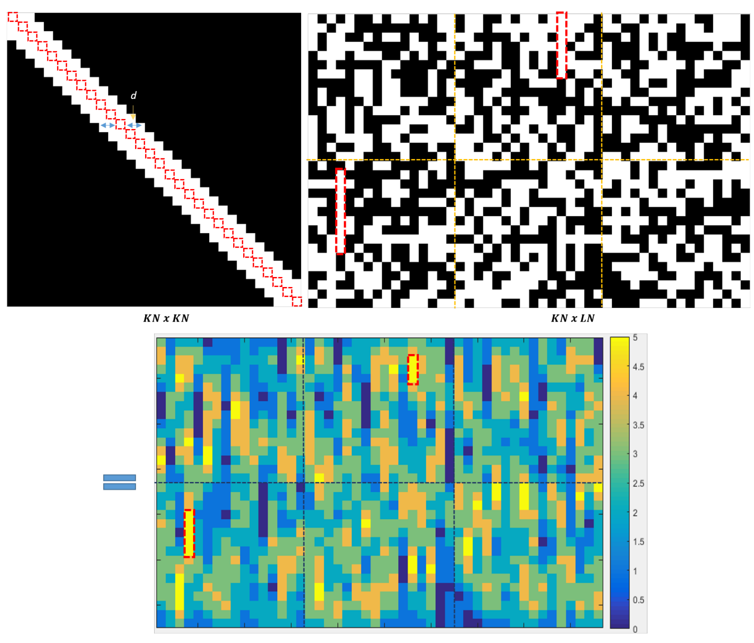

Figure 4.7: Row uniformity constraint illustration: **ZX**. Clusters as the two presented in the figure within red areas should be avoided.

In the following section, we propose an alternating minimization algorithm, which iteratively minimizes 4.4 with the variability promoter $J(\mathbf{X})$ as in Eq. 4.7 and the uniformity promoter $Q(\mathbf{X})$ as in Eq. 4.12 to find an optimized coded aperture arrangement $\mathbf{X}^*$.

4.4 Gradient Descent Approach to find Optimized Colored Coded Aperture

A gradient descent method is applied to minimize Eq. 4.4, starting with a realization of a random coded aperture arrangement $\mathbf{X}$. The minimization method can be described as an iterative process where the coded aperture ensemble at the i^th iteration is given by,

$$\mathbf{X}_i = \mathbf{X}_{i-1} + \eta \left(\nabla_{\mathbf{X}} J(\mathbf{X}) + \nabla_{\mathbf{X}} Q(\mathbf{X}) \right), \tag{4.13}$$

where ∇ is the gradient operator, and $\eta > 0$ is the iteration step size. In order to apply the proposed method, we need to compute the gradient of J with respect to $\mathbf{X}$,

$$\begin{aligned} \nabla J = \frac{\partial J}{\partial \mathbf{X}} &= \frac{\partial}{\partial \mathbf{X}} \left(\|\mathbf{I}_1 - \mathbf{X}\mathbf{X}^\intercal\|_F^2 + \|\mathbf{I}_2 - \mathbf{X}^\intercal\mathbf{X}\|_F^2 \right) \\ &= \frac{\partial}{\partial \mathbf{X}} \mathrm{Tr}\{(\mathbf{I}_1 – \mathbf{X}\mathbf{X}^\intercal)^\intercal(\mathbf{I}_1 – \mathbf{X}\mathbf{X}^\intercal) + (\mathbf{I}_2 – \mathbf{X}^\intercal\mathbf{X})^\intercal(\mathbf{I}_2 – \mathbf{X}^\intercal\mathbf{X})\} \\ &= 4(\mathbf{X}\mathbf{X}^\intercal - \mathbf{I}_1)\mathbf{X} + 4\mathbf{X}(\mathbf{X}^\intercal\mathbf{X} - \mathbf{I}_2), \end{aligned} \tag{4.14}$$

where the derivative is expanded using the $\mathrm{Tr}\{\cdot\}$ operator, which denotes the matrix trace operation. On the other hand, the gradient of Q with respect to $\mathbf{X}$,

$$\begin{aligned} \nabla Q = \frac{\partial Q}{\partial \mathbf{X}} = \frac{\partial}{\partial \mathbf{X}} (&\|\mathbf{U} - \mathbf{R}\mathbf{X}\|_F^2 + \|\mathbf{V} - \mathbf{X}\mathbf{D}\|_F^2 \\ &+ \|\mathbf{B} - \mathbf{X}\mathbf{W}\|_F^2 + \|\mathbf{C} - \mathbf{Z}\mathbf{X}\|_F^2), \end{aligned} \tag{4.15}$$

can be calculated also using the trace operator as,

$$
\begin{aligned}
\frac{\partial Q}{\partial \mathbf{X}} = \frac{\partial}{\partial \mathbf{X}} \mathrm{Tr}\,\{&(\mathbf{U}–\mathbf{RX})^\intercal(\mathbf{U}–\mathbf{RX})+(\mathbf{V}–\mathbf{XD})^\intercal(\mathbf{V}–\mathbf{XD}) \\
&+ (\mathbf{B}–\mathbf{XW})^\intercal(\mathbf{B}–\mathbf{XW})+(\mathbf{C}–\mathbf{ZX})^\intercal(\mathbf{C}–\mathbf{ZX})\} \\
&= 2\mathbf{R}^\intercal(\mathbf{RX} - \mathbf{U}) + 2(\mathbf{XD} - \mathbf{V})\mathbf{D}^\intercal \\
&+ 2(\mathbf{XW} - \mathbf{B})\mathbf{W} + 2\mathbf{Z}(\mathbf{ZX} - \mathbf{C}),
\end{aligned}
\tag{4.16}
$$

where $\mathbf{W}^\intercal = \mathbf{W}$, and $\mathbf{Z}^\intercal = \mathbf{Z}$.

4.5 Shifting Colored Coded Aperture

In practice, the spectral response of the colored coded apertures can be constrained by cost and fabrication limitations. These limitations are given by the type of filters used in the fabrication. Additionally, the cost of the coded aperture increases when a multi-shot system is required, as the number of colored coded apertures also increases. And besides, experimentally, one of the main challenges is the design of compact and portable systems. Following these requirements, two additional specifications design are included in this work. Firstly, since the cost limitation is given by the type of colored filters used in the fabrication of the coded apertures, the spectral response of the filters in the coded aperture is limited to be either low or high pass filters. Secondly, the CCA patterns optimized in the previous section are organized in such a way that only one mask is required for the implementation. This is called ”shifting color coded aperture”, since the mask should be shifted between shots and several pixels of the coded aperture are shared between them.

4.5.1 *LH*-Colored Coded Aperture Design

The spectral response of the colored coded apertures is constrained to low/high (L/H) pass colored coded filters. The cut-off wavelengths of the filters are assumed to be selected from the subset $\lambda_0, \ldots, \lambda_{L-1}$. Thus, there are $2\lambda_L$ colored filters to be selected for each coded aperture pixel. More specifically, the spectral response of a λ_j^{Low} low pass colored coded aperture pixel is given by

$$\left(x_K^{\ell}\right) = \begin{cases} 1 & \text{if } k < \lambda_i^{Low} \\ 0 & \text{otherwhise,} \end{cases} \tag{4.17}$$

for $K = 0, \ldots, L-1$, $i \in 0, \ldots, N^2-1$, and $\ell \in 0, \ldots, K-1$. Similarly, the spectral response of a λ_j^{High} high pass colored coded aperture pixel is given by

$$\left(x_K^{\ell}\right) = \begin{cases} 1 & \text{if } k \geq \lambda_i^{High} \\ 0 & \text{otherwhise.} \end{cases} \tag{4.18}$$

Let the available set of low pass filters be $\Lambda^{Low} = \left\{\lambda_0^{Low}, \ldots, \lambda_L^{Low}\right\}$, and the set of high pass filters $\Lambda^{High} = \left\{\lambda_0^{High}, \ldots, \lambda_L^{High}\right\}$. A thresholding operator is applied with each iteration of the gradient descent algorithm, to reduce the resulting filters in the entries of the coded aperture, to those belonging to the set $\Lambda \in \left\{\Lambda^{Low} \cup \Lambda^{High}\right\}$.

Figure 4.8 shows an example of the set of filters Λ for a specific case of $L = 3$ spectral bands $\lambda_1, \lambda_2, \lambda_3$. In the left the set of filters is presented, in the right four of the six filters spectral responses are shown. The remaining two filters are an all-pass and block filters. A small black lower left or upper right triangle in the middle of a pixel represents a low or a high pass filter respectively.

The equivalent representation of a colored coded aperture and its binary arrangement matrix $\mathbf{X}$ is presented in figure 4.9 for a coded aperture of 4×4 spatial pixels, $L = 3$ spectral bands, and $K = 2$ shots. The respective equivalence of two color coded aperture pixels is shown for high pass filter in the upper side of the figure and a low pass filter in the bottom side of the figure.

4.5.2 Shifting Color Coded Aperture Design

Multiple colored coded apertures can be implemented by coating a DMD or by moving a colored lithographic mask using a micro-piezo electric device, a shifting colored coded aperture design is proposed in order to reduce the cost of its implementation

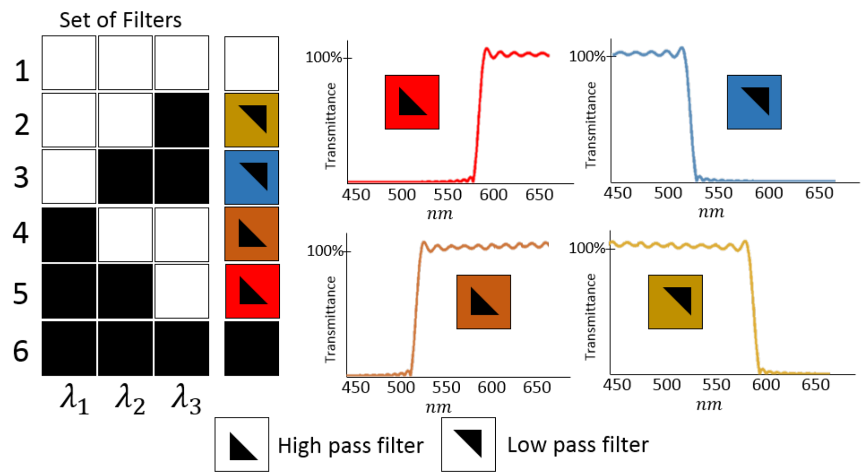

Figure 4.8: Set of filters for $L = 3$ spectral bands $\lambda_1, \lambda_2, \lambda_3$. In the left the set of filters is presented with its respective color pixel representation. In the right the spectral response of four of the six filters is shown.

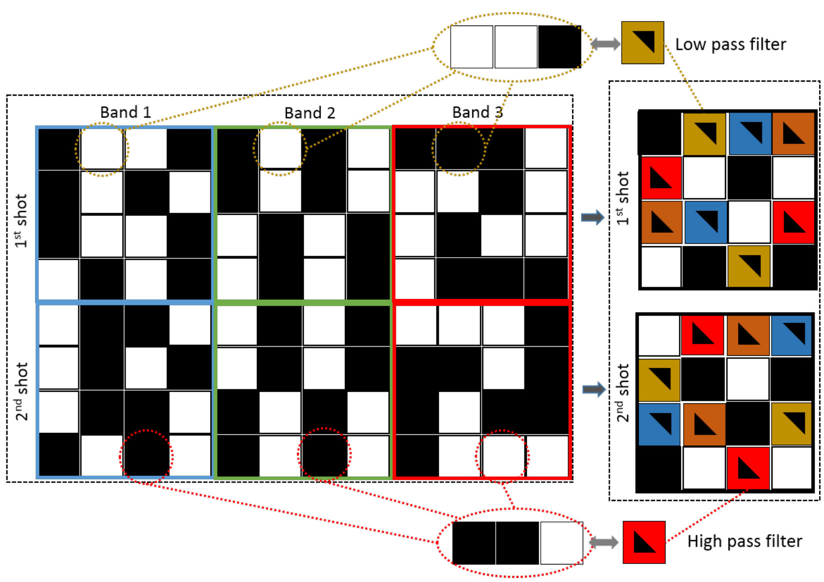

Figure 4.9: Equivalent representation of a colored coded aperture and its binary arrangement matrix $\mathbf{X}$. The colored coded aperture dimensions are 4×4 spatial pixels, $L = 3$ spectral bands, and $K = 2$ shots. A high pass and a low pass filters representations are specified.

as well as to improve the compactness of the compressive system. Figure 4.1 shows how the colored coded aperture can be moved or shifted upwards in order to capture a second shot.

Three shifting strategies can be considered for the coded aperture design, vertical, horizontal, and diagonal. However, given that the dispersion induced by the prism occurs in the horizontal dimension, and then the information from the different spectral bands is multiplexed, the horizontal and diagonal (involving vertical and horizontal shifting) strategies are discarded.

One of the main constraints fulfilled by the optimized colored coded aperture is that the filters have to be as complementary as possible among the shots such that the sum of the filters contains all the spectral components. With the aim to preserve the shots uniformity constraint in the design of the vertical shifting codes, a strategy based on patch concatenation is proposed in this work. The strategy consists in the concatenation of vertical complementary colored coded aperture patches of size $S \times N$, where S is the shifting parameter, corresponding to the number of pixels the mask should be moved between shots, and N is the number of spatial columns of the colored coded aperture. This strategy only requires K complementary colored coded aperture patches, which will be interleaved one after the other, such that all the shots maintain the uniformity. Figure 4.10 illustrates the concatenation shifting strategy used to reduce a color coded aperture for $K = 2$ shots. The parameter $S = 2$, and the final spatial dimension of the shifting colored coded aperture is $N + (S * (K - 1))$.

4.6 Simulations and Experimental Results

4.6.1 Simulations

The proposed model is verified using the forward model in Eq. 4.2. Three sets of compressive measurements are simulated. The only difference between sets is the modulation pattern. The first set is modulated by a random LH-colored coded aperture, which entries are realizations of a Bernoulli random variable and restricted to the corresponding set of LH filters defined in 4.5.1, the second set is modulated

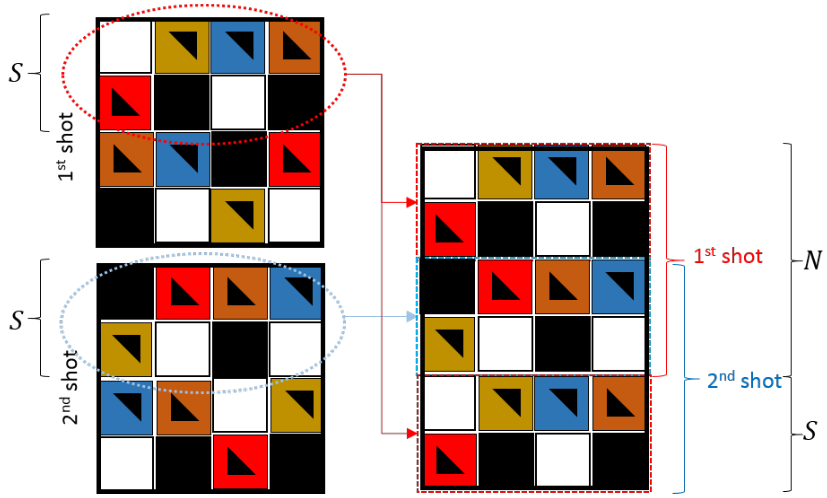

Figure 4.10: The colored coded aperture resulting from binary arrangement **X** in Fig. 4.9 is used to show the concatenation shifting strategy used to design the shifting color coded apertures.

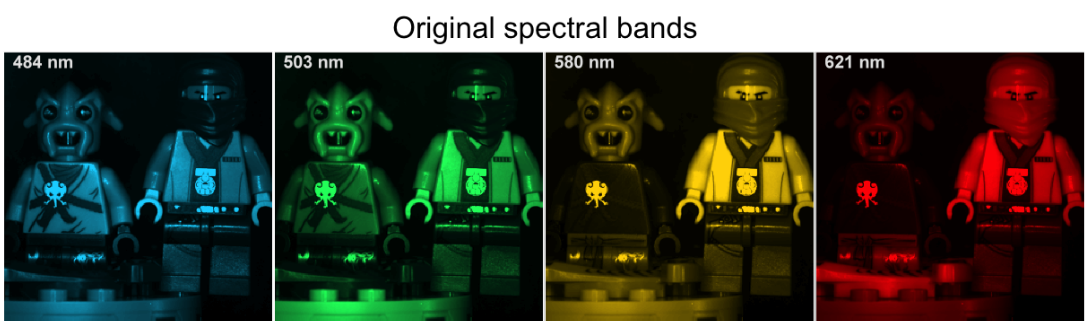

Figure 4.11: Four of the eight original spectral bands of the data cube used in simulations.

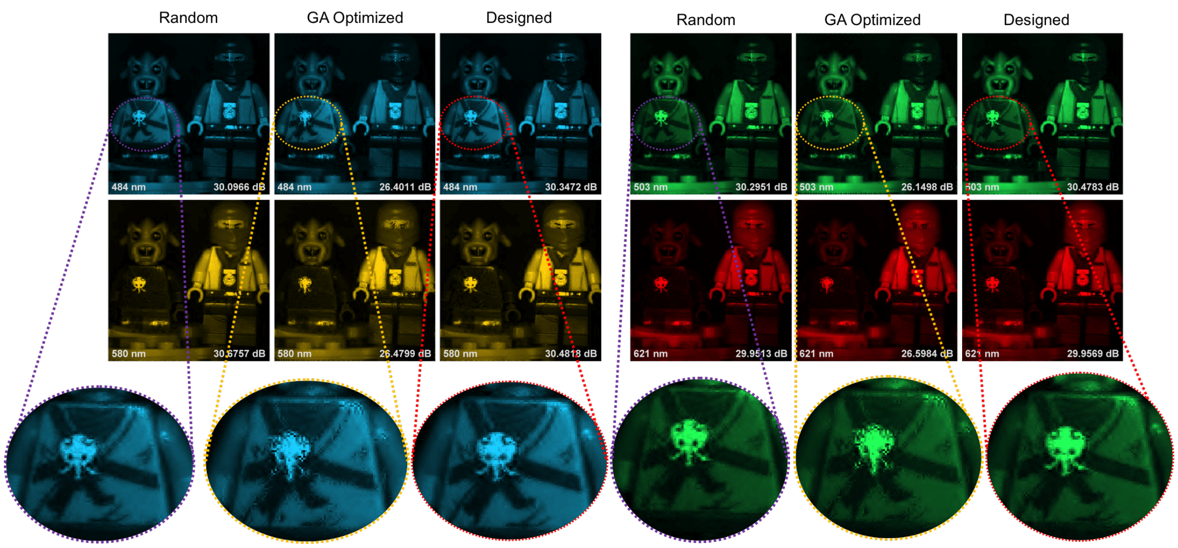

Figure 4.12: Reconstruction of four spectral bands using the CASSI with color coded apertures and 2 measurements shots. For each spectral band, three reconstructions from measurements modulated by LH-colored coded apertures, with a random pattern (Random), an optimized coded aperture in literature, designed by a genetic algorithm (GA optimized), and the designed coded apertures (Designed) are shown.

by an optimized LH-colored coded aperture in literature, designed by a genetic algorithm (GA)[68], and the third set is modulated by the proposed shifting colored coded aperture pattern. All the three coded apertures are designed to be shifted patterns in order to make a fair comparison. A test spatio spectral data cube $\mathbf{F}$ is acquired using a monochromator in the spectral range between 450 and 650nm with a spatial resolution of 256×256 pixels, and $L = 8$ spectral bands. The camera used to capture the data cube is a CCD camera AVT Marlin F0033B, with 656×492 pixels and a pixel pitch size of $9.9\mu m$. The resolution of the colored coded apertures of the three sets is 256×256 pixels, and they were acquired using the same 16 low-high color filter set, as defined in section 4.5.1. The transmittance of all the coded apertures depends directly on the number of shots, using the relation $T = 1/K$. The simulations were performed for $K = 2, 4$ shots.

The sensing reconstruction (GPSR) algorithm is applied to reconstruct the data cube [22], solving the inverse problem in Eq. 4.3. Figure 4.11 shows four of the eight spectral bands of the original data cube used for the simulations. Figures 4.12 and 4.13 present the respective reconstructions for two and four measurements shots respectively, and for a shifting value of $S = 8$ pixels. For each spectral band, the reconstructions from the measurements acquired using the random, the GA optimized, and the designed color coded aperture are presented. The spatial quality is improved when the designed coded aperture is used, and it can be easily noticed in the PSNR values.

An analysis of the shifting parameter S is performed for $K = 2$ and $K = 4$ measurements shots, and for the three set of measurements. The performance achieved by the designed coded apertures is for both number of shots, superior than the random and the GA optimized coded apertures. The performance can be seen in Fig. 4.14 for $K = 2$ shots, and in Fig. 4.15 for $K = 4$ shots. The results corresponds with results in literature [68], where random colored coded apertures are shown to behave closely as the optimized designs for $K = 2$. For greater number of shots $K = 4$, the designed coded apertures beat random codes for all the shifting values.

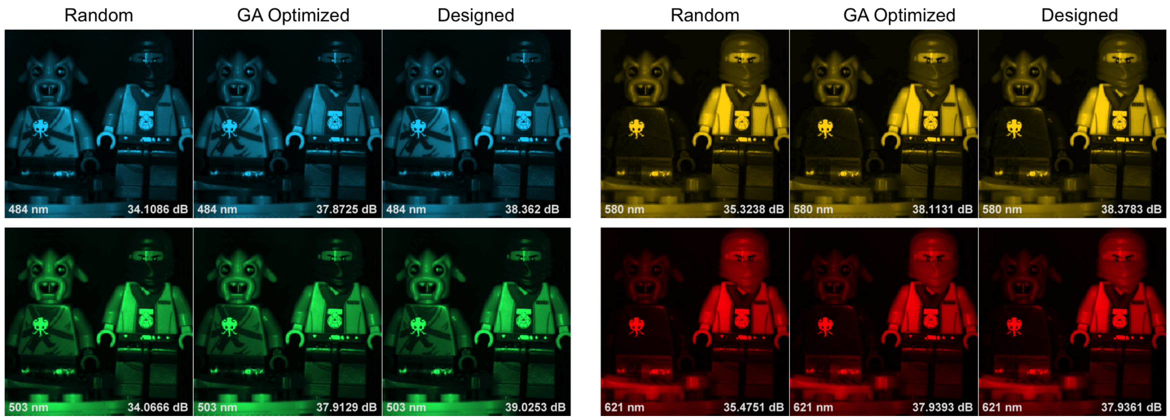

Figure 4.13: Reconstruction of four spectral bands using the CASSI with color coded apertures and 4 measurements shots. For each spectral band, three reconstructions from measurements modulated by LH-colored coded apertures, with a random pattern (Random), an optimized coded aperture in literature, designed by a genetic algorithm (GA optimized), and the designed coded apertures (Designed) are shown.

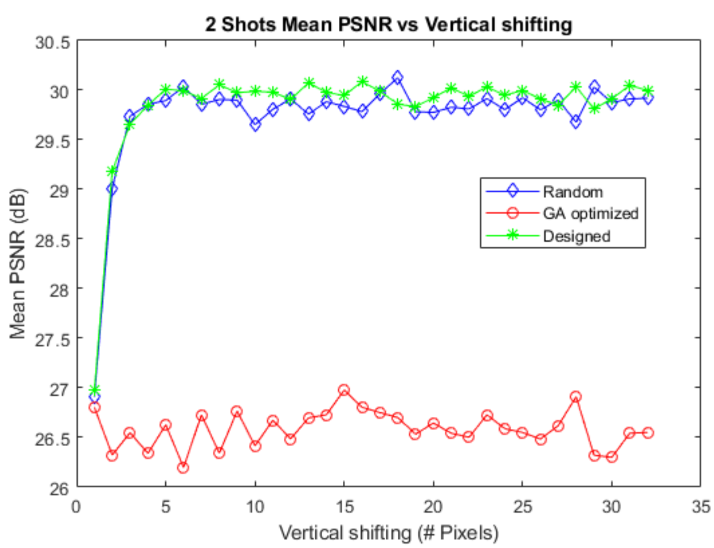

Figure 4.14: Mean PSNR achieved with $K = 2$ measurements shots for different vertical shifting value S from 1 to 32 pixels.

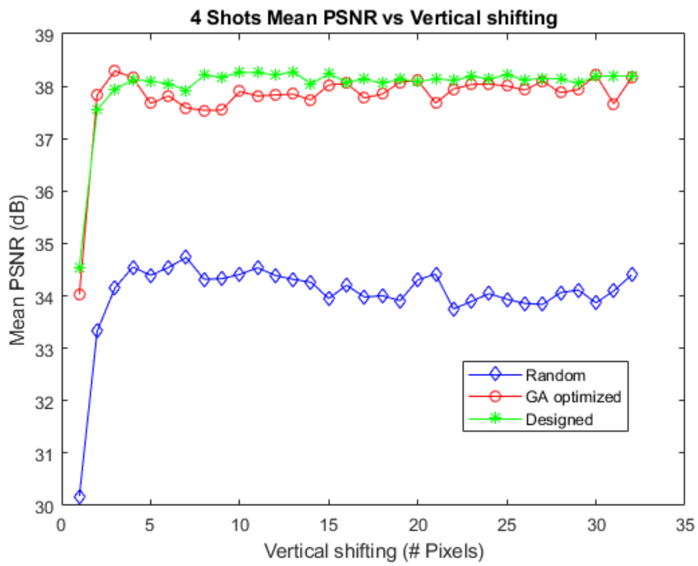

Figure 4.15: Mean PSNR achieved with $K = 4$ measurements shots for different vertical shifting value S from 1 to 32 pixels.

4.6.2 Experimental Results

The CASSI system was experimentally realized to demonstrate the proposed design method of the shifting colored coded apertures. To emulate the colored coded apertures, the equivalent binary codes were implemented in a Texas Instruments D1100 DMD (DLP), a custom double Amici prism (Shangai Optics) was used as a dispersive element, and an FPA detector (Stingray F-033B) captured the measurements. The nonlinear dispersion curve of the prism was determined experimentally by using a monochromator. The DMD used to implement the coded apertures has a resolution of 1024×768 and a mirror pitch the size of $13.68\mu m$. The FPA detector used in this experimental setup has a resolution of 1280×960 pixels and a pitch size of $6.45\mu m$.

Three sets of compressive measurements were acquired by using the CASSI optical setup for two different targets. Figure 4.16 shows the real scenes used in the experiments. The first set of compressive measurements was modulated by a LH random color coded aperture, the second was modulated by an optimized LH-colored coded

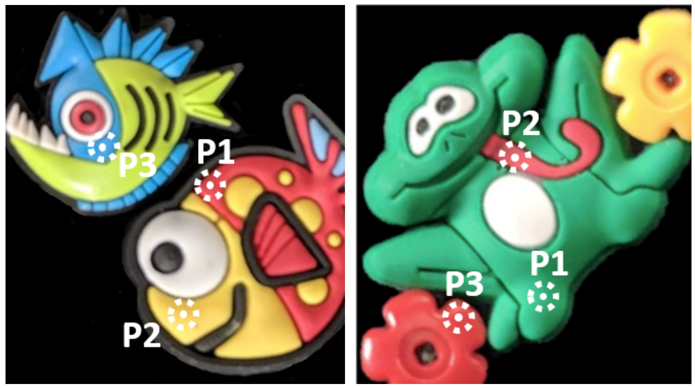

Figure 4.16: Two real scenes used to show the performance of designed shifting color coded apertures.

aperture in literature, designed by a genetic algorithm (GA), and the third was modulated by the the proposed LH shifting color coded aperture. The spatial resolution of the scenes, coded apertures, and respective reconstructions is limited to 256×256 pixels. The number of resolvable bands was $L = 8$. The GPSR algorithm was used to recover the spatio-spectral data cube using the model as formulated in Eq. 4.3. $K = 2, 4$ shots where acquired and reconstructed. The spatial reconstructions for the scenes are shown in Figs. 4.17,- 4.20. Figures 4.17 and 4.18 illustrate four reconstructed spectral bands of target 1 using $K = 2$ and $K = 2$ shots respectively, and for the three colored coded apertures.

The quality on the reconstructed bands using the designed coded apertures outperforms the results attained with the random coded apertures. Figure 4.18 shows the same four reconstructed bands of the target 1 but using $K = 4$ shots. Notice the quality of improvement achieved at the objects in the scene.

Figures 4.19 and 4.20 present the same spatial bands for target 2, using $K = 2$ and $K = 4$ shots respectively. The quality of the reconstructions using the proposed shifting color coded apertures is better in the borders details.

The RGB profiles of target 1 are show in figures 4.21 and 4.22, for $K = 2$ and $K = 4$ measurements shots respectively. The visual improvement is noticeable, the RGB obtained when using the optimized color coded apertures are high-fidelity with

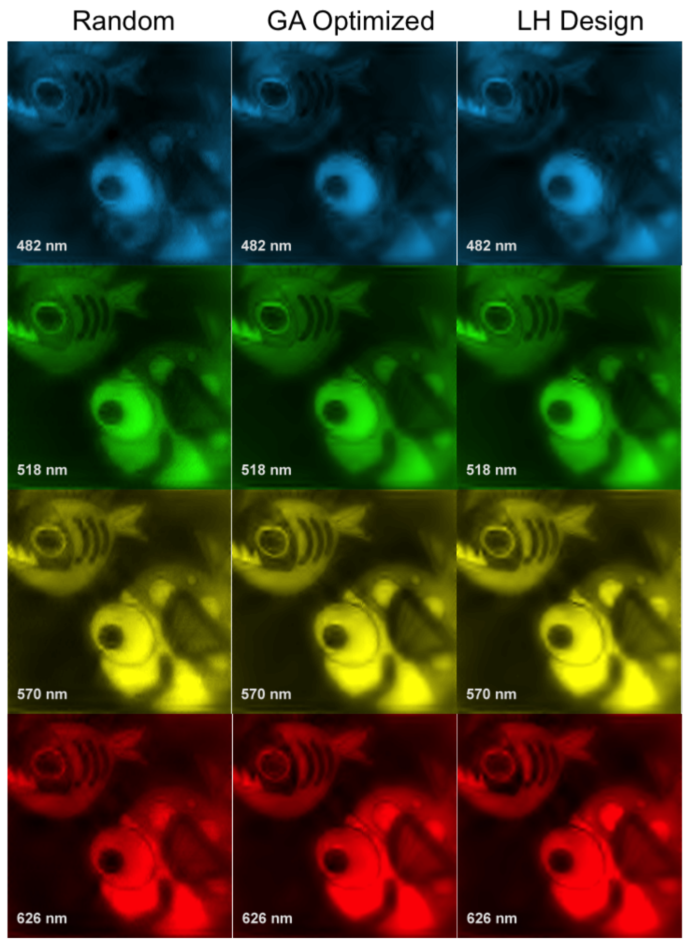

Figure 4.17: Reconstruction of four bands for Target 1 using LH random, genetic algorithm optimized and designed shifting colored coded apertures, for 2 shots.

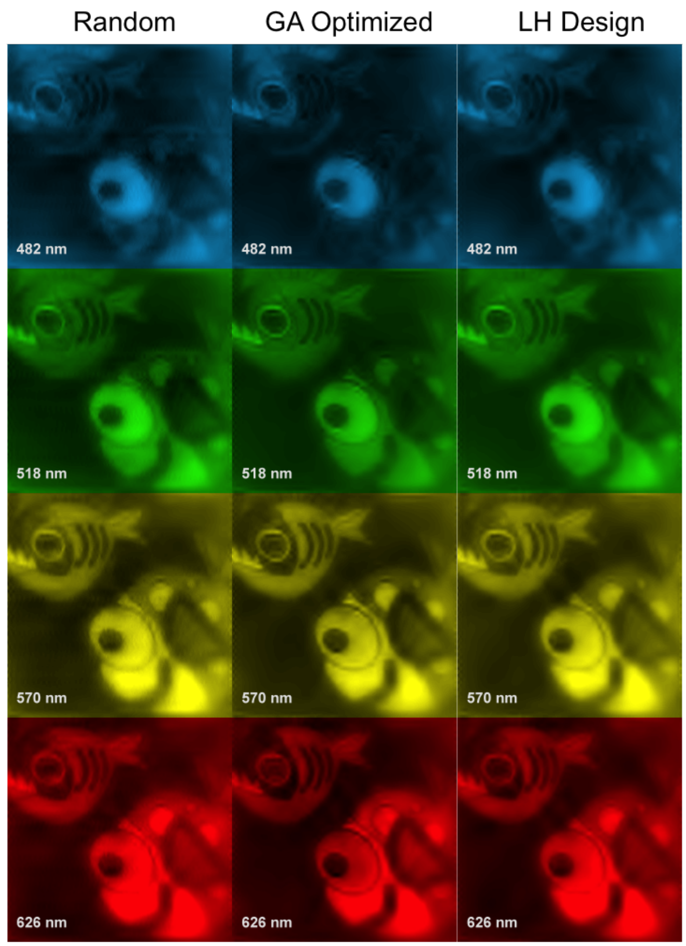

Figure 4.18: Reconstruction of four bands for Target 1 using LH random, genetic algorithm optimized and designed shifting colored coded apertures, for 4 shots.

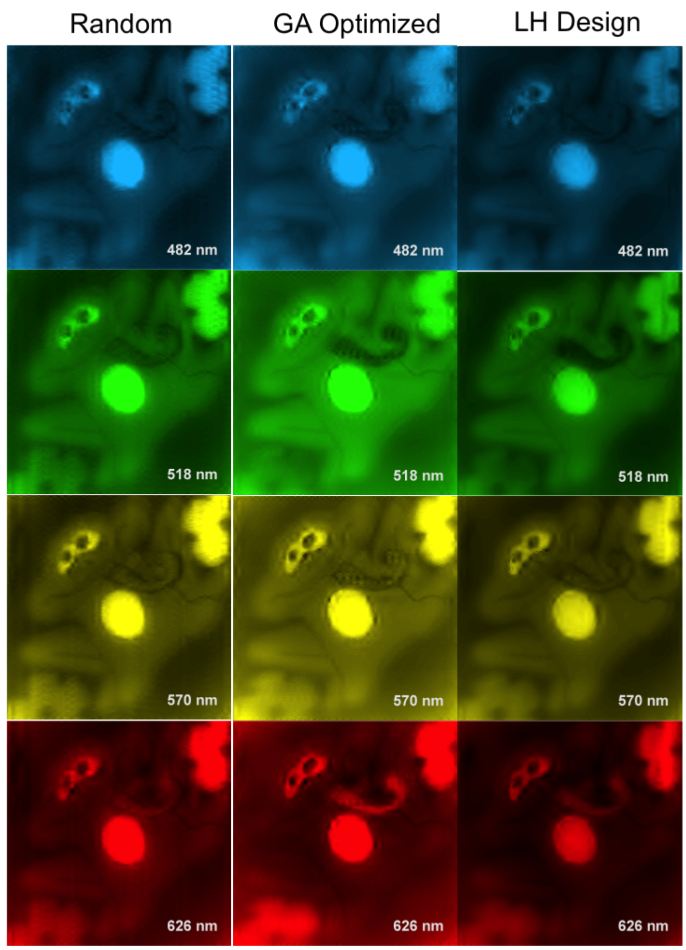

Figure 4.19: Reconstruction of four bands for Target 2 using LH random, genetic algorithm optimized and designed shifting colored coded apertures, for 2 shots.

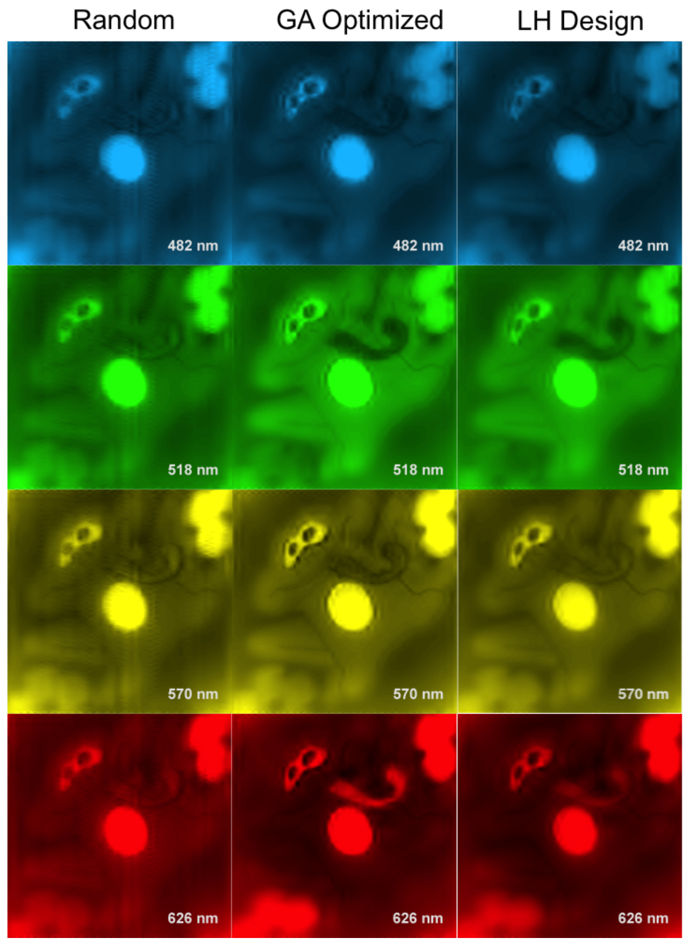

Figure 4.20: Reconstruction of four bands for Target 2 using LH random, genetic algorithm optimized and designed shifting colored coded apertures, for 4 shots.

Figure 4.21: RGB profiles of reconstructed target 1 using $K = 2$ measurements shots. (Left) Random. (Center) GA Optimized. (Right) Designed.

Figure 4.22: RGB profiles of reconstructed target 1 using $K = 4$ measurements shots. (Left) Random. (Center) GA Optimized. (Right) Designed color coded apertures.

the real targets. The same results are shown in figures 4.23 and 4.24, for $K = 2$ and $K = 4$ measurements shots, for target 2.

Figures 4.25-4.30 show the spectral signatures for three points randomly chosen from the reconstructions of the two targets, and for two and four shots. The points are indicated as P1, P2, and P3 in fig 4.16. The original signature, obtained using a commercially available spectrometer (Ocean Optics USB2000+), is compared with the spectral reconstruction using the LH random, genetic algorithm optimized and the designed shifting color coded apertures. The curves obtained by using the CASSI and the designed shifting color coded aperture are closer to the original signatures. It is noticeable the improvement in the reconstructed spectral profile going from $K = 2$ to $K = 4$ measurements shots when using the shifting color coded apertures.

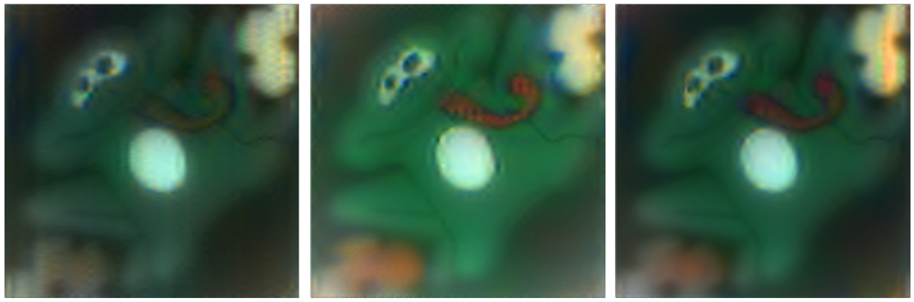

Figure 4.23: RGB profiles of reconstructed target 2 using $K = 2$ measurements shots. (Left) Random. (Center) GA Optimized. (Right) Designed color coded apertures.

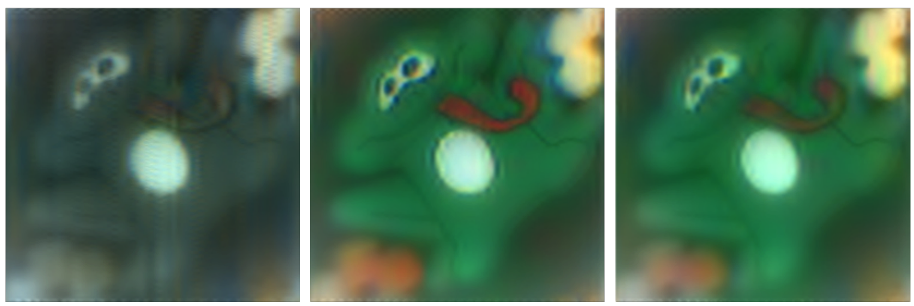

Figure 4.24: RGB profiles of reconstructed target 2 using $K = 4$ measurements shots. (Left) Random. (Center) GA Optimized. (Right) Designed color coded apertures.

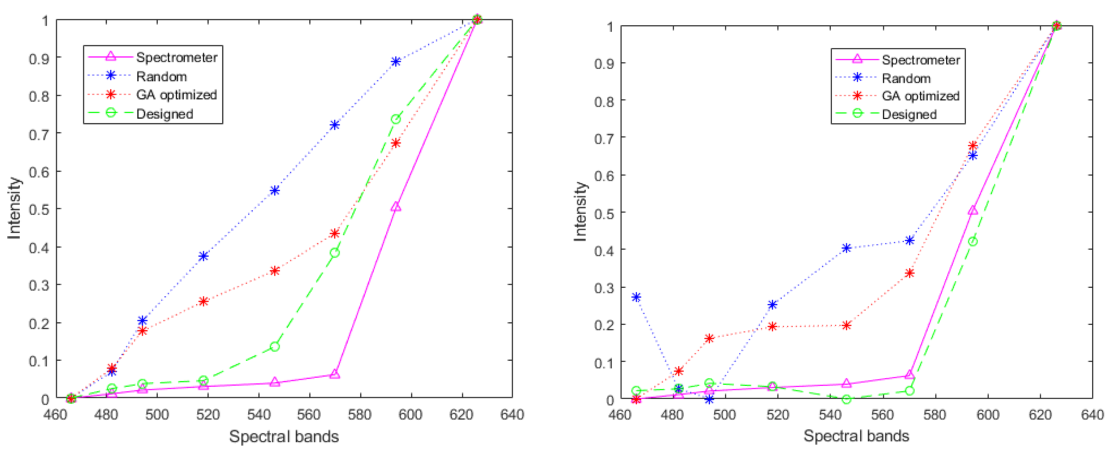

Figure 4.25: Spectral signatures for P1 (red) in target 1 when (Left) $K = 2$, and (Right) $K = 4$ shots are used.

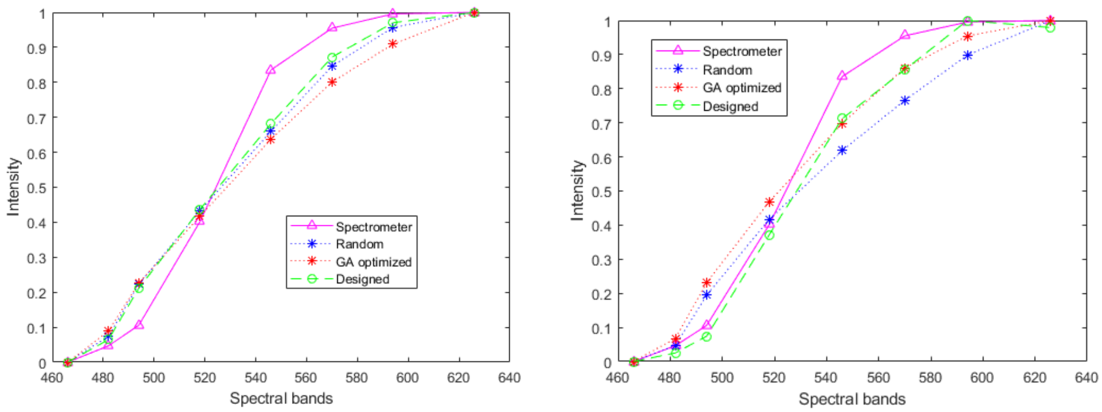

Figure 4.26: Spectral signatures for P2 (yellow) in target 1 when (Left) $K = 2$, and (Right) $K = 4$ shots are used.

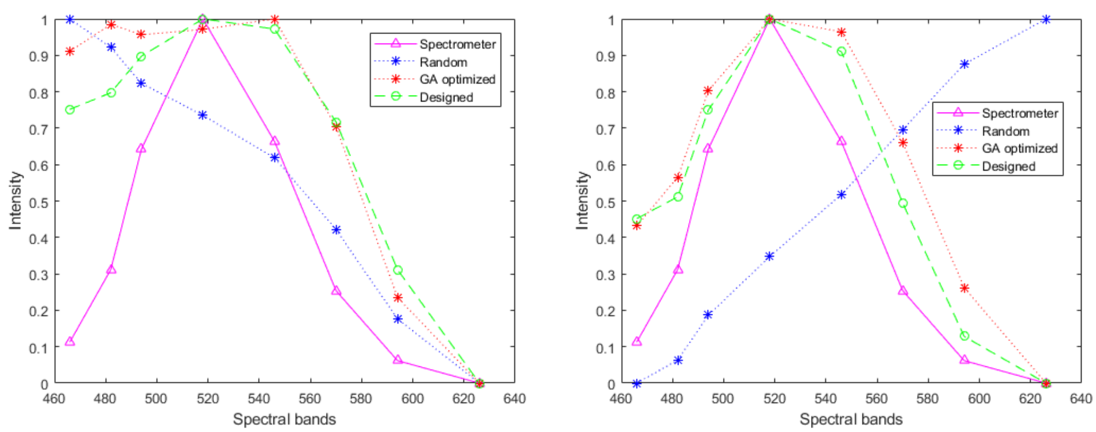

Figure 4.27: Spectral signatures for P3 (blue) in target 1 when (Left) $K = 2$, and (Right) $K = 4$ shots are used.

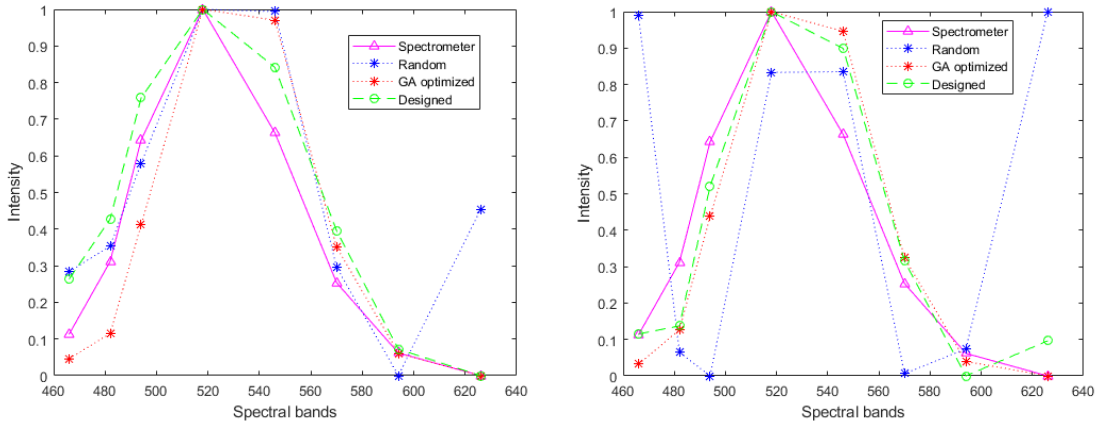

Figure 4.28: Spectral signatures for P1 (green) in target 2 when (Left) $K = 2$, and (Right) $K = 4$ shots are used.

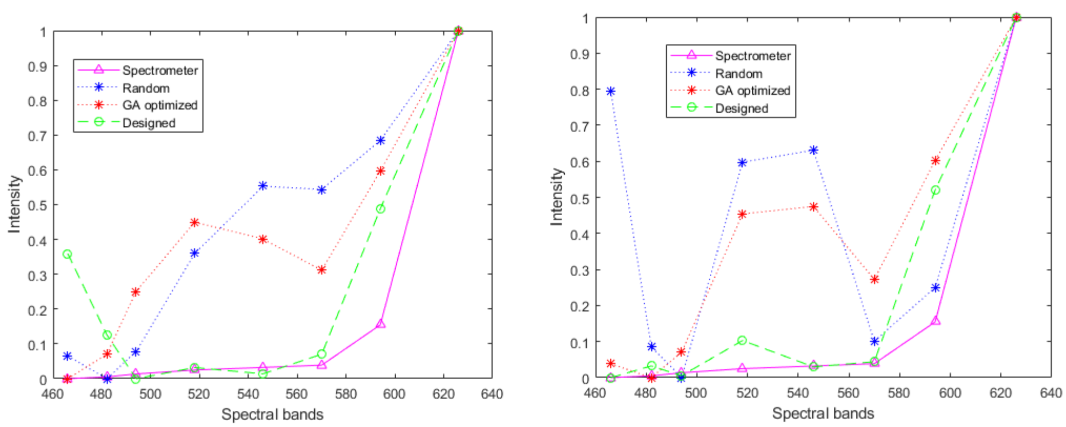

Figure 4.29: Spectral signatures for P2 (red) in target 2 when (Left) $K = 2$, and (Right) $K = 4$ shots are used.

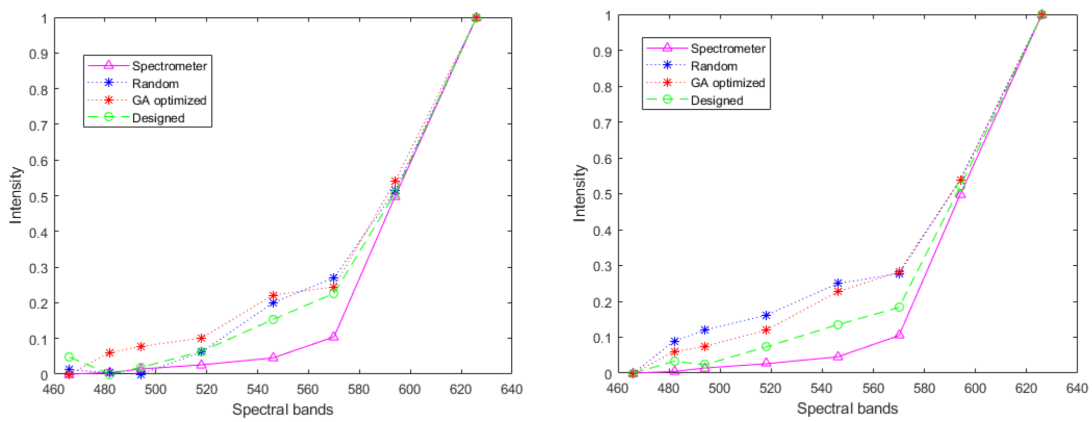

Figure 4.30: Spectral signatures for P3 (red-orange) in target 2 when (Left) $K = 2$, and (Right) $K = 4$ shots are used.

4.7 Conclusions

A shifting color coded aperture optimization is proposed. The optimization promotes the variability in the columns and rows of the coded aperture, and the uniformity constraint aimed at reducing the spatial, spectral and shot correlation of the samples in the acquisition process. In addition, the optimization design includes cost and fabrication constraints, for that reason, the set of filters is limited, and a shifting feature of the mask is proposed, such that only one mask is required for several shots in a real implementation. The shifting color coded apertures were experimentally demonstrated in a compressive spectral imaging architecture. Real reconstructions show the spatial and spectral improvement achieved with the proposed optimization in comparison with random color coded apertures, and a genetic algorithm optimization from the literature.

BIBLIOGRAPHY

[1] Alfredo Thenkabail, Prasad S Lyon, and John G Huete. *Hyperspectral remote sensing of vegetation*. CRC Press, 2011.

[2] Di Wu and Da-Wen Sun. Advanced applications of hyperspectral imaging technology for food quality and safety analysis and assessment: A reviewpart i: Fundamentals. *Innovative Food Science & Emerging Technologies*, 19:1–14, 2013.

[3] Matthew E Martin, Musundi B Wabuyele, Kui Chen, Paul Kasili, Masoud Panjehpour, Mary Phan, Bergein Overholt, Glenn Cunningham, Dale Wilson, Robert C DeNovo, et al. Development of an advanced hyperspectral imaging (hsi) system with applications for cancer detection. *Annals of biomedical engineering*, 34(6):1061–1068, 2006.

[4] Guolan Lu, Luma Halig, Dongsheng Wang, Xulei Qin, Zhuo Georgia Chen, and Baowei Fei. Spectral-spatial classification for noninvasive cancer detection using hyperspectral imaging. *Journal of biomedical optics*, 19(10):106004–106004, 2014.

[5] Qingli Li, Xiaofu He, Yiting Wang, Hongying Liu, Dongrong Xu, and Fangmin Guo. Review of spectral imaging technology in biomedical engineering: achievements and challenges. *Journal of biomedical optics*, 18(10):100901–100901, 2013.

[6] Hamed Akbari, Luma V Halig, David M Schuster, Adeboye Osunkoya, Viraj Master, Peter T Nieh, Georgia Z Chen, and Baowei Fei. Hyperspectral imaging and quantitative analysis for prostate cancer detection. *Journal of biomedical optics*, 17(7):0760051–07600510, 2012.

[7] Michael Theodore Eismann. Hyperspectral remote sensing. SPIE Bellingham, 2012.

[8] M Govender, K Chetty, and H Bulcock. A review of hyperspectral remote sensing and its application in vegetation and water resource studies. *Water Sa*, 33(2):145–151, 2007.

[9] Elhadi Adam, Onisimo Mutanga, and Denis Rugege. Multispectral and hyperspectral remote sensing for identification and mapping of wetland vegetation: a review. *Wetlands Ecology and Management*, 18(3):281–296, 2010.

[10] Haida Liang. Advances in multispectral and hyperspectral imaging for archaeology and art conservation. *Applied Physics A*, 106(2):309–323, 2012.

[11] Guillaume Dupuis, Mady Elias, and Lionel Simonot. Pigment identification by fiber-optics diffuse reflectance spectroscopy. *Applied Spectroscopy*, 56(10):1329–1336, 2002.

[12] Kirk Martinez, John Cupitt, David Saunders, and Ruven Pillay. Ten years of art imaging research. *Proceedings of the IEEE*, 90(1):28–41, 2002.

[13] John K Delaney, Jason G Zeibel, Mathieu Thoury, Roy Littleton, Michael Palmer, Kathryn M Morales, E René de La Rie, and Ann Hoenigswald. Visible and infrared imaging spectroscopy of picasso's harlequin musician: mapping and identification of artist materials in situ. *Applied spectroscopy*, 64(6):584–594, 2010.

[14] Dimitris Manolakis and Gary Shaw. Detection algorithms for hyperspectral imaging applications. *IEEE signal processing magazine*, 19(1):29–43, 2002.

[15] Dimitris Manolakis, David Marden, and Gary A Shaw. Hyperspectral image processing for automatic target detection applications. *Lincoln laboratory journal*, 14(1):79–116, 2003.

[16] Adrian Stern. Optical compressive imaging, 2016.

[17] M. E. Gehm, R. John, D. J. Brady, R. M. Willett, and T. J. Schulz. Single-shot compressive spectral imaging with a dual-disperser architecture. *Opt. Express*, 15(21):14013–14027, Oct 2007.

[18] Y. Wu, I. O. Mirza, G. R. Arce, and D. W. Prather. Development of a digital-micromirror-device-based multishot snapshot spectral imaging system. *Opt. Lett*, 36:2692–2694, 2011.

[19] A. A. Wagadarikar, R. John, R. Willett, and D. Brady. Single disperser design for coded aperture snapshot spectral imaging. *Appl. Opt.*, 47:B44–B51, 2008.

[20] H. Arguello, C. V. Correa, and G. R. Arce. Fast lapped block reconstructions in compressive spectral imaging. *Applied Optics*, 52(10):D32–D45, April 2013.

[21] J. M. Bioucas-Dias and M. A. T. Figueiredo. A new twist: Two-step iterative shrinkage/thresholding algorithms for image restoration. *IEEE Transactions on Image Processing*, 16(12):2992–3004, Dec 2007.

[22] M. Figueiredo, R. D. Nowak, and S. J. Wright. Gradient projection for sparse reconstruction: Application to compressed sensing and other inverse problems. *Selected Topics in Signal Processing, IEEE Journal of*, 1(4):586–597, 2007.

[23] Ajit Rajwade, David Kittle, Tsung-Han Tsai, David Brady, and Lawrence Carin. Coded hyperspectral imaging and blind compressive sensing. *SIAM Journal on Imaging Sciences*, 6(2):782–812, 2013.

[24] J. Tan, Y. Ma, H. Rueda, D. Baron, and G. R. Arce. Compressive hyperspectral imaging via approximate message passing. *IEEE Journal of Selected Topics in Signal Processing*, 10(2):389–401, March 2016.

[25] R. Glenn Sellar and Glenn D. Boreman. Classification of imaging spectrometers for remote sensing applications. *Optical Engineering*, 44(1):013602–013602–3, 2005.

[26] G. R. Arce, D. J. Brady, L. Carin, H. Arguello, and D. S. Kittle. An introduction to compressive coded aperture spectral imaging. *IEEE Signal Processing Magazine*, 2013.

[27] Chengbo Li, Ting Sun, K.F. Kelly, and Yin Zhang. A compressive sensing and unmixing scheme for hyperspectral data processing. *Image Processing, IEEE Transactions on*, 21(3):1200–1210, March 2012.

[28] D. Kittle, K. Choi, A. A. Wagadarikar, and D. J. Brady. Multiframe image estimation for coded aperture snapshot spectral imagers. *Appl. Opt.*, 49(36):6824–6833, Dec 2010.

[29] H. Arguello, H. Rueda, Y. Wu, D. W. Prather, and G. R. Arce. Higher-order computational model for coded aperture spectral imaging. *Applied Optics*, 52(10):D12–D21, April 2013.

[30] H. Arguello and G. R. Arce. Code aperture optimization for spectrally agile compressive imaging. *J. Opt. Soc. Am. A*, 28(11):2400–2413, Nov 2011.

[31] Chris Slinger, Helen Bennett, Gavin Dyer, Neil Gordon, David Huckridge, Mark McNie, Richard Penney, Ian Proudler, Kevin Rice, Kevin Ridley, Lee Russell, Geoffrey de Villiers, and Philip Watson. Adaptive coded-aperture imaging with subpixel superresolution. *Opt. Lett.*, 37(5):854–856, Mar 2012.

[32] Ashwin A. Wagadarikar, Nikos P. Pitsianis, Xiaobai Sun, and David J. Brady. Video rate spectral imaging using a coded aperture snapshot spectral imager. *Opt. Express*, 17(8):6368–6388, Apr 2009.

[33] Y. Wu, C. Chen, Z. Wang, P. Ye, G. R. Arce, D. Prather, and Garrett J. Schneider. Fabrication and characterization of a compressive-sampling multispectral imaging system. *Optical Engineering*, 48(12):123201–123201–12, 2009.

[34] S. K. Nayar, V. Branzoi, and T. E. Boult. Programmable imaging using a digital micromirror array. In *Computer Vision and Pattern Recognition. CVPR 2004. Proceedings of the IEEE Computer Society Conference on*, volume 1, pages I–436–I–443, 2004.

[35] Norbert Schuster and John Franks. Challenges, constraints and results of lens design in 8-12micron waveband for bolometer-fpas having a pixel pitch 12micron. volume 8704, pages 870424–870424–10, 2013.

[36] Florence de la Barrière, Guillaume Druart, Nicolas Guérineau, Jean Taboury, Jérôme Primot, and Joël Deschamps. Modulation transfer function measurement of a multichannel optical system. *Appl. Opt.*, 49(15):2879–2890, May 2010.

[37] R. E. Carrillo, L. F. Polania, and K. E. Barner. Iterative algorithms for compressed sensing with partially known support. In *2010 IEEE International Conference on Acoustics, Speech and Signal Processing*, pages 3654–3657, March 2010.

[38] R. von Borries, C. J. Miosso, and C. Potes. Compressed sensing using prior information. In *Computational Advances in Multi-Sensor Adaptive Processing, 2007. CAMPSAP 2007. 2nd IEEE International Workshop on*, pages 121–124, Dec 2007.

[39] Z. Li, W. Xu, Y. Tian, Y. Wang, and J. Lin. Compressed sensing reconstruction algorithms with prior information: Logit weight simultaneous orthogonal matching pursuit. In *2014 IEEE 79th Vehicular Technology Conference (VTC Spring)*, pages 1–5, May 2014.

[40] J. Scarlett, J. S. Evans, and S. Dey. Compressed sensing with prior information: Information-theoretic limits and practical decoders. *IEEE Transactions on Signal Processing*, 61(2):427–439, Jan 2013.

[41] R. E. Carrillo and K. E. Barner. Lorentzian iterative hard thresholding: Robust compressed sensing with prior information. *IEEE Transactions on Signal Processing*, 61(19):4822–4833, Oct 2013.

[42] N. Vaswani and W. Lu. Modified-cs: Modifying compressive sensing for problems with partially known support. In *2009 IEEE International Symposium on Information Theory*, pages 488–492, June 2009.

[43] X. Wang and J. Liang. Side information-aided compressed sensing reconstruction via approximate message passing. In *2014 IEEE International Conference on Acoustics, Speech and Signal Processing (ICASSP)*, pages 3330–3334, May 2014.

[44] J. F. C. Mota, N. Deligiannis, and M. R. D. Rodrigues. Compressed sensing with side information: Geometrical interpretation and performance bounds. In *Signal and Information Processing (GlobalSIP), 2014 IEEE Global Conference on*, pages 512–516, Dec 2014.

[45] Guang-Hong Chen, Jie Tang, and Shuai Leng. Prior image constrained compressed sensing (piccs): A method to accurately reconstruct dynamic ct images from highly undersampled projection data sets. *Medical Physics*, 35(2):660–663, 2008.

[46] F. Renna, L. Wang, X. Yuan, J. Yang, G. Reeves, R. Calderbank, L. Carin, and M. R. D. Rodrigues. Classification and reconstruction of compressed gmm signals with side information. In *2015 IEEE International Symposium on Information Theory (ISIT)*, pages 994–998, June 2015.

[47] Lior Weizman, Yonina C. Eldar, and Dafna Ben Bashat. Compressed sensing for longitudinal mri: An adaptive-weighted approach. *Medical Physics*, 42(9):5195–5208, 2015.

[48] Xiaojing Fang, Jiao Feng, and Yongjin Wang. Texture-adaptive hyperspectral video acquisition system with a spatial light modulator. In *Proc. SPIE*, volume 9273, pages 92730F–92730F–6, 2014.

[49] Chenguang Ma, Xun Cao, Xin Tong, Qionghai Dai, and Stephen Lin. Acquisition of high spatial and spectral resolution video with a hybrid camera system. *International Journal of Computer Vision*, 110(2):141–155, 2014.

[50] X. Cao, X. Tong, Q. Dai, and S. Lin. High resolution multispectral video capture with a hybrid camera system. In *Computer Vision and Pattern Recognition (CVPR), 2011 IEEE Conference on*, pages 297–304, June 2011.

[51] Chenguang Ma, Xun Cao, Rihui Wu, and Qionghai Dai. Content-adaptive high-resolution hyperspectral video acquisition with a hybrid camera system. *Opt. Lett.*, 39(4):937–940, Feb 2014.

[52] Reza Arablouei, Ethan Goan, Stephen Gensemer, and Kusy Branislav. Fast and robust pushbroom hyperspectral imaging via dmd-based scanning. volume 9948, 2016.

[53] G. Warnell, S. Bhattacharya, R. Chellappa, and T. Baar. Adaptive-rate compressive sensing using side information. *IEEE Transactions on Image Processing*, 24(11):3846–3857, Nov 2015.

[54] Masahiro Yamaguchi. *Optics and Computational Methods for Hybrid Resolution Spectral Imaging*, pages 23–32. Springer International Publishing, Cham, 2015.

[55] D.J. Brady. *Optical Imaging and Spectroscopy*. Wiley, 2009.

[56] J. Canny. A computational approach to edge detection. *IEEE Transactions on Pattern Analysis and Machine Intelligence*, (6):679–698, Nov 1986.

[57] R. K. Sidhu. Improved canny edge detector in various color spaces. In *Proceedings of 3rd International Conference on Reliability, Infocom Technologies and Optimization*, pages 1–6, Oct 2014.

[58] D.L. Lau and G.R. Arce. *Modern Digital Halftoning, Second Edition*. Signal Processing and Communications. Taylor & Francis, 2001.

[59] D. L. Lau, R. Ulichney, and G. R. Arce. Blue and green noise halftoning models. *IEEE Signal Processing Magazine*, 20(4):28–38, July 2003.

[60] D. L. Lau, G. R. Arce, and N. C. Gallagher. Digital color halftoning with generalized error diffusion and multichannel green-noise masks. *Trans. Img. Proc.*, 9(5):923–935, May 2000.

[61] Chen Fu, Henry Arguello, Brian M. Sadler, and Gonzalo R. Arce. Compressive spectral polarization imaging by a pixelized polarizer and colored patterned detector. *J. Opt. Soc. Am. A*, 32(11):2178–2188, Nov 2015.

[62] Claudia V. Correa, Henry Arguello, and Gonzalo R. Arce. Spatiotemporal blue noise coded aperture design for multi-shot compressive spectral imaging. *J. Opt. Soc. Am. A*, 33(12):2312–2322, Dec 2016.

[63] Kaiming He, Jian Sun, and Xiaoou Tang. Guided image filtering. In *Proceedings of the 11th European Conference on Computer Vision: Part I*, ECCV'10, pages 1–14, Berlin, Heidelberg, 2010. Springer-Verlag.

[64] Xun Cao, Tao Yue, Xing Lin, Stephen Lin, Xin Yuan, Qionghai Dai, Lawrence Carin, and David J Brady. Computational snapshot multispectral cameras: toward dynamic capture of the spectral world. *IEEE Signal Processing Magazine*, 33(5):95–108, 2016.

[65] Nathan Hagen and Michael W Kudenov. Review of snapshot spectral imaging technologies. *Optical Engineering*, 52(9):090901–090901, 2013.

[66] Claudia V Correa, Henry Arguello, and Gonzalo R Arce. Spatiotemporal blue noise coded aperture design for multi-shot compressive spectral imaging. *JOSA A*, 33(12):2312–2322, 2016.

[67] RM Willett, Michael E Gehm, and David J Brady. Multiscale reconstruction for computational spectral imaging. In *Electronic Imaging 2007*, pages 64980L–64980L. International Society for Optics and Photonics, 2007.

[68] Henry Arguello and Gonzalo R Arce. Colored coded aperture design by concentration of measure in compressive spectral imaging. *IEEE Transactions on Image Processing*, 23(4):1896–1908, 2014.

[69] M. Elad. Optimized projections for compressed sensing. *IEEE Transactions on Signal Processing*, 55(12):5695–5702, Dec 2007.

[70] Laura Galvis, Henry Arguello, and Gonzalo R. Arce. Coded aperture design in mismatched compressive spectral imaging. *Appl. Opt.*, 54(33):9875–9882, Nov 2015.

[71] Laura Galvis, Daniel Lau, Xu Ma, Henry Arguello, and Gonzalo R. Arce. Coded aperture design in compressive spectral imaging based on side information. *Appl. Opt.*, 56(22):6332–6340, Aug 2017.

[72] Edson Mojica, Said Pertuz, and Henry Arguello. High-resolution coded-aperture design for compressive x-ray tomography using low resolution detectors. *Optics Communications*, 404:103 – 109, 2017. Super-resolution Techniques.

[73] M. Aharon, M. Elad, and A. Bruckstein. *rmk*-svd: An algorithm for designing overcomplete dictionaries for sparse representation. *IEEE Transactions on Signal Processing*, 54(11):4311–4322, Nov 2006.

[74] Z. Wang, G. R. Arce, and J. L. Paredes. Colored random projections for compressed sensing. In *2007 IEEE International Conference on Acoustics, Speech and Signal Processing - ICASSP '07*, volume 3, pages III–873–III–876, April 2007.

[75] A. Parada-Mayorga and G. arce. Colored coded aperture design in compressive spectral imaging via minimum coherence. *IEEE Transactions on Computational Imaging*, PP(99):1–1, 2017.

[76] Michael Lustig, David Donoho, and John M. Pauly. Sparse mri: The application of compressed sensing for rapid mr imaging. *Magnetic Resonance in Medicine*, 58(6):1182–1195, 2007.

[77] Z. Wang and G. R. Arce. Variable density compressed image sampling. *IEEE Transactions on Image Processing*, 19(1):264–270, Jan 2010.

[78] Vahid Abolghasemi, Saideh Ferdowsi, and Saeid Sanei. A gradient-based alternating minimization approach for optimization of the measurement matrix in compressive sensing. *Signal Processing*, 92(4):999–1009, 2012.

[79] Julio Martin Duarte-Carvajalino and Guillermo Sapiro. Learning to sense sparse signals: Simultaneous sensing matrix and sparsifying dictionary optimization. *IEEE Transactions on Image Processing*, 18(7):1395–1408, 2009.

[80] W. Chen, M. R. D. Rodrigues, and I. J. Wassell. Projection design for statistical compressive sensing: A tight frame based approach. *IEEE Transactions on Signal Processing*, 61(8):2016–2029, April 2013.

Appendix A

COPYRIGHT NOTICE

Appendix B

DISCLAIMER

Some target objects used in this dissertation were not endorsed by the trademark owners and they are used here as fair use to illustrate the quality of reconstruction of compressive spectral image measurements. LEGO is a trademark of the LEGO Group, which does not sponsor, authorize or endorse the images in this dissertation. The LEGO Group. All Rights Reserved. http://aboutus.lego.com/en-us/legal-notice/fair-play/.